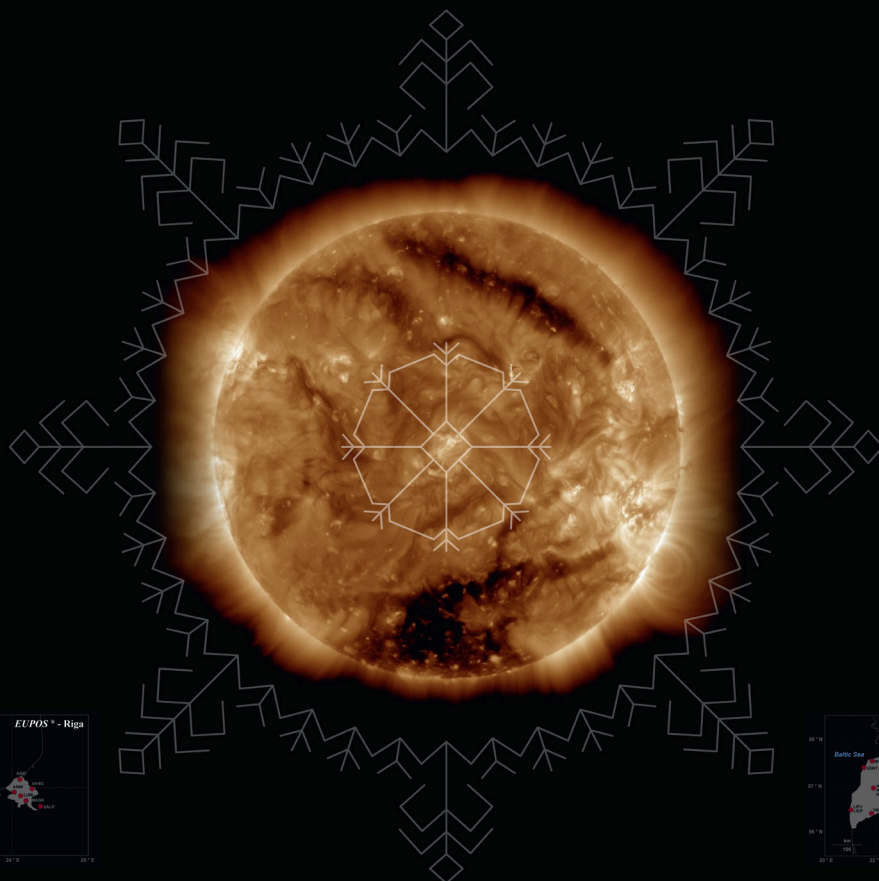


**Madara Normanda**

# SPACE WEATHER IMPACT ON GPS POSITIONING RESULTS IN LATVIA

Doctoral Thesis



**RIGA TECHNICAL UNIVERSITY**

Faculty of Civil and Mechanical Engineering  
Institute of Transport Infrastructure Engineering

**Madara Normanda**

Doctoral Student of the Doctoral Study Programme “Construction”

**SPACE WEATHER IMPACT ON GPS  
POSITIONING RESULTS IN LATVIA**

**Doctoral Thesis**

Scientific supervisors

Prof. *Dr. phys.*

J. BALODIS

*Dr. sc. ing.*

I. VĀRNA

Riga 2024

## ANNOTATION

The term “space weather” generally refers to conditions on the Sun, in the solar wind, and within the Earth's magnetosphere, ionosphere and thermosphere that can influence the performance and reliability of space-borne and ground-based technological systems and can endanger human life or health (definition used by the U.S. National Space Weather Plan).

The peak of the 25th solar activity cycle is approaching and with the expansion of Global Navigation Satellite Systems’ (GNSS) Continuously Operating Reference Station (CORS) networks for high precision positioning and automated device guiding, the space weather impact on the GNSS positioning precision has nowadays become an important topic of discussion in various branches of GNSS applications in national economies.

Here, in the frame of this Doctoral Thesis, the NAVigation System Timing And Ranging (NAVSTAR) Global Positioning System (GPS, the U.S. positioning system) observation data out of all the existing GNSS systems, has been considered. As of today, GPS is used in most of the navigation and device guidance applications. The use of this data particularly contributes to the European Commissions’ defined roadmap for the evolution of the GNSS Mission beyond Europe’s Global Navigation Satellite System (GALILEO) Full Operational Capability (FOC) and the European Geostationary Navigation Overlay Service (EGNOS) Version 3 (V3). One of the three mission evolution objectives states: “In order to remain competitive, services offered by GALILEO should offer a level of performance at least comparable to the best-in-class GNSS. Therefore, in the current context, modernized-GPS level of performance should be taken as the benchmark. In order to be used independently in critical infrastructure, the European satellite navigation infrastructure should guarantee the best level of availability possible. Therefore, robustness and reliability of services should be considered as primary objectives in all technical trade-offs” (written in the Statement of Work of the “Evil waveform and ionospheric characterization monitoring network” (Reference: H2020-SOW-ESA-037-00001, date of issue 10/10/2018) invitation to tender).

The objective of this Doctoral Thesis is to verify the stability of the Latvian GNSS CORS networks (further on referred to as the Latvian CORS networks), used for Real Time Kinematics (RTK) and static measurements. To achieve the objective, this study assesses the impact of space weather on positioning accuracy and coordinate stability over an 11-year timeframe covering the whole 24th cycle of solar activity, by means of the statistical analysis of kinematic coordinate discrepancies in relation to the publicly available ionospheric Total

Electron Content (TEC) and Rate Of change of TEC Index (ROTI) levels, in the midlatitude, in the region – Latvia.

For this purpose, a new methodology was developed, using the GPS observation data of the Latvian CORS networks': LatPos and *EUPOS*<sup>®</sup>-Riga, which have been operating since 2007 (some stations since 2006), as well as the International GPS/GNSS Service (IGS)/European Reference Frame Permanent GNSS Network (EPN) station RIGA, providing a remarkable GNSS observation data base, for the years 2007–2017. The time of the installation of Latvian GNSS CORS stations almost coincides with the beginning of the 24th solar cycle, therefore for the data post-processing and the research in general, one full solar cycle which is 11 years long, has been considered.

Data sets of 4 to 5 months of each year of high Sun activity, geomagnetic storms, solar flares and extreme TEC and ROTI levels were selected and post-processed using *Bernese GNSS Software v5.2*. 90-second kinematic time series of all the Latvian CORS stations for a period from 2007 to 2017 were obtained as well as the flowchart for the data analysis and statistics. At the Institute of Geodesy and Geoinformatics, University of Latvia (LU GGI) new software scripts were developed in Fortran g95 and Python programming languages. The obtained results were analysed and confirmed by this newly developed and applied methodology.

A correlation between time series outliers (hereinafter referred to as faulty solutions or disturbances) and significant space weather events was sought. Over 36 million position determination solutions were examined, 0.6 % of the solutions appear to be faulty, 0.01 % of all solutions show positioning discrepancies greater than 50 meters, 0.05 % have discrepancies greater than 10 m, 0.13 % of the solutions have discrepancies greater than 1 m. The correlation between faulty solutions, TEC and ROTI levels and *Bernese GNSS Software v5.2* detected cycle slips was computed. This also includes an analysis of faulty solutions' distribution simultaneously occurring in several stations.

The geomagnetic storm on March 17, 2015 was the most remarkable solar activity event that created significant (~500 m) positioning discrepancies in the Latvian CORS stations and correlated with high TEC level. The monthly positioning discrepancy diagrams revealed simultaneous faulty solutions at numerous individual stations. The output was analysed, and it was identified that for several stations the faulty solutions sometimes appear more than 150–200 times. This was assumed to be the Loss-of-Lock (LoL) of GNSS receivers. In years 2007–2017 there was only one solar activity event that correlated with high TEC level, the performed Pearsons' correlation analysis revealed that the global TEC and ROTI approximation models do not describe the details of ionosphere anomaly irregularities.

Taking into account that midlatitude regions have been rarely investigated, the research conducted in the frame of this Doctoral Thesis is filling the gap in the research related to space weather phenomena in these areas. The analysis is performed over the entire solar cycle. This historical analysis is giving information on the similar situations that will arise in the next solar cycle.

The research conducted in the frame of this Doctoral Thesis is the first step to raise the awareness of space weather impact on GNSS positioning results in Latvia at a national level.

The Doctoral Thesis includes 33 figures, 21 formulas, 25 tables, and 2 appendices. The total volume of the Doctoral Thesis is 93 pages.

## ANOTĀCIJA

Kosmisko laikapstākļu jēdzienu parasti attiecina uz situāciju, kas novērojama uz Saules, Saules vējā, Zemes magnetosfērā, jonosfērā un termosfērā. Kosmiskie laikapstākļi var ietekmēt kosmosā bāzēto un uz Zemes esošo tehnoloģisko sistēmu veiktspēju un uzticamību, un apdraudēt cilvēka dzīvību un veselību (definīcija, kas tiek lietota ASV Nacionālajā kosmisko laikapstākļu plānā).

Tuvojas 25. Saules aktivitātes cikla maksimums. Līdz ar globālo navigācijas satelītu sistēmu (angļu val. – *Global Navigation Satellite Systems; GNSS*) nepārtraukti darbojošos atbalsta staciju (angļu val. – *Continuously Operating Reference Stations; CORS*) tīklu paplašināšanos un to pielietošanu augstas precizitātes pozicionēšanā un automatizētu ierīču vadīšanā par nozīmīgu diskusiju tēmu valstu tautsaimniecībās un dažādās *GNSS* pielietošanas nozarēs ir kļuvis jautājums par kosmisko laikapstākļu ietekmi uz *GNSS* pozicionēšanas precizitāti.

Šī promocijas darba ietvaros no visu esošo *GNSS* sistēmu datiem, ir apskatīti globālās pozicionēšanas sistēmas (*GPS* – ASV navigācijas sistēma laika un attāluma noteikšanai (angļu val. – *NAVigation System Timing And Ranging; NAVSTAR*)) novērojumu dati. Šobrīd *GPS* tiek izmantota lielākajā daļā navigācijas un ierīču vadības lietojumprogrammu. Šo datu izmantošana atbilst Eiropas Komisijas izstrādātajā ceļvedī noteiktajam par *GNSS* misiju un tās attīstību, Eiropas globālās navigācijas satelītu sistēmas (*GALILEO*) pilnīgas darbības (angļu val. – *Full Operational Capability; FOC*) uzsākšanu un Eiropas ģeostacionārās navigācijas pārklājuma pakalpojuma (angļu val. – *European Geostationary Navigation Overlay Service; EGNOS*) 3. versijas (*V3*) īstenošanu. Viens no 3 (trim) attīstības mērķiem nosaka: “Lai saglabātu konkurētspēju, *GALILEO* piedāvātajiem pakalpojumiem ir jānodrošina tāds veiktspējas līmenis, kas ir salīdzināms ar labāko *GNSS* kategorijā. Pašreizējā kontekstā par etalonu būtu jāņem modernizētās *GPS* veiktspējas līmenis. Lai Eiropas satelīt-navigācijas infrastruktūru varētu izmantot neatkarīgi, kritiskajā infrastruktūrā tai būtu jāgarantē vislabākais iespējamais pieejamības līmenis. Pakalpojumu vienkāršība un uzticamība būtu jāuzskata par galvenajiem mērķiem visos tehniskajos kompromisos” (raksfīts izsludinātā konkursa darba “Traucējumu viļņu forma un jonosfēru raksturojošais uzraudzības tīkls” (angļu val. – “*EVIL WAVEFORM AND IONOSPHERIC CHARACTERIZATION MONITORING NETWORK*” aprakstā (H2020-SOW-ESA-037-00001, uzsaukuma datums 10.10.2018).

Promocijas darba mērķis ir pārbaudīt Latvijas *GNSS CORS* tīklu (turpmāk darbā tie tiks saukti par Latvijas *CORS* tīkliem) stabilitāti. Šie tīkli tiek izmantoti veicot reālā laika kinemātiskos (angļu val. – *Real Time Kinematics; RTK*) un statiskos mērījumus. Lai sasniegtu

darba mērķi, šis pētījums, izmantojot statistisko analīzi, nosaka kinemātisko koordinātu nesaistes attiecībā pret publiski pieejamo informāciju par jonosfēras kopējo elektronu daudzumu (*TEC*) un *TEC* indeksa līmeņu izmaiņu ātrumu (angļu val. – *Rate Of change of TEC Index; ROTI*) vidējo platuma grādos, Latvijas reģionā, vienlaikus novērtējot kosmisko laikapstākļu ietekmi uz pozicionēšanas precizitāti un koordinātu stabilitāti 11 gadu laikā, kas aptver visu 24. Saules aktivitātes ciklu.

Šim nolūkam, izmantojot Latvijas *CORS* staciju *GPS* novērošanas datus, tika izstrādāta jauna metodika. Tā kā Latvijas *CORS* tīkli: LatPos un *EUPOS*<sup>®</sup>-Rīga, kas darbojas kopš 2007. gada (dažas stacijas kopš 2006. gada), kā arī starptautiskā *GPS/GNSS* servisa (angļu val. – *International GPS/GNSS Service; IGS*) / *EUREF* pastāvīgās darbības *GNSS* tīkla (angļu val. – *European Reference Frame Permanent GNSS Network; EPN*) stacija RIGA, nodrošina ievērojamu *GNSS* novērojumu datu bāzi, katram gadam (2007–2017) tika atlasītas datu kopas, 4–5 mēneši, ar augstu Saules aktivitāti, ģeomagnētiskām vētrām, Saules uzliesmojumiem un ekstremāliem *TEC* un *ROTI* līmeņiem. Izmantojot *Bernese GNSS programmatūras v5.2*, tika veikta datu pēcapstrāde. Tika iegūtas visu Latvijas *CORS* staciju 90 sekunžu kinemātiskās laika sērijas par laika posmu no 2007. līdz 2017. gadam, kā arī izveidota blokshēma datu analīzei un statistikai. Latvijas Universitātes Ģeodēzijas un ģeoinformātikas institūtā (LU ĢĢI) tika izstrādāti jauni programmatūras skripti Fortran g95 un Python programmēšanas valodā. Iegūtie rezultāti tika analizēti.

Korelācija tika meklēta starp laika sēriju novirzēm (turpmāk tekstā – kļūdainie risinājumi vai traucējumi) un nozīmīgiem kosmiskajiem laikapstākļiem. Tika pārbaudīti vairāk nekā 36 miljoni pozīcijas noteikšanas risinājumu. 0,6 % risinājumu bija kļūdaini. No visiem risinājumiem 0,01 % nesaiste bija lielāka par 50 metriem, 0,05 % nesaiste bija lielāka par 10 m, 0,13 % nesaiste bija lielāka par 1 m. Korelācija tika aprēķināta starp kļūdainajiem risinājumiem, *TEC* un *ROTI* līmeņiem un *Bernese GNSS programmatūras v5.2* atklātajiem cikliskās nenoteiktības lēcieniem. Promocijas darbs ietvēra arī vairākās stacijās vienlaicīgi novēroto kļūdaino risinājumu sadalījuma analīzi.

2015. gada 17. marta ģeomagnētiskā vētra bija visnozīmīgākais Saules aktivitātes notikums, kas radīja būtiskus (~500 m) pozicionēšanas traucējumus Latvijas *CORS* stacijās un korelēja ar augstu *TEC* līmeni. Ikmēneša pozicionēšanas nesaistes diagrammas atklāja vienlaicīgus kļūdainos risinājumus arī citās stacijās. Rezultātu analīzē tika konstatēts, ka vairākās stacijās kļūdainie risinājumi nereti parādās vairāk kā 150–200 reizes. Atkārtoto kļūdaino risinājumu parādīšanās tika pieņemta kā *GNSS* signāla zudums (angļu val. – *Loss-of-Lock*). Laika posmā no 2007. gada līdz 2017. gadam bija tikai viens Saules aktivitātes notikums,

kas korelēja ar augstu *TEC* līmeni. Veiktā Pīrsona korelācijas analīze atklāja, ka globālie *TEC* un *ROTI* tuvinājuma modeļi detalizēti neapraksta jonosfēras anomāliju neregularitātes.

Ņemot vērā to, ka vidējo platuma grādu reģioni tiek pētīti retāk, pētījums, kas veikts promocijas darba ietvaros sniedz izpratni par kosmisko laikapstākļu ietekmi uz *GPS* pozicionēšanas rezultātiem šajos reģionos. Analīze tiek veikta visam iepriekšējam (24.) Saules ciklam. Vēsturisko datu analīze sniedz informāciju par līdzīgām situācijām, kas varētu rasties nākamajā Saules ciklā.

Promocijas darba ietvaros veiktais pētījums ir pirmais solis, lai valsts līmenī aktualizētu izpratni par kosmisko laikapstākļu ietekmi uz *GNSS* pozicionēšanas rezultātiem Latvijā.

Promocijas darbā ietverti 33 attēli, 21 formula, 25 tabulas un divi pielikumi. Promocijas darba kopējais apjoms ir 93 lpp.

## ACKNOWLEDGMENTS

I am grateful to complete this Doctoral Thesis.

My gratitude goes to my mentors Dr. phys. Jānis Balodis and Dr. sc. ing. Inese Vārna who have supported me all the way into my scientific journey, who have given trust in me, in accomplishing my goals.

The Doctoral Thesis has been carried out at the LU GGI, thus my gratitude is sincerely expressed to each one of my colleagues – including Jānis Balodis, who apart from being my mentor is a former director and a heart of the LU GGI, as well as Gunārs Silabriedis, his successor, who's leadership and communication skills have added a new dynamic to it, and Ingus Mitrofanovs now our leader of the Institute. Augusts Rubans, Ansis Zariņš, Inese Vārna, Diāna Haritonova, Izolde Jumare, Marita Cekule, Irīna Baltmane, and Katerīna Morozova, from whom I have inspired by their example and learned as well, as who have magnificently helped me, in the accomplishment of this goal.

I express my gratitude to the professors from the bachelor, engineering and masters' degree study programmes for giving me the teachings and education which gave me the opportunity to pursue the doctoral degree study programme at Riga Technical University, thus my gratitude goes as well to the professors of the latter study programme.

My dearest family, each and everyone of them, they have motivated and believed in me through all these years.

# CONTENTS

|   |           |
|---|-----------|
| ANNOTATION.....   | 2         |
| ANOTĀCIJA .....   | 5         |
| ACKNOWLEDGMENTS.....  | 8         |
| ACRONYMS .....  | 10        |
| INTRODUCTION.....   | 13        |
| TOPICALITY OF THE DOCTORAL THESIS SUBJECT .....   | 13        |
| FORMULATION OF THE PROBLEM .....  | 18        |
| OBJECTIVE AND TASKS OF THE DOCTORAL THESIS.....   | 19        |
| SCIENTIFIC NOVELTY OF THE DOCTORAL THESIS .....   | 20        |
| PRACTICAL RELEVANCE OF THE DOCTORAL THESIS.....   | 20        |
| <b>1. SPACE WEATHER PHENOMENA.....</b>  | <b>22</b> |
| 1.1 SPACE WEATHER PHENOMENA CHARACTERISTICS .....   | 22        |
| 1.1.1 <i>Ionosphere</i> .....   | 22        |
| 1.1.1.1 Total Electron Content .....  | 25        |
| 1.1.1.2 Ionospheric disturbances characteristics.....   | 27        |
| 1.1.1.3 GPS to monitor ionosphere .....   | 28        |
| 1.1.1.4 Ionospheric effects on GNSS Signals.....  | 29        |
| 1.1.2 <i>Solar flare</i> .....  | 30        |
| 1.1.3 <i>Geomagnetic storms</i> .....   | 32        |
| 1.1.3.1 Geomagnetic indices .....   | 35        |
| 1.2 DATA SOURCES .....  | 36        |
| <b>2. METHODOLOGY OF ANALYSIS OF SPACE WEATHER IMPACT ON LATVIAN CORS IN<br/>2007–2017.....</b> | <b>39</b> |
| 2.1 TIME FRAME .....  | 39        |
| 2.2 DATA .....  | 40        |
| 2.2.1 <i>Latvian CORS networks and IGS/EPN station RIGA</i> .....                               | 40        |
| 2.2.2 <i>Data selection</i> .....   | 42        |
| 2.3 THE DEVELOPED METHOD.....   | 43        |
| 2.3.1 <i>Data processing</i> .....  | 43        |
| 2.3.1.1 primary processing OF CORS Observation data applying Bernese GNSS Software v5.2.....    | 44        |
| 2.3.2 <i>Flowchart of analysis processing functions and related data sets</i> .....             | 46        |
| <b>3. RESULTS .....</b>   | <b>50</b> |
| 3.1 MONTHLY MEAN STATION COORDINATES .....  | 50        |
| 3.2 DISTRIBUTION OF THE SIZE OF DISCREPANCIES.....  | 51        |
| 3.3 “EVIL WAVE” OF DISTURBANCES .....   | 52        |
| 3.4 LOSS OF LOCK SITUATIONS .....   | 58        |
| 3.5 CORRELATION ANALYSIS .....  | 63        |
| 3.6 ROTI CORRELATION ANALYSIS .....   | 67        |
| 3.7 ESTIMATION OF THE RELATION BETWEEN THE COUNT OF FAULTY SOLUTIONS AND TEC-MAX.....           | 70        |
| <b>4. ADDITIONAL SPACE WEATHER TESTS FOR EGNOS RIMS GROUND STATIONS.....</b>                    | <b>72</b> |
| <b>CONCLUSIONS .....</b>  | <b>81</b> |
| <b>APPENDICES.....</b>  | <b>83</b> |
| <b>LIST OF REFERENCES.....</b>  | <b>85</b> |

## ACRONYMS

|                               |  |
|-------------------------------|--|
| ACE                           | Advanced Composition Explorer  |
| AIUB                          | Astronomical Institute of the University of Bern   |
| AS                            | Anti-Spoofing  |
| BeiDou                        | Chinese Navigation Satellite System  |
| CDDIS                         | Crustal Dynamics Data Information System is NASA's data archive and information service supporting the international space geodesy community |
| CMEs                          | Coronal mass ejections   |
| C/NOFS                        | Communications/Navigation Outage Forecasting System satellite  |
| CODE                          | Center for Orbit Determination in Europe, Astronomical Institute, University of Berne, Switzerland   |
| CORS                          | Continuously Operating Reference Station   |
| COSMIC                        | Constellation Observing System for Meteorology, Ionosphere, and Climate  |
| CPF                           | EGNOS Central Processing Facility  |
| CSLP                          | Cycle slips  |
| DLR                           | Deutsches Zentrum für Luft und Raumfahrt   |
| DMSP                          | Defense Meteorological Satellite Program   |
| DOMES                         | Directory of MERIT Sites   |
| DSCOVR                        | Deep Space Climate Observatory   |
| Dst                           | Disturbance storm time   |
| ECAC                          | European Civil Aviation Conference   |
| EGNOS                         | European Geostationary Navigation Overlay Service  |
| EPN                           | EUREF Permanent GNSS Network   |
| EPOS                          | European Plate Observing System  |
| ESA                           | European Space Agency  |
| ESM                           | Extended Slab Model <i>mapping function</i>  |
| ESOC                          | European Space Operations Center of ESA, Darmstadt, Germany  |
| <i>EUPOS</i> <sup>®</sup>     | European Position Determination System   |
| <i>EUPOS</i> <sup>®</sup> ISC | International <i>EUPOS</i> <sup>®</sup> <i>Steering Committee</i>  |
| EUREF                         | Regional Reference Frame Sub-Commission for Europe   |
| EUV                           | Extreme ultraviolet  |
| EUVN_DA                       | European Vertical Network Densification Action   |

|         |   |
|---------|---|
| EWF     | Evil Wave Forms   |
| FOC     | Full Operational Capability   |
| GALILEO | Europe’s Global Navigation Satellite System   |
| GBAS    | Ground Based Augmentation System  |
| GFZ     | Deutsches GeoForschungsZentrum; German Research Centre for Geosciences  |
| GNSS    | Global Navigation Satellite Systems   |
| GLONASS | ГЛОБАЛЬНАЯ НАВИГАЦИОННАЯ СПУТНИКОВАЯ СИСТЕМА; GLObalnaya NAVigatsionnaya Sputnikovaya Sistema, the Russian positioning system |
| GPS     | Global Positioning System, the U.S. positioning system  |
| GRACE   | Gravity Recovery and Climate Experiment satellites  |
| HAF     | Highest affected frequency  |
| HSNAV   | Horizon Framework Programme for Research and Innovation in Satellite Navigation   |
| IAAC    | Ionosphere Associate Analysis Centers   |
| IAGA    | International Association of Geomagnetism and Aeronomy  |
| ICAO    | International Civil Aviation Organization   |
| IDM     | Ion Drift Meter   |
| IGS     | International GPS/ GNSS Service   |
| ILS     | Instrument Landing System   |
| IMF     | Interplanetary Magnetic Field   |
| IONEX   | Ionosphere exchange format  |
| ISES    | International Solar Energy Society  |
| ISGI    | International Services for Geomagnetic Indices  |
| iTEC    | ionospheric total electron content  |
| ITRF    | International Terrestrial Reference Frame   |
| JPL     | Jet Propulsion Laboratory, Pasadena, California, U.S.A  |
| LC      | Linear Combination  |
| LEO     | Low Earth Orbit   |
| LGIA    | Latvian Geospatial Agency   |
| LU GGI  | Institute of Geodesy and Geoinformatics, University of Latvia   |
| MLT     | Magnetic Local Time   |
| MSLM    | “Modified” Single-Layer Model   |
| MUF     | Maximum usable frequency  |
| NASA    | National Aeronautics and Space Administration   |

|       |   |
|-------|---|
| NOAA  | National Oceanic and Atmospheric Administration                               |
| nT    | nanoTeslas  |
| PECS  | ESA's Plan for European Cooperating States programme                          |
| QZSS  | Quasi-Zenith Satellite System (Japanese satellite positioning system)         |
| RIMS  | Ranging Integrity Monitoring Stations   |
| RINEX | Receiver INdependent Exchange format  |
| RO    | Radio occultation   |
| ROT   | Rate Of change of TEC   |
| ROTI  | ROT index   |
| RPA   | Retarding Potential Analyzer  |
| RTK   | Real Time Kinematics  |
| SBAS  | Satellite-Based Augmentation Systems  |
| SLM   | Single-Layer Model  |
| SOHO  | the joint NASA-ESA Solar and Heliospheric Observatory mission                 |
| SoL   | Safety of Life  |
| SSIES | Special Sensor-Ions Electrons Scintillation thermal plasma instrument package |
| SSN   | Sunspot Number  |
| STEC  | Slant Total Electron Content  |
| TEC   | Total Electron Content  |
| TECU  | Total Electron Content Unit   |
| TIDs  | Travelling Ionospheric Disturbances   |
| TSX   | Terra SAR-X satellite   |
| UPC   | Technical University of Catalonia, Barcelona, Spain                           |
| UT    | Universal time day  |
| UV    | Ultraviolet   |
| VHF   | Very high frequency   |
| VTEC  | Vertical Total Electron Content   |
| WAAS  | American Wide Area Augmentation System  |
| XRS   | X Ray Sensor  |

# INTRODUCTION

## **Topicality of the Doctoral Thesis subject**

The term “space weather” generally refers to conditions on the Sun, in the solar wind, and within the Earth's magnetosphere, ionosphere and thermosphere that can influence the performance and reliability of space-borne and ground-based technological systems and can endanger human life or health (definition used in the U.S. National Space Weather Plan).

The research on space weather, thus the characteristics of ionosphere, has become more and more a subject of interest over the last decade.

Several countries have put the subject of a high importance at a national level. The executive office of the president of the United States, space weather operations, research, and mitigation working group, space weather, security, and hazards subcommittee, committee on homeland and national security of the national science and technology council have developed “The National Space Weather Strategy and Action Plan”, where strategic objectives and high-level actions necessary to achieve a space-weather-ready Nation have been identified (Weather Operations and Mitigation Working Group, 2019).

One of the three objectives of the “National space weather strategy and action plan” is to “develop and disseminate accurate and timely space weather characterization and forecasts” (Weather Operations and Mitigation Working Group, 2019). Characterization includes measurement, assessment, and modelling of the space weather environment to inform nowcasts, situational awareness, historical studies, forensics, and attribution (Weather Operations and Mitigation Working Group, 2019).

Improving the understanding and characterization of the effects space weather phenomena have on Earth and in the space environment can improve situational awareness, informing decision-making and enabling the execution of missions that depend on technologies and services susceptible to disruptions from space weather (Weather Operations and Mitigation Working Group, 2019).

It is important to identify and release, as appropriate, new or previously underutilized data sets. Greater access to existing data sets could improve the development, validation, and testing of models used for characterizing and forecasting space weather events (Weather Operations and Mitigation Working Group, 2019). In order to predict ionospheric characteristics, it is effective to use models considering the state of the ionosphere in the past, as well as the history of parameters characterizing the main impact on the ionosphere from above – solar and magnetic activity (Salimov et. al. 2023).

In the United Kingdom the risk from space weather was added to the National Risk Register in 2011 (Sverige. Myndigheten för samhällsskydd och beredskap, 2012), and later in 2017, the United Kingdom included space weather as one of the natural hazards risks in the “National Risk Register of Civil Emergencies” (National Risk Register of Civil Emergencies 2017 Edition, 2017). Norway included space weather in its National Vulnerability and Preparedness Report (in Norwegian – *Nasjonal sårbarhets och beredskapsrapport; NSBR*) in 2012. In the Netherlands the impact of space weather is considered as part of the work underpinning the National Safety and Security Strategy. Sweden in 2012 was dealing with a risk scenario involving GNSS disruptions as part of its national risk assessment and since then is developing further work on scenarios based on space weather impacts (Sverige. Myndigheten för samhällsskydd och beredskap, 2012).

These documents of the United States and United Kingdom as well as of other countries mentioned above show the importance of space weather impact worldwide and importance of its acknowledgement also at the national level.

United States of America and United Kingdom have a clear vision at the national level for the tasks to be completed in order to achieve the goals described above.

The great importance on this subject has been highlighted by the European Space Agency (ESA) as well.

In order to achieve the goals above, which, in fact, can easily be generalized for every country, there are several projects dedicated to this subject worldwide.

For example, one of such initiatives under the Delegation Agreement by European Commission was undertaken by ESA. It is the Horizon 2020 Framework Programme for Research and Innovation in Satellite Navigation (HSNAV), where ESA stands for its technical as well as management implementation (H2020 HSNAV home page).

Within this programme one of the ongoing projects is Evil Waveform and Ionospheric Characterization Monitoring Network (H2020 HSNAV home page).

The objective of this activity is to monitor the different GNSS signals, extending the current capabilities of the MONITOR network and to exploit the database to provide relevant input for the evolution of European Geostationary Navigation Overlay Service (EGNOS) V3 (updated models and reference scenarios, statistics and specifications, worst-case estimates, representative data samples, etc.). Thus, the objective of this activity is broken up into two main parts:

- a) monitoring and analysis of Evil Wave Forms (EWF) also known as a non-nominal signal distortions;

b) monitoring, analysis, and characterization (including development of technical specifications) of environmental effects due to ionosphere (H2020 HSNAV home page).

The term “evil waveform” is used to denote the disturbed information for navigation in some area caused by the GPS clock error (Julien et al. 2017). The term “evil wave” in the Doctoral Thesis is used to describe the changing distribution of positioning discrepancies over the territory of Latvia in some time period.

The above described examples and multiple studies carried out in many institutions worldwide show that there is a strong topicality of space weather phenomena research.

In space weather research, the investigations of ionospheric storm effects are of fundamental importance (Yang et al. 2020). Space weather phenomena are much more investigated at the high latitudes and equatorial latitudes, because the evidence is more frequent and the impact is higher in these regions. The impact is more severe at high latitudes, while at low latitudes the impact is associated with different types of ionospheric disturbance. By contrast, midlatitude irregularities are less severe, and they are usually attributed to expansion of auroral and/or equatorial irregularities under disturbed conditions (Yang et al. 2020).

The hypothesis of the Doctoral Thesis is as follows: Midlatitude TEC irregularities and space weather impact are less severe (Yang et al. 2020). Is it true?

Historically midlatitude areas were less investigated, thus only little investments and research were dedicated to these phenomena in these regions (Skone 2001), however the situation has evolved.

Spogli et al. (2009) discussed the possibility to investigate the dynamics of ionospheric irregularities causing scintillation by combining the information coming from a wide range of latitudes. The authors analysed the data of ionospheric scintillation from latitudes 44–88° N during October, November and December 2003.

Similar work has been carried out in Belgium by Stankov et al. (2009) by studying GPS signal delay during geomagnetic storms of 29 October and 20 November, 2003. The anomalous movement of ionosphere walls were searched (Stankov, Warnant, and Stegen 2009). Similar ionospheric gradients were found. Instead of the traditional Instrument Landing System (ILS), several as a prototype chosen airports have used systems for GNSS landings and takeoffs. These prototype airports are in areas in which the occurrence of scintillations is negligible (Mayer et al. 2009; Circiu et al. 2014; Lee and Lee 2019). Stankov et al. (2009) suggest that one important objective is to assess the integrity risk to Ground Based Augmentation System (GBAS)/Satellite Based Augmentation System (SBAS) services.

Chinese researchers had studied the variation characteristics of the GPS-based TEC fluctuations over 21 regions of China (Liu et al. 2016). They studied the fluctuation intensity in

various latitudes, in daytime and nighttime, during winter and summer. The ROTI indices was used to investigate the characteristics of the ionospheric TEC fluctuations during 11-year solar cycle 2002–2012 (X. Liu et al. 2016).

To classify the relevant orders of the magnitude and the occurrence rates, Hlubek et al. (2014) employed a statistical approach, and large amounts of measured data were aggregated. The research by Hlubek et al. (2014) concludes that a double peak structure with the greatest scintillation intensity was observed during the spring and autumn equinoxes.

The research on the correlation between GNSS-derived ionospheric spatial de-correlation and space weather intensity for safety-critical differential GNSS systems was carried out by Lee and Lee (2019).

Over the last decade, space weather has been one of the subjects of the conducted research at the LU GGI. This theme is reflected in publications by Balodis et al. (2017) and Balodis, Varna, and Normand (2018), which were the inspiration for further research as presented in the frame of this Doctoral Thesis. The article, published in Remote Sensing Journal (Balodis, Normand, and Varna, 2021) presents part of the results obtained in completion of the ESA project carried out at the LU GGI (2019–2021). The continuation of this research is represented in publication “The Movement of GPS Positioning Discrepancy Clouds at a Mid-Latitude Region in March 2015” (Balodis, Normand, and Ansis Zarins, 2023).

According to the above mentioned, as well as taking into account the ESA’s priorities in research related to space weather, and Latvia being one of the countries in the ESA’s Plan for European Cooperating States (PECS) programme, the subject is of a significant importance.

Latvia became the seventh ESA European Cooperating State on March 19, 2013, and on June 30, 2020, it became an Associate Member (ESA home page).

The research on space weather phenomena in Latvia has become possible within the development and implementation of CORS networks LatPos (Zvirgzds 2012) and *EUPOS*<sup>®</sup>-Riga (Silabriedis 2012). LatPos and *EUPOS*<sup>®</sup>-Riga CORS stations are operating since 2007 (some stations since 2006). The initiation of these two networks, which were developed in the frame of *EUPOS*<sup>®</sup> regional development project, was in 1992, when the first GPS measuring campaign was carried out. More information can be found in publications by Balodis et al. (2015) as well as by Madsen and Madsen (1993).

General information on both networks can be found in (Zvirgzds 2007; Zvirgzds 2012; and Abele et al. 2008).

Technical aspects on the implementation of Latvian CORS followed the *EUPOS*<sup>®</sup> ISC (International *EUPOS*<sup>®</sup> Steering Committee) specifications (*EUPOS*<sup>®</sup> ISC 2013).

Since their implementation, LatPos and *EUPOS*<sup>®</sup>-Riga networks (as well as IGS/EPN station RIGA) have been a great source of different high-level research conducted in Latvia. Some examples include ionospheric research studies by Dobelis, Zvirgzds, and Kaļinka (2017), studies on the geophysical processes in Latvia by Haritonova (2016), as well as the geoid related research by Janpaule (2014), Kaminskis (2010) and Morozova (2022). Most part of these studies have been carried out in the Doctoral Thesis. As mentioned previously – over the last decade, data from LatPos and *EUPOS*<sup>®</sup>-Riga networks (as well as IGS/EPN station RIGA) has been applied on the research related to space weather phenomena and to the ionosphere as well.

Therefore, as the observation data of the Latvian CORS stations is widely used in various high level studies, as well as in civil engineering tasks, machine guiding, etc., the conducted research in the frame of the Doctoral Thesis, including the Latvian CORS stability control in relation to space weather impact over an 11-year timeframe, is essential in Latvian CORS stations analysis. The analysis is performed over entire solar cycle. This historical analysis is giving information on the similar situations that will arise in the next solar cycle.

Data and information on the risks from extreme space weather are fragmented across governments and the private sector and still largely unavailable to decision-makers and at-risk populations. A positive trend is that the risks from extreme space weather are increasingly included in national risk assessments. National processes for risk assessment provide important vehicles for coherence and cross-sectoral coordination. (Sverige. Myndigheten för samhällsskydd och beredskap, 2012).

The research conducted in the frame of this Doctoral Thesis is the first step to raise the awareness of space weather impact on GNSS positioning results in Latvia at a national level.

## Formulation of the problem

The impact of space weather on the GNSS positioning, navigation, and timing has been recognized as a serious threat (Sreeja 2016) to the operational quality of GBAS and SBAS, and for many other positioning and navigation applications as well, such as remote sensing vehicles, satellites, aviation, cars, trucks, agriculture, construction, snow removal, etc. Distortion of GNSS signals is of concern for many applications, especially those related to Safety-of-Life (SoL).

The results of the research, obtained within the framework of the Doctoral Thesis, could indicate that similar effects may occur in GBAS (and that they may be detected in a similar fashion) and in regional SBAS (for example EGNOS). This way, critical SoL services and their applications could be compromised during extreme solar events. Amongst others, the main EGNOS SoL service objective is to support civil aviation operations. Since April 1993, Latvia is also a part of the European Civil Aviation Conference (ECAC) (ECAC home page), which means that in order to meet International Civil Aviation Organization's (ICAO) standards for precision approaches, the EGNOS Central Processing Facility (CPF) is used in Latvia as well. It could become even more critical over the territory of Latvia, taking into account that the physical border of the EGNOS Ranging Integrity Monitoring Stations (RIMS) network almost coincides with the border of the territory of Latvia.

Thus, these results obtained in this Doctoral Thesis could serve as a warning sign and would potentially indicate the necessity to raise the topic at a national level.

Diverse approaches on how to identify and characterize the space weather phenomena on the ground-based segment and space-based segment are investigated worldwide, e.g. by Spogli et al. (2009), Stankov, Warnant, and Stegen (2009), Liu et al. (2016), Hlubek et al. (2014), Lee and Lee (2019), Cherniak, Zakharenkova, and Redmon (2015), Morozova et al. (2020), Astafyeva, Zakharenkova, and Förster (2015), Jacobsen and Andalsvik (2016), (Liu et al. (2016), Balasis, Papadimitriou, and Boutsis (2019), Park et al. (2017), and Jin et al. (2019) and are briefly presented in Section 1.2 of the Doctoral Thesis.

The lack of ground-based infrastructure, such as ionosondes, digital ionosondes, dynasondes (NOAA home page), magnetometers, etc., in certain areas is a limiting factor of the related research approaches when tackling this subject. It has been emphasized above in this chapter, and stated by Skone (2001) that in midlatitudes less investments were dedicated, thus less research performed.

However, over the last decade, Spogli et al. (2009), Stankov et al. (2009), Mayer et al. (2009), Circiu et al. (2014), Lee and Lee (2019), Liu et al. (2016), Hlubek et al. (2014) conducted research on the subject in the area of midlatitude. The challenge of the scientific community is to make the research possible in every part of the world, therefore to find a way on how to identify and characterize space weather phenomena by using the infrastructure already in place in that specific area (latitude), if no additional funds are dedicated; as well as to develop new infrastructure, new software and software scripts related to the specific research, when possible.

Accordingly, in Latvia, in the frame of the Doctoral Thesis, it includes the use of a new methodology based only on CORS GPS observation data to identify and characterize the impact of space weather phenomena on GPS positioning results, detected through ionospheric disturbances; *Bernese GNSS Software v5.2* for the GPS observation data post-processing; creation of the flowchart for the data analysis and statistics; and new software scripts developed in g95 Fortran and Python programming languages at the LU GGI.

## **Objective and tasks of the Doctoral Thesis**

The objective of the Doctoral Thesis is to verify the stability of the Latvian CORS networks, used for RTK and static measurements, in connection with space weather impact on positioning accuracy and coordinate stability over an 11-year period covering the whole 24th cycle of solar activity, by means of the statistical analysis of kinematic coordinate discrepancies in relation to the publicly available ionospheric TEC and ROTI levels, in the midlatitude region – Latvia.

The main tasks are:

- 1) to discover the amount of disturbed results and to characterize the statistics of disturbance size;
- 2) to analyse correlation of disturbances to TEC and ROTI;
- 3) to find the most influenced CORS stations and to characterize the conclusions on the reason of network affected instability.

## **Scientific novelty of the Doctoral Thesis**

The scientific novelty of the present Doctoral Thesis is the developed and applied methodology, which is original, has not been implemented before, and relies on the following achievements.

For the first time the Latvian CORS GPS positioning data for the whole solar cycle of 11 years (2007–2017) has been analysed and has been post processed in a 90-second kinematic mode using *Bernese GNSS Software v5.2*.

- 1) Latvian CORS stability control in relation to space weather impact, has been summarized by discovering the discrepancies in positioning results.
- 2) Pearson's correlation analysis method gave the opportunity to assess the relation between the ionospheric TEC levels and the frequency of disturbed positioning results, as well as the frequency of those cycle slips which were identified by the *Bernese GNSS Software v5.2*. Pearson's correlation analysis method gave the opportunity to assess the relation between the ROTI indices level and the frequency of disturbed positioning results.
- 3) Consequently, the applied method gave the opportunity to assess the suitability of the global TEC and ROTI approximation models for the local ionospheric anomalies as well as to discover simultaneous discrepancies at numerous individual stations. This allowed to characterize the irregularities of global ionospheric models.
- 4) The monthly discrepancy diagrams revealed the movement of space weather influenced "discrepancy clouds" which have been studied in post-doctoral thesis publication by Balodis, Normand, and Zarins (2023).

## **Practical relevance of the Doctoral Thesis**

This type of information on the analysis of the 11-year selective daily GPS observations of the Latvian CORS, with an emphasis on significant space weather events is necessary in the region of Latvia (latitude around 57°N) like elsewhere in the world.

The main practical gain as a result of reaching the objective of this Doctoral Thesis is the characteristics and analysis of the impact of space weather phenomena and ionospheric disturbances on the GPS observation data, collected at Latvian CORS stations, over an 11-year time span. The result is an understanding of the space weather processes that are influencing

GPS observation data in the midlatitude region (around 57°N); therefore, it is the first research conducted over the territory of Latvia based on collected GPS observation data over an 11-year period, as well as being the first one of its kind of research in midlatitude regions in general.

It is important to understand that beside the multipath the additional source of errors in GNSS measurements is also the space weather impact and to be aware of ionospheric TEC irregularities.

This research brings the knowledge of the necessity to increase the awareness of this subject at a national level. It is of a dual application:

1) in national economy, i.e. for the GNSS users in land surveying, civil engineering tasks and navigation (automotive guidance machines, road construction, etc.), and for many other positioning tasks;

2) in national defence where GNSS is widely used for drones' guidance and for multiple usage in artillery applications.

Therefore, within the framework of the Doctoral Thesis the topicality and the awareness of space weather phenomena, and its impact on GPS observations in Latvia, is revealed.

The research in the frame of the Doctoral Thesis on space weather phenomena serves as a basis for future research as well as the basis for increasing the awareness on this subject at a national level.

Taking into the consideration that the processes in the nature are constantly changing, global climate is evolving, and the atmospheric irregularities are changing, the awareness of this subject in latitudes around 57°N is significantly important in the future. The use of GNSS positioning is increasing in various applications as is the awareness of space weather impact on GNSS observations.

This subject will be of a particular interest in the upcoming years due to the fact that a new solar activity cycle (25th) has begun.

Up until now no such methodology has been applied for the research of the impact of space weather on GPS positioning results; therefore, this study provides an opportunity to combine the learned practices to achieve common goals in the future, expanding the research in a wider area and filling the gap in the research of space weather phenomena in this region.

# 1. SPACE WEATHER PHENOMENA

As stated in the introduction section: “The term “space weather” generally refers to conditions on the Sun, in the solar wind, and within the Earth’s magnetosphere, ionosphere and thermosphere that can influence the performance and reliability of space-borne and ground-based technological systems and can endanger human life or health” (definition used in the U.S. National Space Weather Plan).

This chapter focuses on space weather phenomena, with a special emphasis to those affecting GPS/(GNSS) observation data.

## 1.1 Space weather phenomena characteristics

Space weather can occur anywhere from the surface of the Sun to the surface of Earth. As a space weather storm leaves the Sun, it passes through the corona and into the solar wind. When it reaches Earth, it energizes Earth’s magnetosphere and accelerates electrons and protons down to Earth’s magnetic field lines where they collide with the neutral atmosphere and ionosphere, particularly at high latitudes (NOAA home page).

### 1.1.1 IONOSPHERE

The ionosphere is a weakly ionized plasma or gas, that is formed by the ultraviolet (UV) ionizing radiation from the Sun.

Solar flare, that is a significant emission of X-radiation, creating important additional photo ionization in the ionosphere, directly affects the ionosphere which can affect the radio wave propagation in various ways. Solar flares also release energetic particles into space (ESA home page; Amory-Mazaudier et al. 2017; Parkinson and Spilker Jr. 1995). Solar flare is discussed further on in the Section 1.1.2.

The spatial distribution of electrons and ions is mainly determined by photo-chemical processes and transportation processes. Both processes create different regions of ionized gas in different altitudes (Dach et al. 2015). The degree of ionization does not uniformly increase with the distance from the Earth’s surface. There are regions of ionization D, E and F1 and F2, that have special characteristics as a result of variation in the extreme ultraviolet (EUV)

absorption, the predominant type of ions present, or pathways generated by the electromagnetic field (Leick 2004).

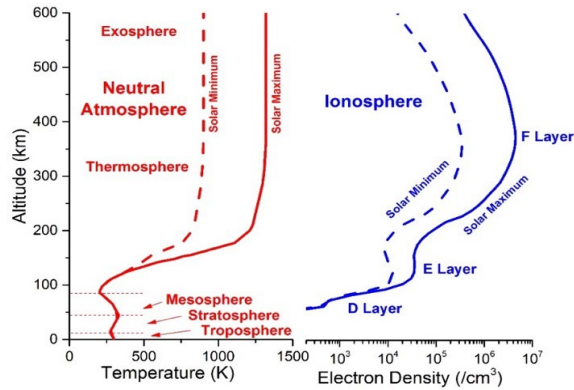


Fig. 1.1. Height profiles of the neutral atmosphere temperature and the ionosphere electron density for daytime solar minimum and solar maximum conditions (layers, further on referred to as regions) of the neutral atmosphere and ionosphere are labelled for reference) (Weather Operations et al. 2018).

Fig. 1.1 illustrates the different regions and their electron densities in the ionosphere. The D, E, and F1 regions are closely tied to the UV ionizing daytime radiation from the Sun, and are not present at night. The F2 region is present at night, but it is lower in density and generally has its maximum density at a greater height during the night, as compared with daytime (Parkinson and Spilker Jr. 1995 and El-Rabanny 2006).

The degree of ionization shows large variations which are correlated with the solar activity, the geomagnetic activity plays an important role, too. The solar activity may be characterized, e.g. by the sunspot number, where one observes an 11-year cycle besides an 80-100-year super-cycle. Solar cycle progression by sunspot number is represented in (SpaceWeatherLive home page). Fig. 1.2 shows the monthly and smoothed sunspot numbers in the time period from 2007 to 2017, used in the Doctoral Thesis for data analysis (Dach et al. 2015).

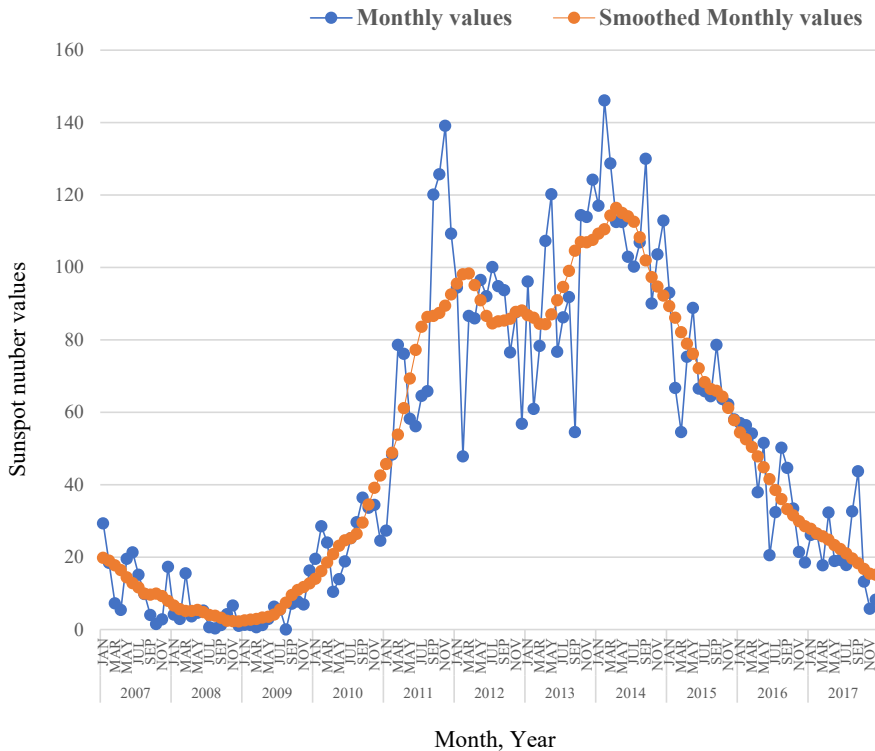


Fig. 1.2. Monthly and smoothed sunspot numbers (SSN), year 2007–2017; data gathered from: (NOAA home page).

The major characteristics and importance of each region of the ionosphere for potential effects on GPS signals are summarized as follows, taking into account, that all heights given are only approximate:

1) D region, 50–90 km: This region, produced by ionization of several molecular species from hard x rays and solar Lyman  $\alpha$  radiation, causes absorption of radio signals at frequencies up to the low very high frequency (VHF) band, and has no measurable effect on GPS frequencies.

2) E region, 90–140 km: the normal E region, produced by solar soft x rays, has a minimal effect on GPS. An intense E region, with irregular structure, produced by solar particle precipitation in the auroral region, might cause minor scintillation effects. Sporadic E region, still of unknown origin, is very thin and also has a negligible effect at GPS frequencies.

3) F1 region, 140–210 km: The normal F1 region, combined with E region, can account for up to 10 % of the ionospheric time delay encountered by GPS. Diffusion is not important at F1 region heights, and, as with the normal E region, it has a highly predictable density from

known solar emissions. The F1 region is produced through ionization of molecular species, and its electron density nicely merges into bottom side of the F2 region.

4) F2 region, 210–1,000 km: The F2 region is the densest and it also has the highest variability, causing most of the potential effects on GPS receiving systems. The height of the peak of the electron density of the F2 region generally varies from 250 to 400 km, but it can be even much higher or somewhat lower under extreme conditions. The F2 region is produced mainly from ionization of atomic oxygen, which is the principal constituent of the neutral atmosphere at those heights. The F2, and to some extent the F1, regions cause most of the problems for radio wave propagation at GPS frequencies.

5)  $H^+ > 1,000$  km: The protonosphere, is a region of ionized hydrogen, with a lesser contribution from helium gas. It is of low density, but extends out to approximately the orbital height of GPS satellites. It can be a significant source of unknown electron density and consequent variability of time delay for GPS users. Estimates of the contribution of the protonosphere vary from 10 % of the total ionospheric time delay during daytime hours, when electron density of the F2 region is highest, to approximately 50 % during the nighttime, when the F2 region density is low. The electron content of the protonosphere does not change by a large amount during the day, but is depleted during major magnetic storms and can take several days to recover to prestorm values (Parkinson and Spilker Jr. 1995).

### 1.1.1.1 TOTAL ELECTRON CONTENT

The state of the ionosphere may be described by the electron density  $n_e$  in units of electrons per cubic meter. The impact of the state of the ionosphere on the propagation of radio waves is characterized by the Total Electron Content (TEC)  $E$ :

$$E = \int_k^i n_e(s) ds \quad (1.1)$$

The integral gives the total number of free electrons included in a rotation cylinder with a cross-section area of one square meter, aligned along the signal path  $s$  between receiver  $k$  and satellite  $i$ . In geodetic applications, the TEC  $E$  is measured in so-called total electron content units (TECU), where one TECU corresponds to  $10^{16}$  electrons per square meter ( $10^{16}/m^2$ ). For comparisons, the vertical TEC  $E_V$  is formed as

$$E_V = E \cos z' \quad (1.2)$$

where  $z'$  is the zenith distance of the signal path with respect to the vertical mean altitude of the ionospheric shell.

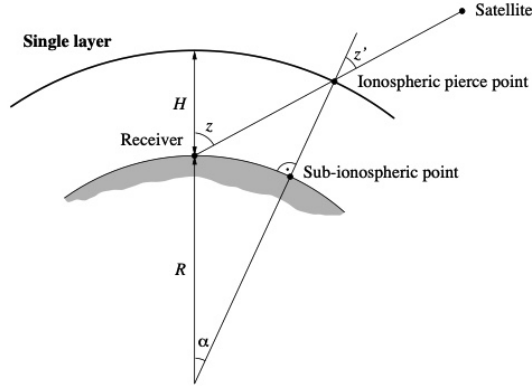


Fig. 1.3. Single-layer model (Dach et al. 2015).

GNSS-derived ionosphere models describing the deterministic component of the ionosphere are usually based on the so-called Single-Layer Model (SLM) as outlined in Figure 1.3. This model assumes that all free electrons are concentrated in a shell of infinitesimal thickness. The SLM mapping function  $F_I$  may be written using the equation (1.2) as

$$F_I(z) = \frac{E}{E_V} = \frac{1}{\cos z'} \quad (1.3)$$

$$\text{with } \sin z' = \frac{R}{R+H} \sin z \quad (1.4)$$

$z, z'$  are the zenith distances at the heights of the station and of the single layer, respectively,  $R$  is the mean radius of the Earth, and  $H$  is the height of the single layer above the Earth's surface.

The geocentric angle  $\alpha$  equals  $z - z'$ .

The height of this idealized layer is usually set to the expected height of the maximum electron density. Furthermore, the electron density  $E$  – the surface density of the layer is assumed to be a function of geographic or geomagnetic latitude  $\beta$  and Sun-fixed longitude  $s$ .

The “modified” SLM (MSLM) mapping function includes an additional constant,  $\alpha$  (Schaer 1999):

$$F_I(z) = \frac{E}{E_V} = \frac{1}{\cos z'} \quad (1.5)$$

$$\text{with } \sin z' = \frac{R}{R+H} \sin(\alpha z). \quad (1.6)$$

Best fit of the equation (1.6) with respect to the Jet Propulsion Laboratory, Pasadena, California, U.S.A (JPL) extended slab model (ESM) mapping function is achieved at  $H = 506,7$  km and  $\alpha = 0,9782$  (when using  $R = 6371$  km and assuming a maximum zenith distance of 80 degrees). The resulting mapping function is used in the ionosphere analysis at Center for Orbit Determination in Europe, Astronomical Institute, University of Berne, Switzerland (CODE).

For computation of the ionospheric pierce points,  $H = 450$  km is assumed for ground stations (Dach et al. 2015).

### 1.1.1.2 IONOSPHERIC DISTURBANCES CHARACTERISTICS

The ionospheric disturbances, which are driven primarily by three types of space weather phenomena, i.e. solar flares, solar energetic particle events and geomagnetic storms, can affect the propagation speed and direction of all radio (communication, navigation and timing) signals, including GNSS, i.e. GPS, GLONASS (ГЛОБАЛЬНАЯ НАВИГАЦИОННАЯ СПУТНИКОВАЯ СИСТЕМА – Russian Global Navigation Satellite System), GALILEO, BeiDou (Chinese Navigation Satellite System), QZSS (Quasi-Zenith Satellite System/Japanese satellite positioning system). For GNSS this reduces the positioning accuracy (Colvin and Thomas 2019).

Particularly significant space weather phenomena events inducing ionospheric disturbances can even lead to a loss of lock between satellite and receiver (loss of signal reception), which can delay or completely invalidate a positioning solution. Basically every GNSS user is affected, especially users that have high requirements for accuracy, integrity, availability, and continuity, e.g. in marine and aviation, agriculture, snow removal, construction, exploration, surveying, and other critical real-time applications (Coster and Komjathy 2008).

The characteristics of ionospheric disturbances that are affected by space weather phenomena and are analysed by the scientific community worldwide include slant TEC (STEC) and vertical TEC (VTEC), which is calculated from STEC. Vertical electron content values can more easily be compared than slant values observed at various elevation angles (Parkinson and Spilker Jr. 1995) by assuming a thin shell ionosphere at 400 km altitude (Sripathi et al. 2008) or 450 km as of Dach et al. (2015). As well as they include ROTI – the GPS TEC fluctuations, which provide information on large-scale irregularities of electron density from several to several hundred kilometers (Li et al. 2011) and ionosphere scintillation indices that describe the electron density irregularities. The ionosphere can become turbulent due to small-scale irregularities that alter the amplitude and phase of transmitted signals. The term “ionospheric scintillation” is often used to describe this phenomenon (Weather Operations et al. 2018) in the ionosphere:  $\sigma\phi$  (sigma-phi) – phase scintillation index and  $S4$  index which characterizes the scintillation of the signal amplitude, that is predominant in equatorial latitude. It allows to calculate a unique,  $S4$  index for each GNSS signal. The indices reflect the variability of the signal over a period of time, usually one minute. Scintillation is more prevalent at low and high

latitudes, but midlatitudes, experience scintillation much less frequently. Scintillation is a strong function of local time, season, geomagnetic activity, and solar cycle but it also is influenced by waves propagating from the lower atmosphere (NOAA home page; Hlubek et al. 2014).

TEC response to space weather events consists of either changes of the amplitude and the shape of the regular daily TEC variations observed world-wide or a phenomenon called travelling ionospheric disturbances (TIDs) which are observed on smaller spatio-temporal scales (Morozova, Barlyaeva, and Barata 2020).

Other characteristics of ionospheric disturbances that are affected by space weather phenomena and are analysed are: height of the F2 layer (hmF2) as well as peak density of the F2 layer (NmF2) and highest affected frequency (HAF), maximum usable frequency (MUF) (Colvin and Thomas 2019; Weather Operations et al. 2018; Coster and Komjathy 2008).

### **1.1.1.3 GPS TO MONITOR IONOSPHERE**

Within the development of GPS and the launch of first experimental GPS satellites (between 1978–1985) ionospheric scientists recognized that the GPS dual-frequency measurements could be used to monitor ionosphere and to measure the ionospheric TEC at multiple locations (Coster and Komjathy 2008). The early GPS measurements, collected primarily using stand-alone receivers, were compared with ionospheric measurements taken with other instruments, such as Faraday rotation sensors or incoherent scatter radar platforms. Soon GPS itself has become recognized as one of the first remote sensing tools to monitor space weather events (Coster and Komjathy 2008).

In 1989, the first fully operational GPS satellites were launched and it is when a group of scientists affiliated with the International Union of Geodesy and Geophysics initiated the concept of IGS. The IGS was founded in 1992 with a network of about 20 geodetic receivers worldwide which has expanded over time. The development of the IGS network allowed scientific community to begin the research of ionosphere on global basis. In 1998 the ionospheric group of IGS was established (Feltens and Schaer 1998).

There are four Ionosphere Associate Analysis Centers (IAACs): CODE, ESOC (European Space Operations Center of ESA, Darmstadt, Germany), JPL, and UPC (Technical University of Catalonia, Barcelona, Spain). Each of these IAACs are computing global distribution of TEC independently using different models and further on IGS by combining this global TEC information, it can be used for calibration of single-frequency GPS receivers and

altimeters, and investigations of the global temporal and spatial behavior of ionospheric TEC (Coster and Komjathy 2008).

Large amount of GPS (GNSS) receivers distributed all over the globe, not only from IGS network, but also from CORS networks contribute to the day-to-day monitoring of the ionosphere with high precision and also allows to develop empirical models to predict ionospheric response to different space weather phenomena.

The IGS has ensured open access, high-quality GPS (GNSS) data products since 1994 (IGS home page). The products from the IGS CODE are used in the frame of this Doctoral Thesis for data post-processing.

#### 1.1.1.4 IONOSPHERIC EFFECTS ON GNSS SIGNALS

The phase measurements and the code pseudoranges are affected by both, systematic and random errors. One of the systematic errors is ionospheric refraction. The ionosphere is a dispersive medium for microwave signals, which means that the refractive index for GPS signals is frequency-dependent (Dach et al. 2015).

Ionospheric refraction delays the GNSS code measurements and advances the carrier phases. The effect has the same absolute value for code and phase measurements, but with opposite signs (Dach et al. 2015).

On one hand, irregularities in the ionosphere produce short-term signal variations. These scintillation effects may cause a large number of cycle slips because the receiver cannot follow the short-term signal variations and fading periods. Scintillation effects mainly occur in a belt along the Earth's geomagnetic equator and in the polar auroral zone.

On the other hand, a high electron content produces strong horizontal gradients and affects the ambiguity solution using geometrical methods. In GNSS observation data post-processing the only reliable strategy to solve the ambiguities in this case is the Melbourne-Wübbena approach, which is applied in *Bernese GNSS Software v5.2* (Dach et al. 2015) using in addition the P-code measurements. The success of this method very much depends on the quality of the P-code measurements, which is often unsatisfactory under Anti-Spoofing (AS) conditions. Maximum electron content and correspondingly pronounced gradients may be expected for regions close to the (geomagnetic) equator (Dach et al. 2015).

## 1.1.2 SOLAR FLARE

The ionospheric effects due to the solar flare depend on the flare class and the cosine of the great circle angle between the center and flare locations on the solar disc (Liu et al. 2006). The classification of solar flares in this Doctoral Thesis is used to select the data of months included in the analysis, therefore these are described in more detail.

Solar flares are classified as A, B, C, M or X according to the peak flux (in watts per square meter,  $W/m^2$ ) of 1 to 8 Ångströms X-rays near Earth, as measured by X Ray Sensor (XRS) instrument on-board the GOES-15 satellite which is in a geostationary orbit over the Pacific Ocean. Table 1.1 shows the different solar flare classes:

Table 1.1

Solar flare classes

| Class | $W/m^2$ between 1 and 8 Ångströms |
|-------|-----------------------------------|
| A     | $<10^{-7}$                        |
| B     | $\geq 10^{-7} < 10^{-6}$          |
| C     | $\geq 10^{-6} < 10^{-5}$          |
| M     | $\geq 10^{-5} < 10^{-4}$          |
| X     | $\geq 10^{-4}$                    |

Each X-ray class category is divided into a logarithmic scale from 1 to 9. For example: B1 to B9, C1 to C9, etc. An X2 flare is twice as powerful as an X1 flare, and is four times more powerful than an M5 flare. The X-class category is slightly different and it does not stop at X9 but it continues on. Solar flares of X10 or stronger are sometimes also called “Super X-class solar flares.”

Most common are the A-class and B-class solar flares which are regarded as a lowest class of solar flares. The background flux, which is the amount of radiation emitted when there are no flares, is often in the B-range during solar maximum and in the A-range during solar minimum.

The C-class solar flares have little to no effect on Earth, only those which are long in duration might produce a coronal mass ejection but they are usually slow, weak and rarely cause a significant geomagnetic disturbance on Earth. The background flux can be in the lower C-class range when a complex sunspot region inhabits the Earth-facing solar disk.

M-class solar flares are called the medium large solar flares. They cause small (R1) to moderate (R2) radio blackouts on the daylight side of the Earth. Some eruptive M-class solar flares can also cause solar radiation storms. Strong, long duration M-class solar flares can launch a coronal mass ejection. If the solar flare takes place near the center of the Earth-facing

solar disk and launches a coronal mass ejection towards our planet, there is a high probability that the resulting geomagnetic storm is going to be strong enough for aurora to appear on the middle latitudes.

Another factor is the duration of the solar flare. For example, when there is a solar flare with a peak strength of X5 and with a total duration of two hours then it will certainly be accompanied with a bright, large and fast coronal mass ejection. Depending on the location of the eruption, the blast could either miss Earth, be partially or fully Earth-directed. An Earth-directed coronal mass ejection will look like a partial or full-halo coronal mass ejection on the images from the joint NASA-ESA Solar and Heliospheric Observatory mission – SOHO. When this happens the coronal mass ejection will arrive at Earth after 24 hours or more (depending on the speed) and will likely cause a geomagnetic storm with vivid auroral displays (SpaceWeatherLive home page).

X-class solar flares are the biggest and strongest of all the above. On average, solar flares of this magnitude occur about 10 times a year and are more common during solar maximum than solar minimum. Strong to extreme (R3 to R5) radio blackouts occur on the daylight side of the Earth during the solar flare. If the solar flare is eruptive and takes place near the center of the Earth-facing solar disk, it could cause a strong and long lasting solar radiation storm and release a significant coronal mass ejection that can cause severe (G4) to extreme (G5) geomagnetic storming at Earth. There were three severe geomagnetic storms (G4) of the 24th solar cycle that occurred in 2015.

Here below Fig. 1.4 shows C-class, M-class and X-class flares and the respective sunspot numbers during year 2007–2017, which represents the period of analysed data in the frame of Doctoral Thesis.

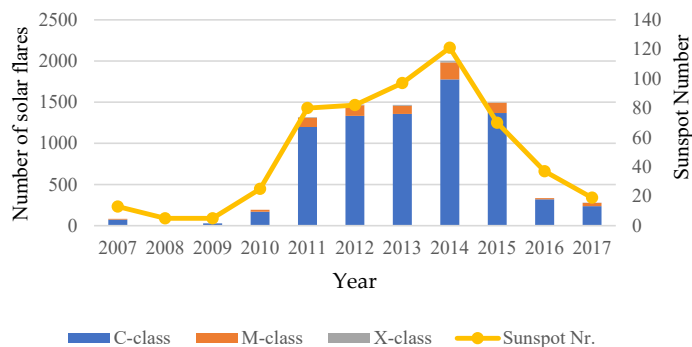


Fig. 1.4. Count of solar flares and count of sunspots, Year 2007–2017; data gathered from (SpaceWeatherLive home page).

### 1.1.3 GEOMAGNETIC STORMS

Magnetic storms occur because of particles from solar flares arriving at the Earth and causing changes in the Earth's magnetic field (Parkinson and Spilker Jr. 1995).

The geomagnetic storm is a major disturbance of the Earth's magnetosphere that occurs when there is a very efficient exchange of energy from the solar wind into the space environment surrounding the Earth. The largest storms are associated with solar coronal mass ejections (CMEs) where a billion tons with its embedded magnetic field, arrives at Earth. Geomagnetic storms create strong horizontal variations in the ionospheric density that can modify the path of radio signals and create errors in the positioning information provided by GNSS (Dobelis, Zvirgzds, and Kaļinka 2017).

Interplanetary magnetic field (IMF) acts as a trigger for magnetic storms. If it is directed southward, in the opposite direction to the Earth's magnetic field, there is reconnection of the IMF and the Earth's magnetic field. The magnetosphere is open and is completely under the influence of the solar wind, that is a flux of particles that regularly escape from the Sun, and that carries with it a part of the solar magnetic field which is called IMF.

Some events such as CMEs, which are huge bubbles of gas threaded with magnetic field lines that are ejected from the Sun over the course of several hours (Alfred Leick 2004; ESA home page), or fast winds associated with coronal solar holes (Coronal holes are large zones less dense and colder than the mean corona. They do not emit in the X-ray domain, which explains the "hole" appearing on X-ray images. Coronal holes correspond to large unipolar regions of the photosphere, allowing a fast solar wind to flow along the open magnetic field lines (Wautelet 2012).) can disrupt the solar wind and create near-earth disturbances called magnetic storms (Amory-Mazaudier et al. 2017).

Geomagnetic storms create large disturbances in the ionosphere. The currents and energy introduced by a geomagnetic storm enhance the ionosphere and the TEC. GPS systems cannot correctly model this dynamic enhancement and errors are introduced into the position calculations. This usually occurs at high latitudes, though major storms can produce large TEC enhancements at mid latitudes as well (NOAA home page).

At high latitudes, the dynamic behavior of the ionosphere is dominated by the solar wind and electron precipitation (aurora borealis and aurora australis). In mid latitudes, ionospheric dynamics are dominated by the inner magnetosphere and neutral winds, the knowledge of which is incomplete (Kintner, Ledvina, and de Paula 2007).

The visible aurora, or "northern lights", are caused by high-energy particles flowing along the Earth's magnetic field lines into the high latitudes, where they interact with the neutral

atmosphere to produce excited ions, giving off red and green displays. These particles also produce additional electrons, and are indirectly responsible for strong electric fields, both of which can produce large electron densities and large shear effects which, in return, produce irregularities. The irregularities cause strong amplitude and phase scintillation fading effects on GPS receivers operating in the auroral and polar cap latitudes.

The strong electric fields generated in the ionosphere during those magnetically disturbed times push electrons over the polar cap, and large, rapid changes in ionospheric group delay can move through a GPS signal ray path, greatly changing the ionospheric range and range-rate errors within time periods of the order of 1 min (Parkinson and Spilker Jr. 1995).

During rare, very strong magnetic storms, these auroral effects can extend well into the midlatitudes, and can cause unusual effects on GPS receivers (Parkinson and Spilker Jr. 1995).

Here below Fig. 1.5 (a) and (b) shows the aurora borealis observed in Latvia on March 17, 2015 when one of the largest geomagnetic storms of the 24th solar cycle occurred.

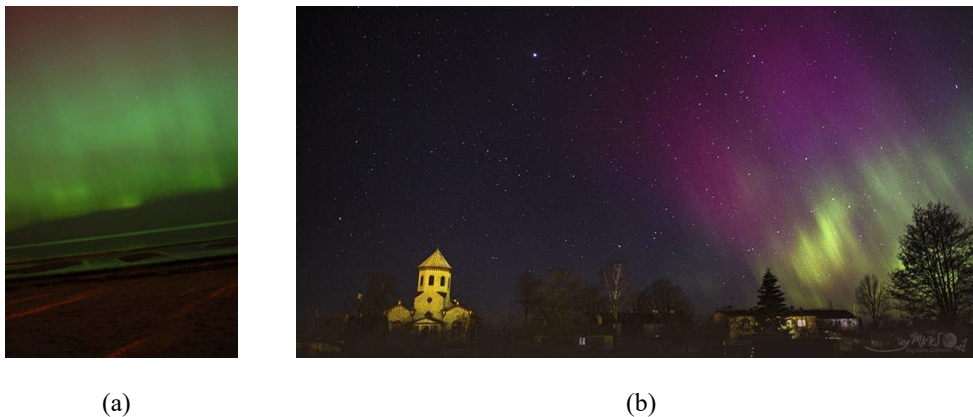


Fig. 1.5 Aurora borealis in (a) Jurmala (Jauns home page), (b) Livani (Jauns home page) observed in Latvia on March 17, 2015.

Figure 1.6 below represents number of days with geomagnetic storm per year, according to the finalized  $Kp$ -index of German Research Centre for Geosciences (Deutsches GeoForschungsZentrum – GFZ) Potsdam in year 2007–2017.

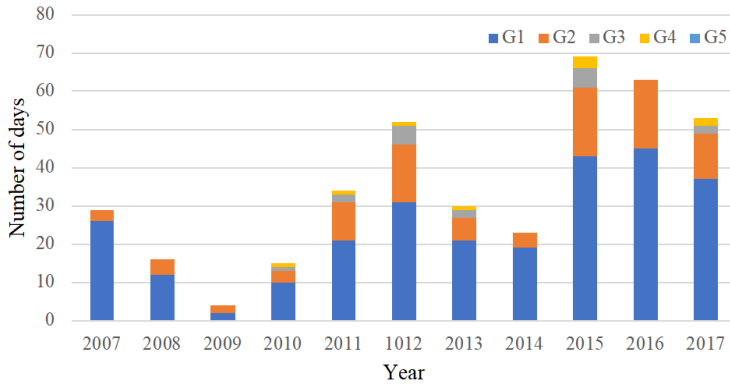


Fig. 1.6. Number of days with geomagnetic storm per year, according to the finalized  $K_p$  – index of GFZ Potsdam (Year 2007–2017); data gathered from: (SpaceWeatherLive home page) (G1 = minor geomagnetic storm; G2 = moderate geomagnetic storm; G3 = strong geomagnetic storm; G4 = severe geomagnetic storm; G5 = extreme geomagnetic storm).

During 2015 three of the most intense geomagnetic storms (Table 1.2) of the solar cycle 24 have occurred, i.e. the storms of March 17 (with a minimum  $Dst$  index value of  $-223$  nT peaking at 23.00 UT, ranked #1 storm in intensity of the present solar cycle), June 23 ( $Dst_{min} = -204$  nT at 05.00 UT, ranked #2), and December 20 ( $Dst_{min} = -155$  nT at 23.00 UT, ranked #3) (Balasis, Papadimitriou, and Boutsis 2019)

The Disturbance storm time ( $Dst$ ) index is a measure of geomagnetic activity used to assess the severity of geomagnetic storms. It is expressed in nanoTeslas (nT) and is based on the average value of the horizontal component of the Earth's magnetic field measured at four near-equatorial geomagnetic observatories. It measures the growth and recovery of the ring current in the Earth's magnetosphere. The lower these values get, the more energy is stored in Earth's magnetosphere (SpaceWeatherLive home page).

Table 1.2

Dst Index in Year 2015

| # | Date       | Dst index (nT) | Geomagnetic storm |
|---|------------|----------------|-------------------|
| 1 | 2015.03.17 | -223           | G4                |
| 2 | 2015.04.11 | -73            |                   |
| 3 | 2015.06.23 | -204           | G4                |
| 4 | 2015.08.16 | -84            |                   |
| 5 | 2015.10.07 | -124           |                   |
| 6 | 2015.12.20 | -155           | G4                |

Space weather events, that occurred in 2015 were widely analysed by the researcher society all over the globe. The impact of the strongest geomagnetic storm on March 17 (St Patrick's Day), 2015 has been widely considered in many publications (Astafyeva,

Zakharenkova, and Förster 2015; Hairston, Coley, and Stoneback 2016; Huang et al. 2016; Kuai et al. 2016; Verkhoglyadova et al. 2016; Zakharenkova, Astafyeva, and Cherniak 2016; Astafyeva et al. 2018).

The findings and obtained results of the impact of the geomagnetic storm, that occurred on March 17, 2015 over the territory of Latvia, on GPS positioning results is discussed further in the Section 3. of the Doctoral Thesis.

### 1.1.3.1 GEOMAGNETIC INDICES

There are numerous indices of magnetic activity. The International Association of Geomagnetism and Aeronomy (IAGA) (IAGA home page) officially recognizes magnetic indices *aa* (*Aa* time resolution: 1 day Universal Time (UT) interval unit: linear scale in unit nT, obtained from daily average of eight *aa* values), *am* (*Am*, *An* and *As* time resolution: 1 day (UT) interval unit: linear scale in unit nT, obtained from daily average of eight *am*, respectively *an* and *as* values), *Kp*, *Dst*, and *AE* (IAGA Working Group V-DAT home page).

The *global Kp index*, referred to as *the planetary index Kp*, that has 3 h time resolution is the mean standardized *K-index* obtained from 13 geomagnetic observatories (NOAA home page) (8 ground based magnetometers around the world (SpaceWeatherLive home page)) located between 44 degrees and 60 degrees northern or southern geomagnetic latitude. The scale is 0 to 9 expressed in thirds of a unit, e.g. 5- is 4 2/3, 5 is 5 and 5+ is 5 1/3, and has 28 values (SpaceWeatherLive home page). This planetary index is designed to measure solar particle radiation by its magnetic effects.

The *ap* index has a time resolution: 3-hour (UT) interval unit: linear scale in unit ~ 2nT, and it is obtained from *Kp* through a conversion table (*Kp2ap*); *Ap* (*Ap* – time resolution: 1 day (UT) interval unit: linear scale in unit ~ 2nT, is obtained from daily average of eight *ap* values) (ISGI home page).

The indices *Ap* and *Kp*, were taken into account when selecting the months for data processing in the frame of the present Doctoral Thesis. Figure 1.7 below shows an example of the *Ap* and *Kp* max indices in year 2015.

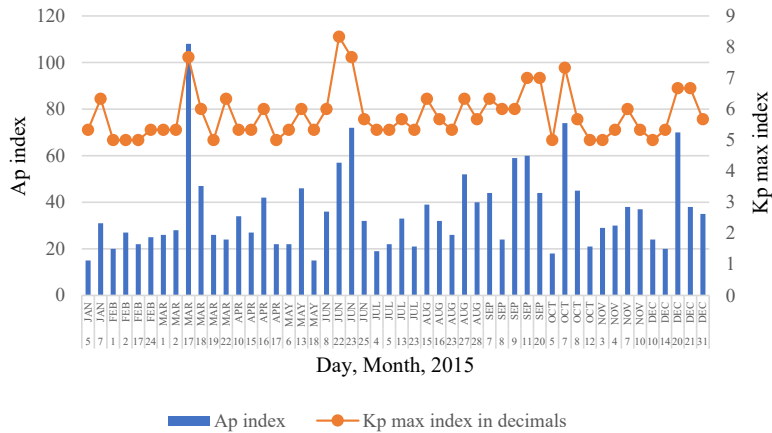


Fig. 1.7. *Ap* and *Kp* max index in Year 2015, data gathered from: (SpaceWeatherLive home page).

Daily regular magnetic field variation arise from current systems caused by regular solar radiation changes. Other irregular current systems produce magnetic field changes caused by the interaction of the solar wind with the magnetosphere, by the magnetosphere itself, by the interactions between the magnetosphere and ionosphere, and by the ionosphere itself.

Magnetic activity indices were designed to describe variation in the geomagnetic field caused by these irregular current systems (NOAA home page).

Geomagnetic indices aim at describing the geomagnetic activity or some of its components. Each geomagnetic index is related to different phenomena occurring in the magnetosphere, ionosphere and deep in the Earth in its own unique way. The location of a measurement, the timing of the measurement and the way the index is calculated all affect the type of phenomenon the index relates to (ISGI home page).

## 1.2 Data sources

Different data acquisition techniques allow to determine various space weather phenomena indices, and thus space weather impact on specific space-based and/or ground based infrastructure, and further to perform the analysis of the data obtained on the basis of either single or combined technique. Worldwide, various methods are studied and applied for the analysis of the obtained data.

Studies of the diurnal, seasonal, and solar cycle behaviour of TEC have been conducted by numerous observers, using various measurement techniques, over more than 30 years (Parkinson and Spilker Jr. 1995).

Ionospheric disturbances, have been observed with ionosondes (providing information about the altitude and maximal concentrations of electrons for different ionospheric layers (regions) (D, E, F1 and F2) allowing, consequently, to estimate a so called ionospheric Total Electron Content (iTEC) without plasmaspheric contribution (Morozova et al. 2019) backscatter radars, airglow imagers or GNSS. Moreover, GNSS receivers are relatively low-cost, compared to other ionospheric probing devices such as ionosondes or radars (Wautelet 2012).

Ground-based GPS TEC and ionograms provide the most abundant data of ionospheric irregularities, which have been extensively used to study the occurrence characteristics of the equatorial F region irregularities (Li et al. 2011).

Recent observational studies of the morphological characteristics and generation mechanisms of ionospheric irregularities, especially ionospheric electrodynamic coupling processes, in the midlatitude region have been conducted using ionosondes, Very High Frequency (VHF) radar, airglow imagers, the GNSS network, the Constellation Observing System for Meteorology, Ionosphere, and Climate (COSMIC) radio occultation (RO) measurements, and Low Earth Orbit (LEO) satellites (Liu et al. 2021).

Multi-instrument observations from magnetometers, GPS-TEC receivers, ionosondes and Swarm satellites over a large geographical extent covering South American, African and European sectors have been studied by Fagundes et al. (2020).

Nowadays, a whole range of tools and instruments are available to examine ionospheric plasma properties – incoherent scatter radars, ionosondes, satellite missions provided with a proper payload including, e.g. the Langmuir probe used to measure the plasma parameters in situ. Nevertheless, one of the most important and widely used is GPS and other GNSS. Despite many limitations of that technique, GNSS are prevalent due to the global coverage, permanent 24 h monitoring time and easy, open access data (via global and regional permanent reference networks, which allow to monitor ionospheric conditions with high precision and to develop empirical models to predict ionospheric response to different external forcing's: solar flares, geomagnetic storms and other events (Kotulak et al. 2021 and Morozova et al. 2020).

In particular, it was shown that at middle latitudes ionospheric conditions (TEC, Traveling Ionospheric Disturbances (TIDs) and scintillation events) respond significantly to strong geomagnetic storms of recent years. These variations can be a reason for the GNSS signal

degradation and a decrease of the precision of the positioning in the affected area (Morozova et al. 2020).

Dual frequency GPS receivers on board the Terra SAR-X satellite, as well as those on two Gravity Recovery and Climate Experiment (GRACE) satellites: GRACE-A and GRACE-B satellites and of the three satellites (A, Alpha; B, Bravo; and C, Charlie) of the ESA's mission Swarm gives the data on VTEC variations (DLR home page).

Dual-frequency satellite radar altimeter Jason-2 flying at a circular orbit at 1336 km altitude, with an inclination, provides data of the VTEC between the water/ocean surface and its orbital altitude (Imel 1994). In addition to the VTEC data beneath the satellite, VTEC can be calculated by using data from the GPS receiver on board the Jason-2 satellite. The latter can be calculated everywhere (including above the continents) along the satellite pass and provides information about changes in the upper topside ionosphere-plasmasphere (above 1336 km) (Astafyeva, Zakharenkova, and Förster 2015).

The ion drift meter (IDM) instrument onboard the Communications/Navigation Outage Forecasting System (C/NOFS) gives data of the ion density  $N_i$  and that of the plasma drifts. C/NOFS satellite was launched in April 2008 and re-entered in November 2015, its primary scientific objective was to study the equatorial ionosphere and, in particular, occurrence of the equatorial plasma bubbles (de La Beaujardière et al. 2009).

Defense Meteorological Satellite Program (DMSP) data provides information about the plasma flows, densities, composition, and temperatures from the polar regions to the equator (Hairston, Coley, and Stoneback 2016).

DMSP is a series of weather satellites operated by the Air Force since the 1960s. All five spacecraft carry the Special Sensor-Ions Electrons Scintillation (SSIIES) thermal plasma instrument package that contain a Retarding Potential Analyzer (RPA), an IDM, a scintillation meter, and a Langmuir probe. The RPA provides the ion flow in the direction of the spacecraft along with the ion temperature, the ion density, and the plasma composition, while the IDM faces into the direction of the spacecraft's velocity to measure the arrival angle of the ions from which it determines the horizontal and vertical cross-track velocities of the plasma. Thus, the full three-dimensional flow vector of the plasma can be determined by combining these results (Hairston, Coley, and Stoneback 2016).

Deep Space Climate Observatory (DSCOVR) satellite provides the real-time solar wind and IMF. DSCOVR measures the parameters of the solar wind and the IMF before it arrives at Earth. This gives us a 15 to 60 minute warning time (depending on the solar wind speed) as to what kind of solar wind structures are on their way to Earth.

Advanced Composition Explorer (ACE) which is another satellite at the Sun-Earth L1 point measures the incoming solar wind. This satellite used to be the primary real-time space weather data source up until July 2016 when DSCOVR become fully operational. The ACE satellite is still collecting data and now operates mostly as a backup to DSCOVR (SpaceWeatherlive home page).

WIND spacecraft (WIND is a spin stabilized spacecraft) gives 1-min resolution IMF  $B_z$  data. WIND observes the unperturbed solar wind that is about to impact the magnetosphere of Earth (NASA home page) and provided by the NASA Goddard Space Flight Center available at (NASA home page).

The ground-based magnetometer measurements provide the data on the horizontal component of Earth's magnetic field.

Multiple studies of ionospheric scintillations have been performed. However, the global climate is evolving, and atmosphere irregularities are changing. The use of GNSS positioning is increasing in various applications and the awareness of space weather impact on GNSS observations is increasing. Recently Sun has started waking up from prolonged solar minimum and several geomagnetic storms experienced on March/April 2022. It is expected that solar activity maximum of 25th solar cycle will occur around 2025.

## **2. METHODOLOGY OF ANALYSIS OF SPACE WEATHER IMPACT ON LATVIAN CORS IN 2007–2017**

### **2.1 Time frame**

Four to 5-month period for each year from 2007 to 2017, was selected. The selected period covers the 24th solar cycle, depicted below in Fig. 2.1 by International Solar Energy Society (ISES) Solar sunspot number progression.

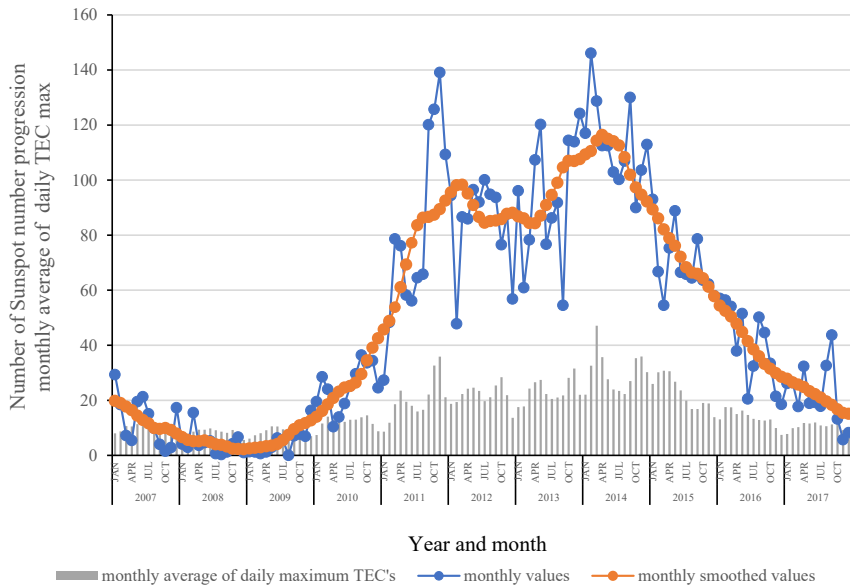


Fig. 2.1. Represents the ISES Solar cycle sunspot number progression and monthly average of daily maximum TEC's (Year 2007–2017) extracted from CODE's ionosphere information *IONEX (IONosphere EXchange format)* data files. Data gathered from: (NOAA home page) and (CODE Data archive).

In general, the sunspot takes place ahead of TEC change by about two days (Guo et al. 2015).

Further on, the description of Latvian CORS stations, the selected GPS observation data, included in the analysis to identify disturbed results caused by space weather phenomena, is given as well as the description of the developed method.

## 2.2 Data

### 2.2.1 LATVIAN CORS NETWORKS AND IGS/EPN STATION RIGA

The research carried out in the frame of this Doctoral Thesis includes the post-processing and analysis of GPS observation data from years 2007 until 2017 of the Latvian CORS networks and the station RIGA00LVA (Directory of MERIT Sites (DOMES) number 12302M002). The station RIGA00LVA is operational since December 5, 1995. It is part of the IGS with its assigned acronym RIGA, and since November 3, 1996 the station RIGA00LVA has been integrated in the EPN (Salmins et al. 2022; EUREF home page; SONEL home page). Hereafter, the station RIGA00LVA will be denoted as IGS/EPN station RIGA.

There are two CORS networks in Latvia, namely – LatPos and *EUPOS*<sup>®</sup>-Riga.

As mentioned above in the *Introduction* section, CORS stations of both networks, are operational since year 2007 (some stations since 2006).

LatPos network GNSS stations cover all the territory of Latvia and are maintained by the Latvian Geospatial Agency (LGIA). The GNSS stations of the *EUPOS*<sup>®</sup>-Riga network as well as the IGS/EPN station RIGA are located in Riga city. The first of these are maintained by the Riga Municipality and the IGS/EPN station RIGA – by the Institute of Astronomy, University of Latvia.

Below, Fig. 2.2 represents the schematic map of the LatPos and the *EUPOS*<sup>®</sup>-Riga network GNSS station locations, as well as the location of the IGS/EPN station RIGA, from years 2007 until 2017.

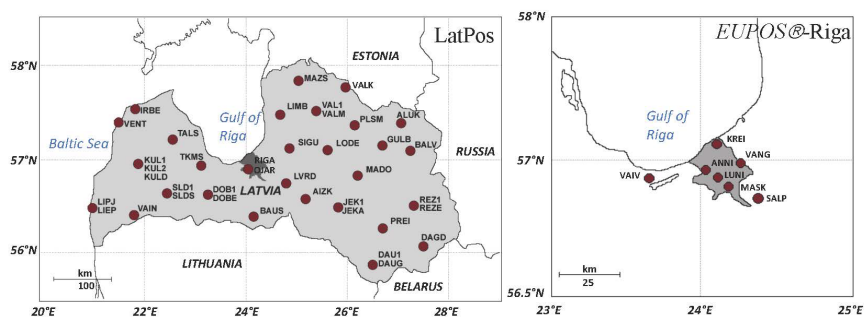


Fig. 2.2. A schematic map of LatPos and *EUPOS*<sup>®</sup>-Riga networks and IGS/EPN station RIGA.

At the beginning of 2007, only 23 CORS stations were operational, new stations were gradually created, and in year 2017, the number of operational stations reached 32. Many stations during the 11-year period were moved to other locations. Therefore, it is more truthful to refer to 46 sites instead of 46 stations.

For example, in the city of Kuldīga, the LatPos network CORS station with a name KULD (although, according to IGS conventions the station name is composed from the entries of the keywords MARKER NAME and MARKER NUMBER: the first four characters of the MARKER NAME (assuming the four character station identifier) and the first nine characters of the MARKER NUMBER (assuming a DOMES code) are concatenated names of the form, e.g. “KULD 10708M001” (Bernese GNSS Software home page), in this Doctoral Thesis station name and MARKER NAME are used with the same meaning) was moved to another location two times, correspondingly changing the station name to KUL1 after the first move and to KUL2 after the second move, thus, different station names are represented in Figure 2.2.

The *EUPOS*<sup>®</sup>-Riga network consists of 5 stations (Fig. 2.2), with their respective names, initially: ANNI, KREI, LUNI, MASK and VANG. Stations MASK and ANNI were operational from 2007–2011, then they were moved to other locations, given new station names – SALP and VAIV respectively, and from mid-2011 up until now are operational.

Amongst all the stations, included in the GPS observation data post-processing and analysis in the present Doctoral Thesis, only 9 stations were not moved for 46 months (Fig. 2.3).

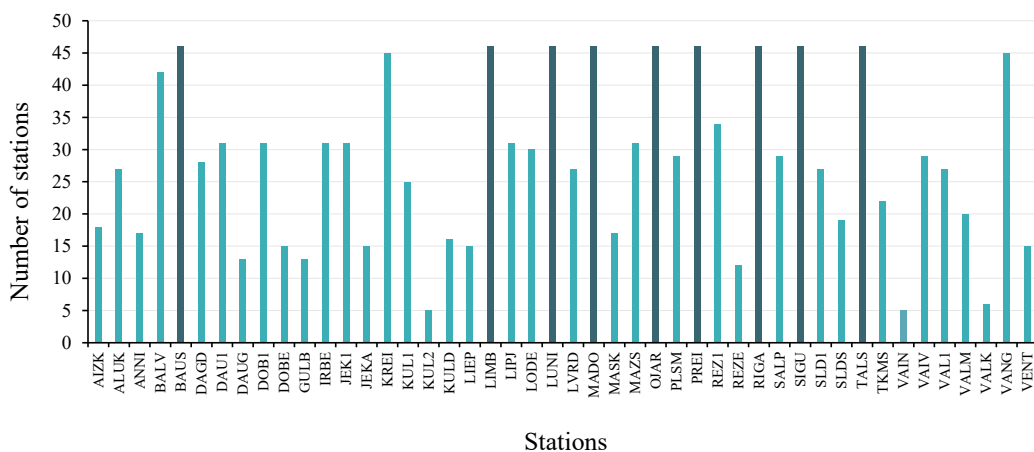


Fig. 2.3. Data input rate (months) of Latvian CORS stations.

### 2.2.2 DATA SELECTION

Daily GPS Receiver INdependent EXchange format (RINEX) observation data (30-second sampling rate) for the full set of the Latvian CORS stations for selected 4 to 5-month period for each year from 2007 to 2017 was collected, taking into account the following indices:

- the maximum TEC values, represented in Figure 2.1, which were extracted from the CODE's IONEX format data files (CODE Data archive);
- information on significant events of space weather phenomena, i.e. data on magnitude (solar flare classes) and number of solar flares, and on geomagnetic storm indices  $Kp$  and  $Ap$ , was obtained from auroral and solar activity web page (SpaceWeatherLive home page).

As a result, total number of months included in the analysis reached 46. The 5-month GPS RINEX 30-second observation data for year 2015 (month of March – St. Patrick's day

geomagnetic storm) and for year 2017 (month of October – due to increased solar activity) has been selected, in comparison with the 4-month observation data in each of all the other 9 years.

Table 2.1

Selected Months for Data Processing

| Year  | 2007 | 2008 | 2009 | 2010 | 2011 | 2012 | 2013 | 2014 | 2015 | 2016 | 2017 |
|-------|------|------|------|------|------|------|------|------|------|------|------|
| Month | FEB  | MAR  | JUL  | JAN  | MAR  | JAN  | MAY  | FEB  | MAR  | FEB  | APR  |
|       | JUN  | JUN  | AUG  | FEB  | AUG  | MAR  | OCT  | JUN  | MAY  | APR  | MAY  |
|       | SEP  | SEP  | OCT  | APR  | SEP  | JUL  | NOV  | OCT  | JUNE | MAY  | JUL  |
|       | OCT  | OCT  | DEC  | MAY  | NOV  | OCT  | DEC  | DEC  | OCT  | JUL  | SEP  |
|       | –    | –    | –    | –    | –    | –    | –    | –    | DEC  | –    | OCT  |

## 2.3 The developed method

The developed method for the data post-processing and analysis, and further on the characterization of space weather impact on GPS observations in Latvia, i.e. on the Latvian CORS stations, is based on a statistical approach.

Statistical approach is used worldwide when analyzing large amount of data (Hlubek et al. 2014).

In the frame of the Doctoral Thesis, the developed method for the analysis of coordinates as such is implemented for the first time.

### 2.3.1 DATA PROCESSING

For the post-processing of the selected data set, the *Bernese GNSS Software v5.2* was used, and for the analysis of the post-processed data, the flowchart of the processing functions and related data sets was created and further on implemented in the development of software programs in Fortran g95 and Python programming languages at LU GGI.

The applied *Bernese GNSS Software v5.2* and software programs in Fortran g95 and Python programming language, developed for the analysis of a large amount of computed results is discussed in the Section 2.3.1.1 and in the Section 2.3.2, respectively.

### 2.3.1.1 PRIMARY PROCESSING OF CORS OBSERVATION DATA APPLYING BERNESE GNSS SOFTWARE V5.2

In order to identify disturbed results caused by significant events of space weather phenomena, the Latvian CORS 11-year, selective daily GPS observation data was post-processed using *Bernese GNSS Software v5.2* (Dach et al. 2015).

*Bernese GNSS Software* is a scientific, high-precision, multi-GNSS data processing software developed at the Astronomical Institute of the University of Bern (AIUB). It is, e.g. used by CODE for its international (IGS) and European (EUREF – Regional Reference Frame Sub-Commission for Europe)/EPN activities. The software is in a permanent process of development and improvement (Bernese GNSS Software home page). It consists of multiple sub-programs with wide possibilities. Mainly it is used for estimation of static daily GNSS coordinate solutions, though it also allows the estimation of kinematic GNSS receiver coordinates in the zero-difference and precise point positioning mode. In the GNSS observable analysis, kinematic positions allows to track sub-daily movement of a static station, for example, changes in antenna position due to an earthquake (Dach et al. 2015). The *Bernese GNSS Software v5.2* is used in most of European countries for the post-processing of most precise GNSS observations (Balodis et al. 2017).

The relevant data post-processing strategy parameters (Table 2.2) were set up within *Bernese GNSS Software v5.2* in order to compute the Latvian CORS stations Cartesian  $X, Y, Z, T$  coordinates of the selected GPS RINEX 30-second observation data.

Table 2.2

List of the Main Data Post-processing Strategy Parameters

| Parameter  | Value   |
|--|---|
| Processing strategy  | Double-difference mode (kinematic double-difference network solution), ionosphere-free linear combination (LC); MAURPP  |
| Ground and satellite antenna phase center calibrations             | Absolute, IGS   |
| CODE products used   | Precise orbits, Earth orientation, clock, final ionosphere, CODE data – available at: <a href="http://ftp.aiub.unibe.ch/CODE/">http://ftp.aiub.unibe.ch/CODE/</a> |
| 4 IGS/EPN network reference stations for each solution computation | LAMA (Olsztyn, Poland), METS (Metsahovi, Finland), VIS0 (Visby, Sweden), VLNS (Vilnius, Lithuania)  |
| Satellite system   | GPS   |
| Elevation cut-off elevation angle                                  | 15° (satellite observations below 15° are excluded)   |

|   |   |
|---|---|
| Sampling interval                               | 90-s sampling interval of kinematic post-processing was chosen  |
| Ocean tidal loading corrections                 | FES2004 ocean tidal model was used, provided online by H.-G. Scherneck (available at: (Free ocean tide loading provider home page)) |
| Corrections of solid Earth tide effect          | Yes   |
| Tropospheric delay modelling                    | Dry Global Mapping Function (DRY_GMF)   |
| Minimum size of accepted cycle slip corrections | 10  |

Hereafter the processing strategy with *Bernese GNSS Software v5.2* programs is described in more detail.

*Bernese GNSS Software v5.2* program RNXSMT (detects cycle slips and outliers on RINEX level using simultaneous code and phase observations from both frequencies to each satellite; code observations are smoothed using the phase measurements) and MAUPRP (Automatic phase pre-processing, cycle slip detection and correction, outlier detection, an update of the Ambiguity List) were used for cycle slip detection (Dach et al. 2015). The MAUPRP program is also used to repair cycle slips, with 10 cycles being the minimum size of accepted cycle slip corrections. The outputs from both programs were used to find detected cycle slips for each station and baseline.

For the *Bernese GNSS Software v.5.2* solutions, 4 IGS/EPN network stations were used as reference stations (selection of reference station data from the EUREF data base (EUREF home page), and the Latvian CORS stations were used as rover stations. The CODE's precise orbit and clock data, final ionosphere products, ocean tidal loading corrections were taken into account. The dry Global Mapping Function (*DRY\_GMF*) was used to model the tropospheric delay.

Ionosphere-free Linear Combination (LC)  $L_3$  of dual-band measurements was used. This LC, which nearly completely eliminates the ionospheric refraction effects, is recommended to be used for most networks (Dach et al. 2015).

For space weather impact analysis the 90-second (90-s) sampling interval for kinematic post-processing was chosen, i.e. the International Terrestrial Reference Frame (ITRF) coordinates were determined for each Latvian CORS station for each 90-s session. The set  $S$  of 90-s kinematic solutions for  $n$  stations with subsets of coordinates for each station are denoted by  $s_i$ , correspondingly:

$$S = \{s_1, s_2, \dots, s_n\}, \quad (2.1)$$

where

$$s_i = \{X_i, Y_i, H_i, T_i\}, i = 1, 2, \dots, n. \quad (2.2)$$

The computation of coordinates was performed for each of the above-mentioned sessions by applying the *Bernese GNSS Software v5.2*. The solutions were carried out in sets of 4–5 Latvian CORS stations and constantly using the same IGS/EPN network reference stations. The results were converted from Cartesian coordinates  $X, Y, Z, T$  to plane coordinates  $x, y, h$  (Northing ( $N$ ), Easting ( $E$ ), Up ( $h$ )), where  $h$  means ellipsoidal height for each 90-s kinematic solution. The set  $P$  of 90-s kinematic solution results for each month with  $m$  days for  $n$  stations was obtained with subsets  $p_{ijk}$  of coordinates:

$$P = \{p_{ij1}, p_{ij2}, \dots, p_{ijk}\}, i = 1, 2, \dots, n; j = 1, 2, \dots, m; k = 1, 2, \dots, 28800, \quad (2.3)$$

where

$$p_{ijk} = \{x_{ijk}, y_{ijk}, h_{ijk}, t_{ijk}\}. \quad (2.4)$$

In formula (2.3) for a period of 30 days, 960 times of 90-s kinematic post-processing solutions per day forms 28800 kinematic solutions for each station, i.e. 864,000 kinematic solutions per month for 23–32 CORS stations (the number of stations changes over the years). The epoch  $t_{ijk}$  is an epoch for each kinematic solution.

The computation of the Cartesian coordinates  $X, Y, Z, T$  of each set of 4–5 Latvian CORS stations (for an observation period of 1 month takes approximately 12–14 hours) was carried out for all the Latvian CORS stations for 4 to 5 months per year, for 11 years (2007–2017). The large amount of data and the resources did restrict to perform the analysis of all months.

### 2.3.2 FLOWCHART OF ANALYSIS PROCESSING FUNCTIONS AND RELATED DATA SETS

As mentioned above, after the data post-processing with *Bernese GNSS Software v5.2*, the post-processed observation data was analysed by applying software programs developed at the LU GGI.

As a result, the monthly disturbed results (further denoted as faulty solutions, where one of the coordinate components exceeds the 10 cm threshold) were found and the statistical analysis was performed, the data was prepared for the correlation analysis and the correlation analysis was performed.

The main functions performed:

- a) the Cartesian  $X, Y, Z, T$  coordinates were computed for each Latvian CORS station, each day, each 90-s using *Bernese GNSS Software v5.2*;
- b) each solutions' Cartesian  $X, Y, Z, T$  coordinates were converted to the national grid coordinates: Northing, Easting, Up (abbreviation denoted in Figure 2.4 – NEht) (SW1);
- c) the cycle slips identified by the *Bernese GNSS Software v5.2* were listed (CSLP);

In order to extract the cycle slip information from the *Bernese GNSS Software v5.2* program MAURPP output files (SMT\*.OUT), and concatenate the cycle slip files, 2 programs in Python programming language were created LU GGI (Table 2.3 below).

In extracted information cycle slips were characterized by the station name, date and time of the cycle slip occurrence. Due to the fact that time of cycle slips occurrence in MAURPP output files is defined as float number, it was converted to hh:mm:ss format.

Table 2.3

List of Programs in Python Programming Language

| # | Name             | Task  | Input                  | Output               |
|---|------------------|---|------------------------|----------------------|
| 1 | SMT_cycle_slips  | Selection of cycle slip information from Bernese SMT*.OUT files | Bernese SMT*.OUT files | Cycle_slips.txt      |
| 2 | Read_cycle_slips | Concatenation of cycle slip files                               | Cycle_slips.txt        | C_SLIPS from Bernese |

- d) the monthly sets of faulty solutions for each station where one of the coordinate components exceeded 10 cm were formed (SW2, ALL\_ERR);
- e) the monthly mean coordinate values were calculated (SW2, MONTH TREND) for each station in each month (ALL\_ERR, X4);
- f) The geomagnetic storms over the territory of Latvia, the TEC max values, and solar flares were extracted from the publicly available data sources (CODE Data archive), (SpaceWeatherLive home page) (For\_CORR);
- g) the analysis of the occurrence of faulty solutions and the sequences of faulty solutions forming Loss-of-Lock situations was performed (SW3\_LOCK);
- h) simultaneously occurred faulty solutions in several stations forming “evil waves” (SW3);

- i) monthly lists of coordinate discrepancies of faulty solutions occurred simultaneously for each corresponding epoch were formed (SW3, 1\_Z4, Table\_S18, Table\_S19, Table\_S20);
- j) count of faulty solutions, cycle slips and cycle slips within faulty solutions for each month for each station were performed by adding information on extreme solar events and max TEC values over Latvia (For\_COR);
- k) covariance and regression lines were computed on TEC and faulty solutions for each month for each station (R\_Line);
- l) the Pearson's correlation coefficients were computed to find the relation between TEC (monthly set  $x$ ) and count of cycle slips (monthly set  $y$ ), similarly, between TEC and the count of faulty solutions, as well as TEC and the count of cycle slips in faulty solutions, and also between the count of the cycle slips and the count of faulty solutions (Correlation, R\_line). (Correlation procedure and Correlation Dbase);

Hereafter the Flowchart of the processing functions and data sets is depicted.

 Process. Indicates any processing function.

 Indicates data that displayed as result or will be used for next processing function.

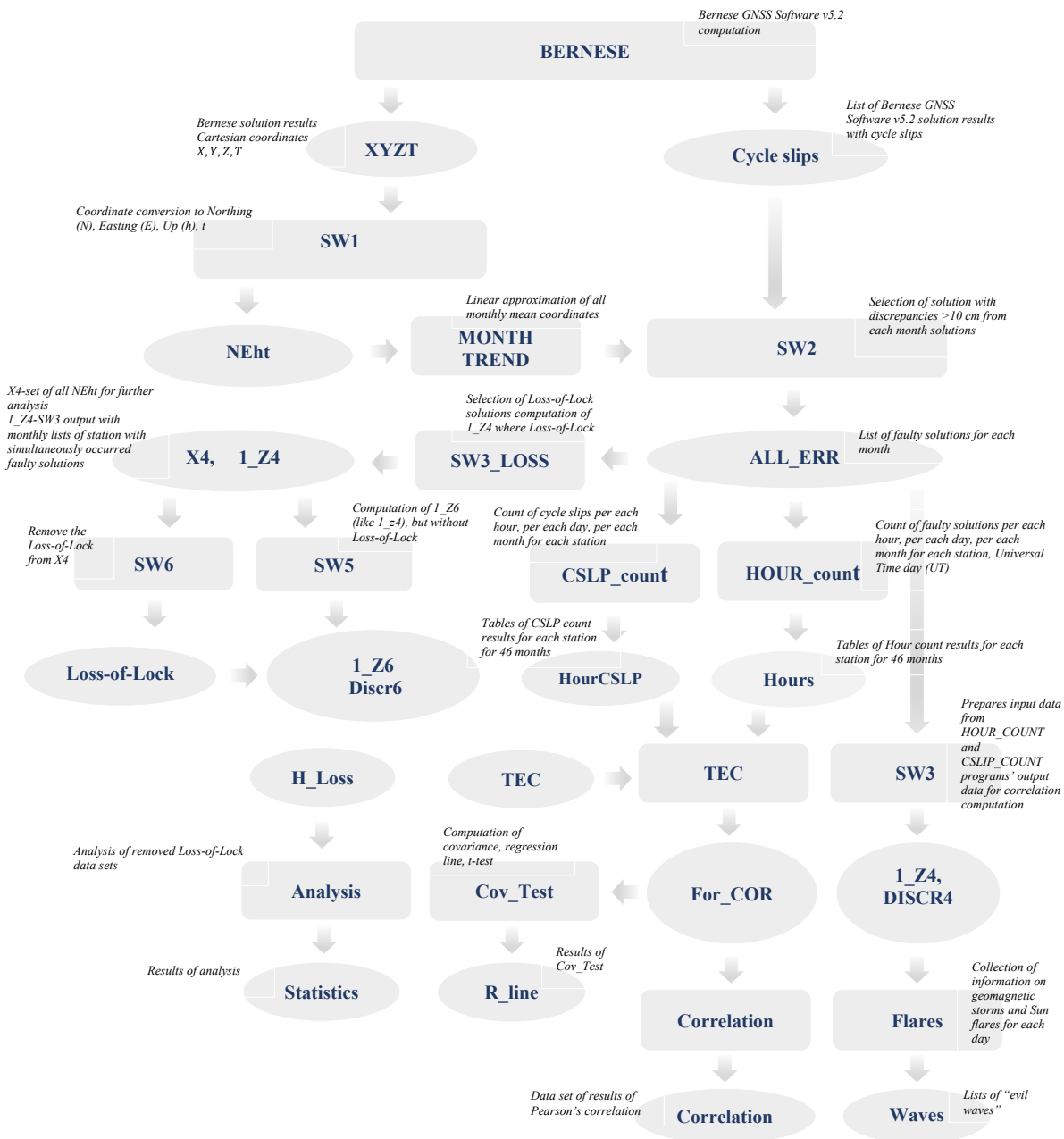


Fig. 2.4. Flowchart of the processing functions and related data sets.

### 3. RESULTS

#### 3.1 Monthly mean station coordinates

As mentioned above, the post-processed observation data was analysed according to the analysis described in Figure 2.4. The Cartesian  $X, Y, Z, T$  coordinates are converted to the national grid coordinates: Northing, Easting, Up (abbreviation denoted in Figure 2.4 –  $NEht$ ). The first task is to evaluate the  $NEht$  results and to discover either there are some disturbed results.

The knowledge on the correct monthly mean station, non-disturbed, coordinate values is the prerequisite to identify disturbances. The values of the monthly mean coordinates were changing during the period of 11 years. In order to calculate the reliable monthly mean coordinates, in the first attempt, the outliers exceeding  $3\sigma$ , i.e. 10 cm, criteria were excluded.

The trend of mean coordinate values after the data filtration from the first attempt was nearly linear. The time series were evaluated in the second attempt (example in Figure 3.1). The adjustment of monthly average was performed for each station component ( $XYH$ ) by solving the trend equation

$$x = at + b \quad (3.1),$$

where  $t$  is expressed in years and decimals of the 15th date of month. The adjusted monthly coordinate values for each station were used to identify the disturbed solutions which differ from adjusted monthly average more than  $3\sigma$ , i.e. 10 cm (Data set ALL\_ERR).

The quality control of the monthly mean coordinates for the set of filtered solution results becomes possible.

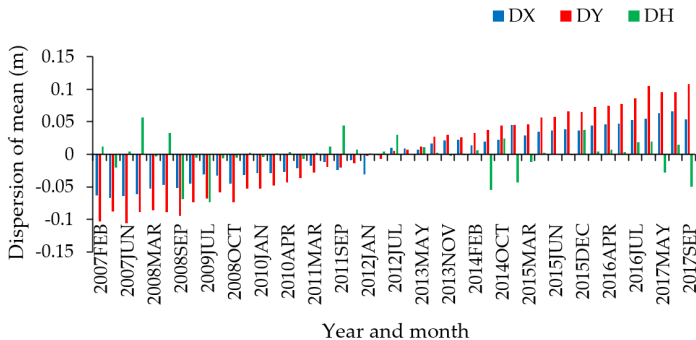


Fig. 3.1. Differences of station RIGA monthly mean coordinate components.

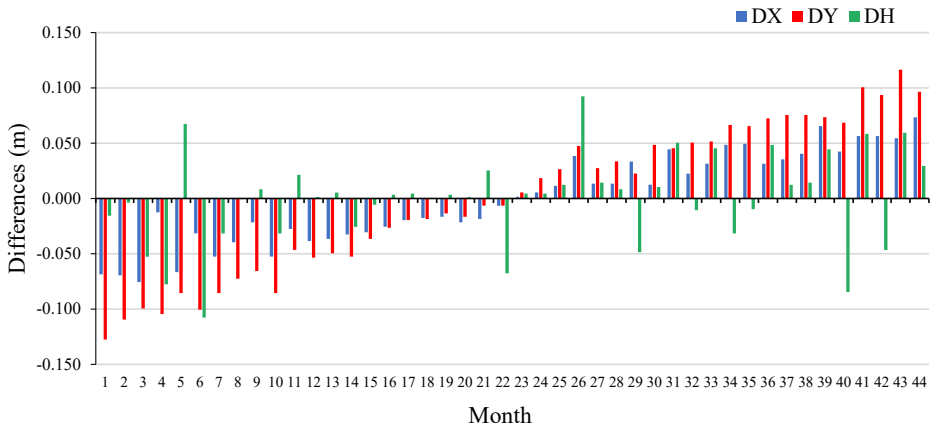


Fig. 3.2. Monthly average differences (m) of station LIMB.

The monthly mean coordinates obtained were used to identify the disturbed solutions among the whole set of *Bernese GNSS Software v5.2* solutions. The accuracy of each solution was controlled by checking the discrepancies of each of the component (Northing, Easting, Up) of the national grid in comparison with monthly mean coordinate values.

The precision of filtered solution results of monthly mean station coordinates is about 3 cm.

### 3.2 Distribution of the size of discrepancies

During the research, the total count of *Bernese GNSS Software v5.2* solutions reached 36,728,129 from which 203,981 (i.e. 0.6 %) solutions appeared with discrepancies in position greater than 10 cm ( $3\sigma$ ). Including the 10 cm threshold, the count reached 204,022. There were 744,689 cycle slips (CSLP) identified by *Bernese GNSS Software v5.2*. This covers 2 % of all *Bernese GNSS Software v5.2* solutions. In the subset of faulty solutions, just 4849 cycle slips (i.e. 0.6 % of all cycle slips) of these were identified by *Bernese GNSS software v5.2*. The size of the discrepancies in coordinates is classified in Table 3.1.

Table 3.1

Distribution of the Size of Discrepancies

| #     | Interval (m)  | Count of faulty solutions | CSLP % f. sol. | % CSLP  |
|-------|---------------|---------------------------|----------------|---------|
| 1     | [0.1 1.0)     | 153592                    | 3781 75.3 %    | 78.0 %  |
| 2     | [1.0 5.0)     | 21533                     | 473 10.6 %     | 9.8 %   |
| 3     | [5.0 10.0)    | 8691                      | 192 4.3 %      | 4.0 %   |
| 4     | [10.0 20.0)   | 7163                      | 141 3.5 %      | 2.9 %   |
| 5     | [20.0 30.0)   | 4196                      | 57 2.1 %       | 1.2 %   |
| 6     | [30.0 40.0)   | 2694                      | 42 1.3 %       | 0.9 %   |
| 7     | [40.0 50.0)   | 1478                      | 33 0.7 %       | 0.7 %   |
| 8     | [50.0 100.0)  | 3401                      | 87 1.7 %       | 1.8 %   |
| 9     | [100.0 150.0) | 806                       | 26 0.4 %       | 0.5 %   |
| 10    | [150.0 200.0) | 259                       | 10 0.1 %       | 0.2 %   |
| 11    | [200.0 500.0) | 204                       | 7 0.1 %        | 0.1 %   |
| 12    | [500.0 900.0] | 5                         | 0 0.0 %        | 0.0 %   |
| Total | [0.1 900.0]   | 204022                    | 4849 100.0 %   | 100.0 % |

During the geomagnetic storm, which occurred on March 17, 2015 (St. Patrick's day), max discrepancies in 2 CORS stations (RIGA and VAIV) reached 500 m. The discrepancies caused by ionospheric disturbances in 50430 solutions is greater than 1 meter (Table 3.1). This is dangerous in Safety-of-Life critical situations.

75 % of discrepancies were in the bounds of [0.1; 1.0) meters; 10 % of discrepancies were in the bounds of [1.0; 5.0) and 4 % of discrepancies were in the bounds of [5.0; 10). 10 % of discrepancies were greater than 10 meters. From 204,022 faulty solutions there were 2.4 % cycle slips identified by *Bernese GNSS Software v5.2*. Unfortunately, in these cases, the results were not excluded by *Bernese GNSS Software v5.2*.

### 3.3 “Evil wave” of disturbances

The term “evil waveform” is used to denote the disturbed information for navigation in some area caused by the GPS clock error (Julien et al. 2017). The term “evil wave” in the present Doctoral Thesis is used to describe the changing distribution of positioning discrepancies over the territory of Latvia in some time period. The movement of “evil wave” is shown in Fig. 3.4 (a), (b), and (c) and supplementary file Tables S2–S7. The red circles in Fig. 3.4. denote the simultaneously occurring faulty solutions. In each of the (a), (b), and (c) titles in the top row, the period of the “evil wave” is written, in the second row – the beginning of the current 90-s faulty solution is shown.

When sorting the faulty solutions, the occurrence of faulty solutions was found in numerous stations simultaneously. The movement of these faulty solutions over the territory of

Latvia can be described as a “waveform”. This could be interpreted as ionospheric disturbances, exposed in a form of table (Table 3.2, supplementary file Table S4 and Table S7) and/or graphs (Fig. 3.3 and Fig. 3.4).

Table 3.2

Sample List of CORS Stations, Date and Time of Simultaneous Scintillations

| #   | Date        | Time       | CORS station name   |
|-----|-------------|------------|---|
| 785 | 2012 OCT 28 | 8:16:30 UT | BAUS DOB1   |
| 786 | 2012 OCT 28 | 9:45: 0 UT | DAU1  |
| 787 | 2012 OCT 28 | 9:58:29 UT | LUNI  |
| 788 | 2012 OCT 29 | 0: 0: 0 UT | SIGU REZ1 TALS SLD1 VANG IRBE VAL1 RIGA OJAR MADO PREI LIMB ALUK<br>DOB1 DAU1 DAGD BAUS BALV MAZS LIPJ KULI PLSM JEK1 |
| 789 | 2012 OCT 29 | 0:55:30 UT | JEK1 MAZS BALV PLSM DAGD  |
| 790 | 2012 OCT 29 | 0:57: 0 UT | VAL1 DAGD RIGA VANG IRBE DOB1 DAU1 BAUS ALUK PREI OJAR LIMB<br>MADO SLD1 SIGU TALS REZ1 LVRD                          |
| 791 | 2012 OCT 29 | 0:58:30 UT | SLD1 PREI LIMB MADO DAGD MAZS BALV DOB1 DAU1 BAUS LVRD ALUK   |
| 792 | 2012 OCT 29 | 1: 0: 0 UT | LIPJ SIGU SLD1 IRBE RIGA TALS VANG REZ1 PREI OJAR LIMB MADO   |
| 793 | 2012 OCT 29 | 1: 1:30 UT | ALUK OJAR   |
| 794 | 2012 OCT 29 | 1: 3: 0 UT | REZ1  |
| 795 | 2012 OCT 29 | 1: 6: 0 UT | LIPJ OJAR RIGA  |
| 796 | 2012 OCT 29 | 7:33: 0 UT | LIPJ  |

Table 3.2 (and the supplementary file Table S4 and Table S7) lists the names of the CORS stations, where the faulty solutions occurred simultaneously, the date and time are fixed. Similar information was obtained for all the selected months in a period of 11 years.

The “evil waves” were counted in cases where the groups of at least three simultaneous 90-s sequences occurred within at least two simultaneous solutions with equal time events. Table 3.2 shows example of 2 “evil waves”: the first on Oct 29, 2012, 0:0:0 UT and the second, starting at 0:55:30 UT Oct 29, 2012 and ending at 1:1:30 UT, Oct 29, 2012. According to the Fig. 3.5, there are 28 “evil waves” in December 2009.

Figure 3.3 depicts similar information for the entire month of December 2009, and represents, eventually, the space weather impact on GPS observations on the whole set of CORS stations. Figure 3.3 does not represent the names of the CORS stations where the simultaneous faulty solutions occurred. The sample of the size of disturbances on 27, 28, and 29 December, 2009 is shown in the supplementary file Table S8. The month of December 2009 is at the beginning part of the solar cycle 24 when the Sun activity awakes after a long, calm period.

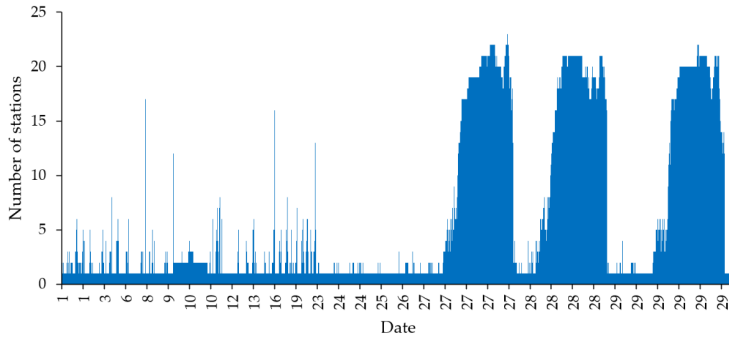


Fig. 3.3. Plot of the distribution of simultaneously occurred faulty solutions in December 2009.

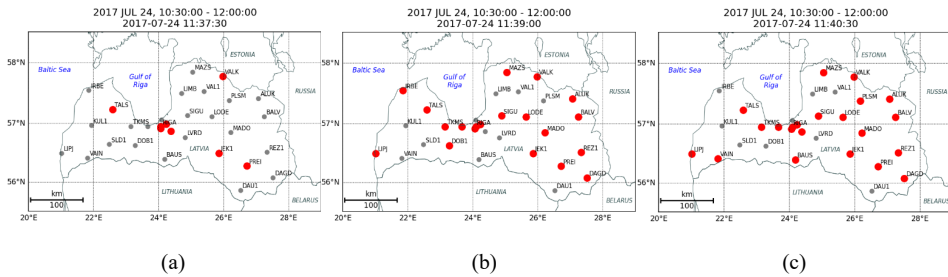


Fig. 3.4. Movement of “evil wave” over the territory of Latvia on July 24, 2017.

The movement of one “evil wave” (Fig. 3.4) is described as an example: there are only 8 CORS stations with faulty solutions (red dots) in Fig. 3.4 (a). In Figure 3.4 (b), there are already 20 CORS stations with faulty solutions; RIGA and SALP now have a good solution and there are 14 new CORS stations with faulty solutions (compared to Fig. 3.4 (a)). In Figure 3.4 (c), there are 21 CORS stations. DOB1, VANG, IRBE, and ALUK now have a good solution and new CORS stations with faulty solutions are VAIN, KUL2, BAUS, LVRD, and PLSM (compared to Fig. 3.4 (b)). The “evil wave” continues (it is not shown in Fig. 3.4), and the end time of the disturbed position’s “evil wave” on July 24, 2017 is at 11:46:30 UT.

Table 3.3 (supplementary file Table S3) summarizes the “evil waves” over the territory of Latvia in December 2014. It is better understandable by looking at the distribution of “evil waves” depicted in the supplementary file Table S4.

Table 3.3

## List of “Evil Waves”

March 2015

December 2014

(see supplementary file Table S6)

(see supplementary file Table S3)

No.- Number of first record of wave;  
S -count of sequential records of wave.

No.- Number of first record of wave;  
S -count of sequential records of wave.

| #       | No.  | S   |
|---------|------|-----|
| 1 WAVE  | 26   | 15  |
| 2 WAVE  | 77   | 23  |
| 3 WAVE  | 135  | 22  |
| 4 WAVE  | 159  | 11  |
| 5 WAVE  | 201  | 21  |
| 6 WAVE  | 256  | 17  |
| 7 WAVE  | 297  | 16  |
| 8 WAVE  | 314  | 1   |
| 9 WAVE  | 344  | 15  |
| 10 WAVE | 380  | 14  |
| 11 WAVE | 414  | 13  |
| 12 WAVE | 451  | 16  |
| 13 WAVE | 495  | 11  |
| 14 WAVE | 551  | 14  |
| 15 WAVE | 572  | 5   |
| 16 WAVE | 609  | 18  |
| 17 WAVE | 685  | 11  |
| 18 WAVE | 697  | 1   |
| 19 WAVE | 726  | 15  |
| 20 WAVE | 812  | 16  |
| 21 WAVE | 865  | 149 |
| 22 WAVE | 1025 | 36  |
| 23 WAVE | 1065 | 8   |
| 24 WAVE | 1078 | 18  |
| 25 WAVE | 1098 | 18  |
| 26 WAVE | 1131 | 21  |
| 27 WAVE | 1182 | 17  |
| 28 WAVE | 1225 | 15  |
| 29 WAVE | 1267 | 11  |
| 30 WAVE | 1304 | 11  |
| 31 WAVE | 1329 | 12  |
| 32 WAVE | 1355 | 15  |
| 33 WAVE | 1375 | 2   |
| 34 WAVE | 1379 | 11  |
| 35 WAVE | 1391 | 3   |
| 36 WAVE | 1407 | 13  |
| 37 WAVE | 1443 | 14  |
| 38 WAVE | 1471 | 14  |
| 39 WAVE | 1486 | 1   |
| 40 WAVE | 1503 | 15  |
| 41 WAVE | 1531 | 17  |

| #       | No.  | S  |
|---------|------|----|
| 1 WAVE  | 4    | 15 |
| 2 WAVE  | 73   | 16 |
| 3 WAVE  | 112  | 15 |
| 4 WAVE  | 163  | 7  |
| 5 WAVE  | 178  | 2  |
| 6 WAVE  | 184  | 18 |
| 7 WAVE  | 238  | 17 |
| 8 WAVE  | 270  | 15 |
| 9 WAVE  | 299  | 17 |
| 10 WAVE | 329  | 15 |
| 11 WAVE | 370  | 15 |
| 12 WAVE | 399  | 15 |
| 13 WAVE | 435  | 17 |
| 14 WAVE | 473  | 9  |
| 15 WAVE | 489  | 16 |
| 16 WAVE | 531  | 1  |
| 17 WAVE | 594  | 15 |
| 18 WAVE | 627  | 17 |
| 19 WAVE | 653  | 15 |
| 20 WAVE | 704  | 15 |
| 21 WAVE | 739  | 15 |
| 22 WAVE | 778  | 15 |
| 23 WAVE | 814  | 16 |
| 24 WAVE | 886  | 4  |
| 25 WAVE | 892  | 17 |
| 26 WAVE | 1067 | 14 |
| 27 WAVE | 1088 | 40 |
| 28 WAVE | 1197 | 1  |
| 29 WAVE | 1259 | 16 |
| 30 WAVE | 1288 | 1  |
| 31 WAVE | 1334 | 17 |
| 32 WAVE | 1420 | 17 |
| 33 WAVE | 1475 | 5  |
| 34 WAVE | 1509 | 17 |
| 35 WAVE | 1548 | 16 |
| 36 WAVE | 1567 | 4  |
| 37 WAVE | 1598 | 16 |
| 38 WAVE | 1641 | 15 |
| 39 WAVE | 1662 | 1  |
| 40 WAVE | 1679 | 17 |
| 41 WAVE | 1711 | 15 |
| 42 WAVE | 1776 | 17 |

More information on the “evil waves” can be found in the supplementary file Tables S4 and S7 for December 2014 and March 2015, respectively.

Figure 3.5 depicts the count of the “evil waves” in each analysed month.

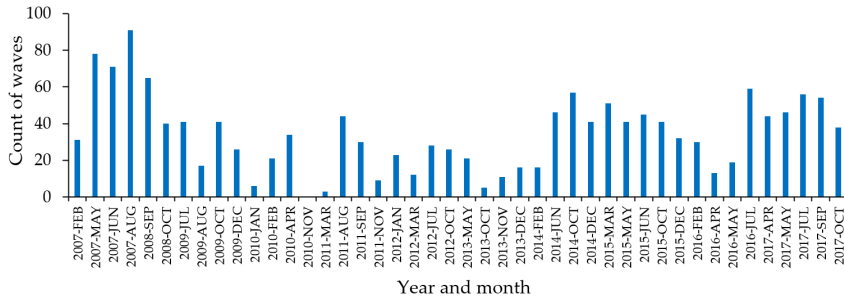


Fig. 3.5. Count of the “evil waves” in the selected month in the period 2007–2017.

In March 2015, strong geomagnetic storms occurred, with following indices, see Table 3.4.

Table 3.4

Geomagnetic Storms in St. Patrick’s Week, March 2015 (SpaceWeatherLive home page)

| # | Date       | Ap         | 00  | 03  | 06  | 09  | 12  | 15  | 18  | 21  | Kp max    | M-class flare | C-class flare |
|---|------------|------------|-----|-----|-----|-----|-----|-----|-----|-----|-----------|---------------|---------------|
|   |            |            | 03h | 06h | 09h | 12h | 15h | 18h | 21h | 00h |           |               |               |
| 1 | 2015.03.17 | <b>108</b> | 2   | 5–  | 6–  | 5+  | 8–  | 8–  | 7+  | 8–  | <b>8–</b> | <b>1</b>      | <b>2</b>      |
| 2 | 2015.03.18 | <b>47</b>  | 6   | 5–  | 4+  | 4+  | 5+  | 5+  | 5–  | 5–  | <b>6</b>  | –             | <b>18</b>     |
| 3 | 2015.03.19 | <b>26</b>  | 4+  | 4   | 4–  | 5   | 4+  | 3   | 2+  | 4–  | <b>5</b>  | –             | <b>2</b>      |
| 4 | 2015.03.22 | <b>24</b>  | 2+  | 3+  | 6+  | 5–  | 3+  | 1   | 1   | 1   | <b>6+</b> | –             | <b>2</b>      |

The impact of the strongest geomagnetic storm on March 17 (St Patrick's Day), 2015 has been widely considered in many papers (Cherniak, Zakharenkova, and Redmon, 2015; Morozova, Barlyaeva, and Barata 2020; Astafyeva, Zakharenkova, and Förster 2015; Jacobsen and Andalsvik 2016; Liu et al. 2016; Balasis, Papadimitriou, and Boutsis 2019).

The aurora borealis caused by geomagnetic storm in St. Patrick’s day, on March 17, 2015 was observed in wide area in many countries, including Latvia (Jauns home page; LSM home page).

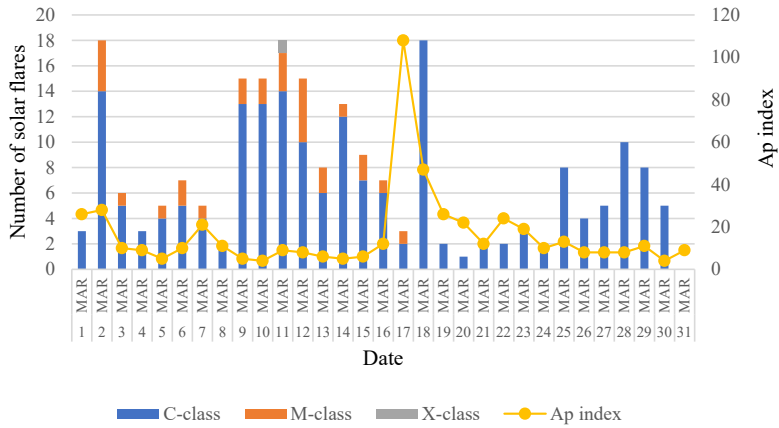


Fig. 3.6. Number of solar flares and  $A_p$  index on March 2015; data gathered from: (SpaceWeatherLive home page).

Figure 3.7 and the supplementary file Tables S5 and S7 show the plot of simultaneously occurring faulty solutions in March 2015.

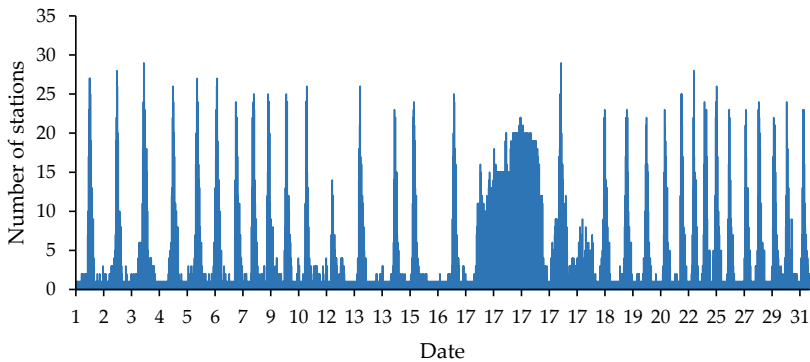


Fig. 3.7. Plot of the distribution of simultaneously occurred faulty solutions in March 2015.

The plot of discrepancies in Figure 3.8 shows that the discrepancies in the Up component of RIGA station on March 17, 2015 reached  $-531.42$  m at 17:09:00 UT.

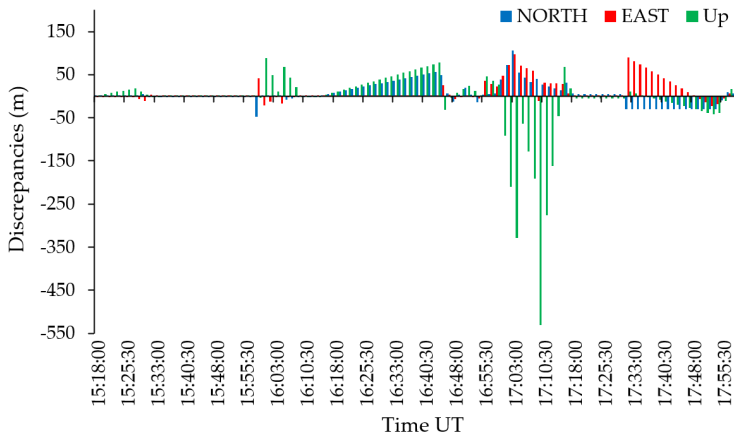


Fig. 3.8. Plot of discrepancies of station RIGA on March 17, 2015.

### 3.4 Loss of lock situations

The impact of ionosphere scintillation on GNSS performance does not end at cycle slips. Severe and continuous cycle slips lead to loss of lock. Loss of lock means that the GNSS receiver no longer tracks the signal accurately; under such status navigation messages cannot be further decoded, leading to less visible satellites for positioning, thus degrading positioning accuracy. Considering the above studies, it is quite meaningful to find how GPS receiver suffers from loss of lock under ionosphere scintillation conditions (Liu et al. 2017).

Figure 3.9 shows the plot of the distribution of simultaneously occurring faulty solutions in July 2017, where the date indicates the day of the month. The figure of a rectangular shape covering July 14, 2017, shows that there is a sequence of a repeated equal count of CORS stations with simultaneously occurring faulty solutions.

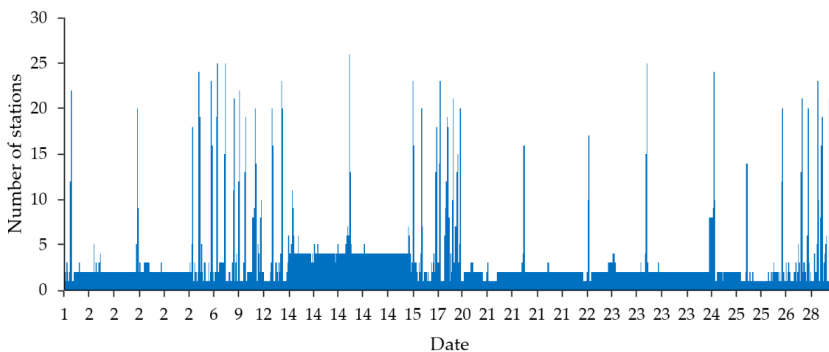


Fig. 3.9. Plot of the distribution of simultaneously occurred faulty solutions in July, 2017.

Table 3.5 is a sample of the lists of simultaneous each 90-s solution sequentially repeated faulty solutions. Inspecting the Tables of July 14, 2017 similar to the supplementary file Table S4, it appears that four CORS stations LUNI, VAIV, KREI, and SALP are repeatedly listed in each row, it means that out of five *EUPOS*<sup>®</sup>-Riga network stations, four of them on July 14, 2017 were out of normal operation. Consequently, erroneous corrections for GNSS-related measurements were disseminated. Such a search method was adopted for searching Loss-of-Lock of GNSS receivers (Leick, Rapoport, and Tatarnikov 2015). Other CORS stations' solutions in the city of Riga (OJAR, RIGA, VANG) and in other sites in Latvia (IRBE, TKMS, LIMB and others) are faulty occasionally, but not as often (Table 3.5). Therefore, there is reason to believe that this is not an effect of jamming.

The information on sequences of repeatedly occurred 90-s faulty solutions is summarized in Table 3.6, where DOY denotes the day of the year.

Table 3.5

Part of the Output Diagnostics for the month of July, 2017

| Date        | CORS station | Repetition information                          |
|-------------|--------------|---|
| 2017 JUL 13 | KREI         | 2010 after 194.516667 day repeatedly 5 times    |
| 2017 JUL 14 | KREI         | 2970 after 195.000000 day repeatedly 960 times  |
| 2017 JUL 15 | KREI         | 2972 after 196.033333 day repeatedly 2 times    |
| 2017 JUL 14 | LUNI         | 5403 after 195.000000 day repeatedly 184 times  |
| 2017 JUL 14 | LUNI         | 5563 after 195.215625 day repeatedly 160 times  |
| 2017 JUL 14 | LUNI         | 5567 after 195.389583 day repeatedly 4 times    |
| 2017 JUL 14 | LUNI         | 6135 after 195.408333 day repeatedly 568 times  |
| 2017 JUL 14 | SALP         | 11513 after 195.000000 day repeatedly 184 times |
| 2017 JUL 14 | SALP         | 11516 after 195.208333 day repeatedly 2 times   |
| 2017 JUL 14 | SALP         | 12270 after 195.214583 day repeatedly 754 times |
| 2017 JUL 15 | SALP         | 12276 after 196.030208 day repeatedly 5 times   |
| 2017 JUL 14 | VAIV         | 16460 after 195.000000 day repeatedly 960 times |
| 2017 JUL 15 | VAIV         | 16469 after 196.033333 day repeatedly 9 times   |
| 2017 JUL 15 | VAIV         | 16471 after 196.511458 day repeatedly 2 times   |
| 2017 JUL 13 | VANG         | 17076 after 194.517708 day repeatedly 2 times   |
| 2017 JUL 15 | VANG         | 17080 after 196.030208 day repeatedly 3 times   |

The detailed analysis of the discrepancies for the two stations LUNI and SALP is shown in Figures 3.10 and 3.11.

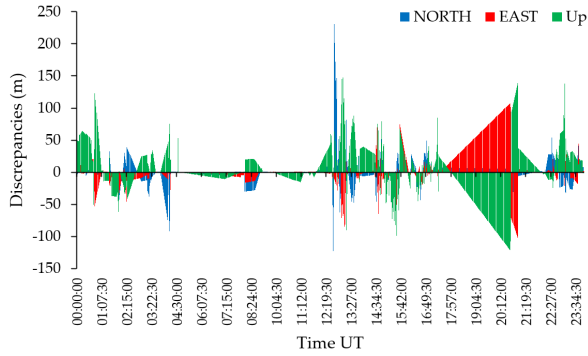


Fig. 3.10. Plot of discrepancies of station LUNI on July 14, 2017.

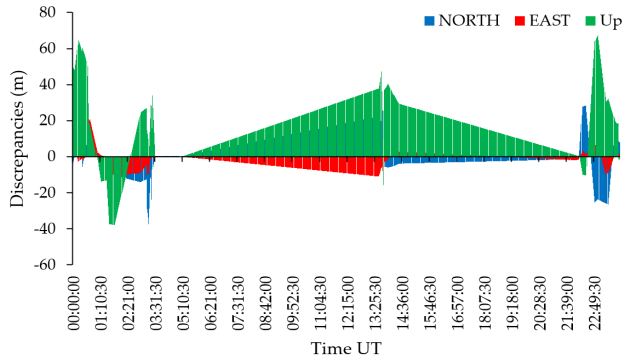


Fig. 3.11. Plot of discrepancies of station SALP on July 14, 2017.

On other dates, there are similar sequences of repeated faulty solutions in other stations of the LatPos network and the IGS/EPN station RIGA. Table 3.6 gives an example of where the sequences of repeated faulty solutions occur.

Table 3.6

Sample List of CORS Stations, Date and Time of the Sequence of Faulty Solutions

| <b>CORS station</b> | <b>DOY interval</b>   | <b>Time interval</b> | <b>Date</b> |
|---------------------|-----------------------|----------------------|-------------|
| BALV                | 188.254167 188.280208 | 6: 6: 0 6:43:30      | 7 JUL 2017  |
| DAU1                | 182.532292 182.553125 | 12:46:30 13:16:30    | 1 JUL 2017  |
| DAU1                | 200.004167 200.031250 | 0: 6: 0 0:45: 0      | 19 JUL 2017 |
| IRBE                | 205.447917 205.473958 | 10:45: 0 11:22:30    | 24 JUL 2017 |
| KREI                | 195.004167 195.998958 | 0: 6: 0 23:58:30     | 14 JUL 2017 |
| KREI                | 205.447917 205.473958 | 10:45: 0 11:22:30    | 24 JUL 2017 |
| LODE                | 188.254167 188.290625 | 6: 6: 0 6:58:30      | 7 JUL 2017  |
| LUNI                | 183.023959 183.995834 | 0:34:30 23:54: 0     | 2 JUL 2017  |

|      |            |            |          |          |             |
|------|------------|------------|----------|----------|-------------|
| LUNI | 195.004167 | 195.190625 | 0: 6: 0  | 4:34:30  | 14 JUL 2017 |
| LUNI | 195.219792 | 195.381250 | 5:16:30  | 9: 9: 0  | 14 JUL 2017 |
| LUNI | 195.412500 | 195.998958 | 9:54: 0  | 23:58:30 | 14 JUL 2017 |
| LUNI | 200.004167 | 200.031250 | 0: 6: 0  | 0:45: 0  | 19 JUL 2017 |
| LUNI | 202.022917 | 202.134375 | 0:33: 0  | 3:13:30  | 21 JUL 2017 |
| LUNI | 202.276042 | 202.494792 | 6:37:30  | 11:52:30 | 21 JUL 2017 |
| LUNI | 202.518750 | 202.553125 | 12:27: 0 | 13:16:30 | 21 JUL 2017 |
| LUNI | 202.585417 | 202.984375 | 14: 3: 0 | 23:37:30 | 21 JUL 2017 |
| LUNI | 204.017709 | 204.498959 | 0:25:30  | 11:58:30 | 23 JUL 2017 |
| LUNI | 204.518750 | 204.994791 | 12:27: 0 | 23:52:30 | 23 JUL 2017 |
| LUNI | 205.447917 | 205.473958 | 10:45: 0 | 11:22:30 | 24 JUL 2017 |
| LUNI | 206.004167 | 206.028125 | 0: 6: 0  | 0:40:30  | 25 JUL 2017 |
| LUNI | 206.261459 | 206.412500 | 6:16:30  | 9:54: 0  | 25 JUL 2017 |
| LUNI | 206.959375 | 206.998958 | 23: 1:30 | 23:58:30 | 25 JUL 2017 |
| MAZS | 188.254167 | 188.280208 | 6: 6: 0  | 6:43:30  | 7 JUL 2017  |
| RIGA | 193.477084 | 193.509375 | 11:27: 0 | 12:13:30 | 12 JUL 2017 |
| RIGA | 200.004167 | 200.023958 | 0: 6: 0  | 0:34:30  | 19 JUL 2017 |

The situation described in Tables 3.5 to 3.6 and shown in Figure 3.9 can be assumed as a corresponding stations' Loss-of-Lock of receiver. According to the Figures 3.10 and 3.11, the impact of space weather during successive scintillations of the receiver are disturbances of various magnitude, which reflect the strength of the impact. Figure 3.12 shows the count of frequencies and how often an assumed Loss-of-Lock has occurred (blue). On some days, Loss-of-Lock sequences occurred several times (2–3) per day, e.g. LUNI on July 14, 2017, and July 21, 2017 (Table 3.6). The second column (red) in Figure 3.12 shows the frequency of the days of receivers' Loss-of-Lock occurrence. The maximum number of the count of frequencies of receivers' Loss-of-Lock appears for the IGS/EPN station RIGA. The receiver of the RIGA station is mounted on a stable basement. Also, the *EUPOS*<sup>®</sup>-Riga network stations ANNI, MASK (relocated to VAIV and SALP in 2011, correspondingly), KREI, LUNI, and VANG are covering a small region of the city of Riga. The antennas are mounted on the roofs of buildings with no obstructions. The OJAR station of LatPos network is also located in the city of Riga very close to the station RIGA with the same type of receiver and antenna. However, the occurrence of the positioning disturbances is many times less.

The LatPos network (now 32 stations) covers the entire territory of Latvia. The analysis discovers that this network is most stable with less Loss-of-Lock situations, except DAU1 and LIMB stations.



### 3.5 Correlation analysis

The monthly data subsets were prepared for the correlation analysis. The monthly data subsets included the collected daily information of max TEC values over the territory of Latvia, count of cycle slips (CSLP) in all solutions and faulty solutions (CSLP (F)), and count of faulty solutions (> 10 cm). A sample of this monthly data set is presented in Table 3.7. In the supplementary file Table S1 the same data is exposed for the whole 24th solar cycle period 2007–2017.

Table 3.7

Data Subset for Correlation Analysis, March 2015

| Year | Month | Date | Geomagnetic storms and Sun flares                            | TEC  | CSLP | >10cm | CSLP(F) |
|------|-------|------|--|------|------|-------|---------|
| 2015 | MAR   | 1    | <i>Kp</i> 5+. 3 C-class flares                               | 23.4 | 466  | 252   | 6       |
| 2015 | MAR   | 2    | <i>Kp</i> 5+. 14 C-class flares. 4 M-class flares            | 31   | 497  | 280   | 3       |
| 2015 | MAR   | 3    | 5 C-class flares. M-class flare                              | 29.4 | 497  | 317   | 4       |
| 2015 | MAR   | 4    | 3 C-class flares   | 31.9 | 476  | 307   | 2       |
| 2015 | MAR   | 5    | 4 C-class flares. M-class flare                              | 33.8 | 455  | 273   | 3       |
| 2015 | MAR   | 6    | 5 C-class flares. 2 M-class flares                           | 35.1 | 479  | 253   | 3       |
| 2015 | MAR   | 7    | 4 C-class flares. M-class flare                              | 31.2 | 461  | 237   | 1       |
| 2015 | MAR   | 8    | 2 C-class flares   | 34.7 | 469  | 224   | 2       |
| 2015 | MAR   | 9    | 13 C-class flares. 2 M-class flares                          | 28   | 484  | 214   | 2       |
| 2015 | MAR   | 10   | 13 C-class flares. 2 M-class flares                          | 30.2 | 479  | 245   | 3       |
| 2015 | MAR   | 11   | 14 C-class flares. 3 M-class flares. X-class flare           | 31.3 | 520  | 198   | 2       |
| 2015 | MAR   | 12   | 10 C-class flares. 5 M-class flares                          | 30   | 445  | 184   | 1       |
| 2015 | MAR   | 13   | 6 C-class flares. 2 M-class flares                           | 33.4 | 520  | 284   | 1       |
| 2015 | MAR   | 14   | 12 C-class flares. M-class flare                             | 30.3 | 460  | 180   | 1       |
| 2015 | MAR   | 15   | 7 C-class flares. 2 M-class flares                           | 30   | 493  | 229   | 4       |
| 2015 | MAR   | 16   | 6 C-class flares. M-class flare                              | 29.3 | 464  | 250   | 4       |
| 2015 | MAR   | 17   | <i>Kp</i> 8-. <i>Ap</i> 108. 2 C-class flares. M-class flare | 40   | 1134 | 2949  | 228     |
| 2015 | MAR   | 18   | <i>Kp</i> 6. <i>Ap</i> 47. 18 C-class flares                 | 18.4 | 511  | 217   | 3       |
| 2015 | MAR   | 19   | <i>Kp</i> 5. 2 C-class flares                                | 25.2 | 497  | 252   | 5       |

|      |     |    |                         |      |     |     |   |
|------|-----|----|-------------------------|------|-----|-----|---|
| 2015 | MAR | 20 | Kp 5-. C-class flare    | 19.9 | 489 | 197 | 3 |
| 2015 | MAR | 21 | 2 C-class flares        | 25   | 484 | 179 | 3 |
| 2015 | MAR | 22 | Kp 6+. 2 C-class flares | 33.5 | 488 | 190 | 1 |
| 2015 | MAR | 23 | 3 C-class flares        | 31.7 | 488 | 174 | 1 |
| 2015 | MAR | 24 | 2 C-class flares        | 32.3 | 488 | 201 | 2 |
| 2015 | MAR | 25 | 8 C-class flares        | 32.9 | 521 | 200 | 4 |
| 2015 | MAR | 26 | 4 C-class flares        | 33.3 | 497 | 173 | 1 |
| 2015 | MAR | 27 | 5 C-class flares        | 30.9 | 502 | 164 | 4 |
| 2015 | MAR | 28 | 10 C-class flares       | 36.4 | 487 | 198 | 3 |
| 2015 | MAR | 29 | 8 C-class flares        | 35.6 | 461 | 186 | 1 |
| 2015 | MAR | 30 | 5 C-class flares        | 29   | 473 | 188 | 2 |
| 2015 | MAR | 31 | –                       | 36.3 | 482 | 187 | 2 |

Using the data as in Table 3.7 the Pearson's correlation coefficient, the covariance coefficient, regression line coefficient, solution's mean square error, both numerator and denominator from Formula (3.7),  $R^2$ , and the value of t-test, were computed and the output was made for each month.

The Pearson's correlation coefficient was computed as follows:

$$r_{xy} = \frac{\sum_{i=1}^n (x_i - \bar{x})(y_i - \bar{y})}{\sqrt{\sum_{i=1}^n (x_i - \bar{x})^2 \sum_{i=1}^n (y_i - \bar{y})^2}} \quad (3.2)$$

The covariance was computed by using the formula

$$Cov(X, Y) = \frac{\sum (x - \bar{x})(y - \bar{y})}{n} \quad (3.3)$$

Regression line was computed

$$Y_i = \hat{a} + \hat{b}X_i \quad (3.4)$$

where

$$\hat{b} = \frac{\sum (x_i - \bar{x})(y_i - \bar{y})}{\sum (x_i - \bar{x})^2} \quad (3.5)$$

and

$$\hat{a} = Y_i - \hat{b}X_i \quad (3.6)$$

$R^2$  was computed by formula

$$R^2 = \frac{\sum (\hat{y}_i - \bar{y})^2}{\sum (y_i - \bar{y})^2} \quad (3.7)$$

The Student's distribution t-test was computed by applying the formula

$$t = \frac{r_{xy}}{\sqrt{\frac{1-r_{xy}^2}{n-2}}} \quad (3.8)$$

A sample of this output is given in Table 3.8 for the four pairs of data types listed in the explanations after Table 3.8. This type of computation was carried out in two different versions: the first one with all the data discussed so far, the second version with modified data sets in which the 90-s sequences were removed, which seems to be the GNSS receiver's Loss-of-Lock product. The resulting correlation coefficients are shown in Table 3.9 and Figure 3.14.

Table 3.8

Sample of Output Data From the Correlation Analysis Program

| T | Year, month | Corr. c. | Cov.    | $\hat{a}$ | $\hat{b}$ | S     | Numerator | Denominator | R <sup>2</sup> | t-test  |
|---|-------------|----------|---------|-----------|-----------|-------|-----------|-------------|----------------|---------|
| 1 | 2014 OCT    | 0.33     | 66.0    | 387.20    | 1.97      | 32.6  | 4021.3    | 35973.4     | 0.11           | 1.9104  |
| 1 | 2014 DEC    | 0.23     | 51.6    | 380.12    | 3.15      | 53.7  | 5032.3    | 91479.1     | 0.06           | 1.2993  |
| 1 | 2015 MAR    | 0.35     | 184.1   | 235.65    | 8.77      | 110.9 | 50068.8   | 419357.4    | 0.12           | 1.9829  |
| 1 | 2015 MAY    | 0.09     | 8.7     | 482.91    | 0.42      | 21.8  | 111.9     | 14431.9     | 0.01           | 0.4761  |
| 2 | 2014 OCT    | 0.05     | 66.0    | 107.43    | 0.29      | 34.0  | 90.4      | 34726.2     | 0.00           | 0.2752  |
| 2 | 2014 DEC    | -0.20    | 51.6    | 326.23    | -1.73     | 34.9  | 1517.4    | 38077.9     | 0.04           | -1.0971 |
| 2 | 2015 MAR    | 0.32     | 184.1   | 12.59     | 7.27      | 100.9 | 34376.9   | 339500.7    | 0.10           | 1.8076  |
| 2 | 2015 MAY    | -0.17    | 8.7     | 130.47    | -1.61     | 42.3  | 1681.6    | 55275.9     | 0.03           | -0.953  |
| 3 | 2014 OCT    | 0.06     | 0.7     | 1.93      | 0.02      | 2.1   | 0.4       | 137.1       | 0.00           | 0.2990  |
| 3 | 2014 DEC    | -0.20    | -3.1    | 10.36     | -0.19     | 3.7   | 17.7      | 424.4       | 0.04           | -1.1236 |
| 3 | 2015 MAR    | 0.29     | 8.8     | -9.15     | 0.42      | 6.6   | 114.9     | 1407.4      | 0.08           | 1.6057  |
| 3 | 2015 MAY    | -0.01    | -0.1    | 2.17      | -0.00     | 1.8   | 0.0       | 96.7        | 0.00           | -0.0367 |
| 4 | 2014 OCT    | 0.11     | 125.1   | 68.60     | 0.11      | 33.8  | 418.3     | 34726.2     | 0.01           | 0.5946  |
| 4 | 2014 DEC    | 0.29     | 556.4   | 184.31    | 0.19      | 34.1  | 3252.3    | 38077.9     | 0.09           | 1.6457  |
| 4 | 2015 MAR    | 0.92     | 11154.8 | -180.64   | 0.82      | 42.6  | 285143.1  | 339500.7    | 0.84           | 12.3339 |
| 4 | 2015 MAY    | -0.10    | -94.0   | 187.07    | -0.20     | 42.7  | 589.0     | 55275.9     | 0.01           | -0.5589 |

Where:

T – Type (1 – 4):

1. TEC and cycle slips;
2. TEC and faulty solutions;
3. TEC and cycle slips in faulty solutions;
4. Cycle slips and faulty solutions.

Corr.c – Pearson's correlation coefficient (Formula (3.2)); Cov – covariance (Formula (3.3)); Linear regression line, coefficient  $\hat{a}$  and coefficient  $\hat{b}$  (Formulas (3.4) – (3.6)); S – mean square error; R<sup>2</sup> – coefficient of determination (Formula (3.7)) and its numerator and denominator values; Student's distribution t-test (Formula (3.8)).

Table 3.9 summarizes the analysis of the Pearson’s coefficients’ results in both versions – complete set of input data (Row 1) and input data without Loss-of-Lock situations (Row 2). The results for each of four data types were summarized in four columns: Pearson’s correlation coefficient within the bounds of [0; 0.4), which means very weak correlation, within the bounds of [0.4; 0.7) – moderate correlation, within bounds of [0.7; 1] – strong correlation and within the bounds of [0; -1] – negative correlation. In both versions 1 and 2, the results are very similar – weak correlation and negative correlation between TEC and count of cycle slips, TEC and count of faulty solutions, TEC and cycle slips in faulty solutions, and between cycle slips and faulty solutions. Only in 2 cases there is a very strong correlation between cycle slips and the count of faulty solutions. One of these cases is March 17, 2015.

Table 3.9  
Count of Pearson’s Correlation Coefficients Before the Removal of the Loss-of-Lock (Row 1)  
and After the Removal of the Loss-of-Lock (Row 2)

| TEC and cycle slips |            |          |          | TEC and faulty solutions |            |          |          | TEC and cycle slips from f.sol. |            |          |          | Cycle slips and f. solutions |            |          |          |
|---------------------|------------|----------|----------|--------------------------|------------|----------|----------|---------------------------------|------------|----------|----------|------------------------------|------------|----------|----------|
| [0 ; 0.4)           | [0.4; 0.7) | [0.7; 1] | [0 ; -1] | [0 ; 0.4)                | [0.4; 0.7) | [0.7; 1] | [0 ; -1] | [0 ; 0.4)                       | [0.4; 0.7) | [0.7; 1] | [0 ; -1] | [0 ; 0.4)                    | [0.4; 0.7) | [0.7; 1] | [0 ; -1] |
| 18                  | 5          | 0        | 23       | 18                       | 4          | 0        | 24       | 25                              | 4          | 0        | 17       | 25                           | 1          | 2        | 18       |
| 19                  | 5          | 0        | 22       | 16                       | 6          | 0        | 24       | 26                              | 3          | 0        | 17       | 21                           | 0          | 2        | 23       |

In Fig. 3.14, the variations of Pearson’s correlation coefficient in three cases are depicted: between TEC and count of cycle slips, TEC and count of faulty solutions (f.s.), and TEC and faulty solutions with removed Loss-of-Lock sequences (No LoL). The conclusion is that in most situations TEC max, which is defined as a smooth value over the territory of Latvia, is not comparable to the sporadic nature of real time instantaneous spatial distribution of TEC (Pi et al. 1997).

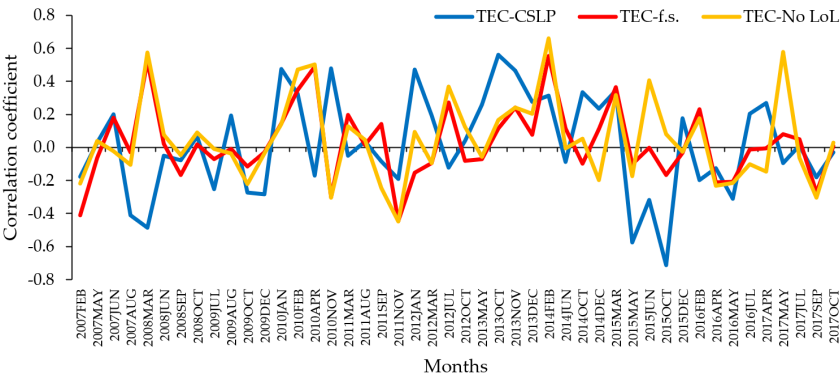


Fig. 3.14. Graph of Pearson's coefficient values in three cases.

### 3.6 ROTI correlation analysis

The ROTI index is determined from the IGS data of GNSS stations located around the Earth (CDDIS Data Archive).

The ROTI is defined as the standard deviation of the Rate of TEC (ROT) over certain time intervals. This index calculation is used by many researchers to detect ionospheric disturbances, as it is fairly simple to calculate based on the data obtained from GNSS receivers and can also eliminate the variances and uncertainties that often complicate the analysis of GNSS data (Jacobsen 2014).

To calculate the ROTI from the vertical TEC (VTEC) values, the ROT value is first calculated using the following formula;

$$ROT = \frac{VTEC_k^i - VTEC_{k-1}^i}{(t_k - t_{k-1})} \quad (3.9)$$

where  $i$  is a GPS receiver and  $t_k$  is a period of time. The ROT is calculated as the total electron content unit (TECU) per minute for each GPS station. A TECU equals  $10^{16}$  electrons/m<sup>2</sup>. Then, ROT values are used to obtain ROTI values as standard deviation at xxx(certain)-minute intervals.

$$ROTI = \sqrt{\langle ROT^2 \rangle - \langle ROT \rangle^2} \quad (3.10)$$

Additional sources of ionospheric error include amplitude and phase scintillations and a straight-line deviation of the signal paths due to break in the ionosphere. In general, these effects can be fully reproduced during periods of high ionospheric activity resulting from the interaction between the solar wind and the Earth system. Except for amplitude scintillation, the ROTI is expected to be affected by such disorders. ROTI is more closely related to phase scintillation (Jacobsen 2014).

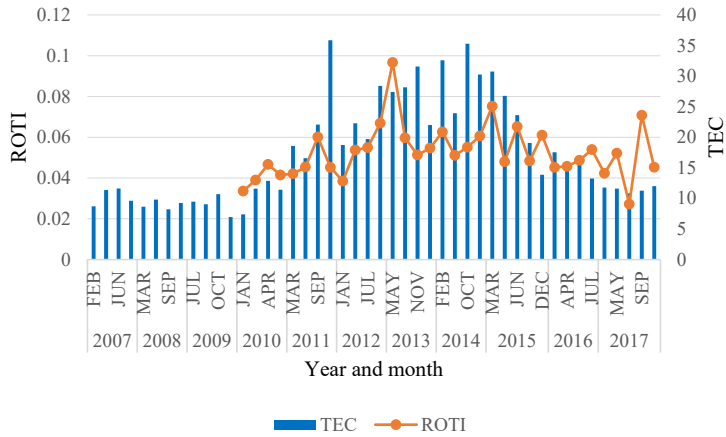


Fig. 3.15. Monthly average of daily max TECs (2007–2017) and monthly average of daily ROTI (2010–2017) data, of months, included in data post-processing and analysis in this Doctoral Thesis. Data gathered from (CODE Data archive) and (CDDIS Data Archive).

The ROTI values were available starting from year 2010 (CDDIS Data Archive). IGS ROTI maps UWM ROTIPOLARMAP product was used (see supplementary file sample Table S17) (CDDIS Data Archive). The daily ROTI maps are generated on a regular basis at UWM using data from more than 700 GPS permanent stations of the IGS, UNAVCO and EUREF networks. The ROTI is presented in a Magnetic Local Time (MLT) reference frame. 00–24 MLT time frame, 8 min MLT bin, 89.0–51.0 magnetic latitude range, 2.0 magnetic latitude bin.

The geomagnetic coordinates were calculated for all stations for 2007 and 2017 epochs according to (British Geological Survey home page).

Stations were sorted by geomagnetic latitude for both 2007 and 2017 epochs. However, sequence of the stations was not significantly affected by epoch change due to the movement of the magnetic pole.

A common definition of the MLT for each faulty solution is (Baker and Wing 1989):

$$MLT = UT + (\varphi + \phi N)/15 \tag{3.11}$$

where  $\varphi$  is the magnetic longitude of the CORS station in equation (3.11),  $\phi N$  is the geographic longitude of the North CD (centered dipole) pole and UT is the universal time specified in hours (Laundal and Richmond 2017).

Following flowchart was designed for the ROTI correlation analysis (see Figure 3.16), where:

 indicates any processing function and

○ indicates data that is displayed as result or will be used for next processing function.

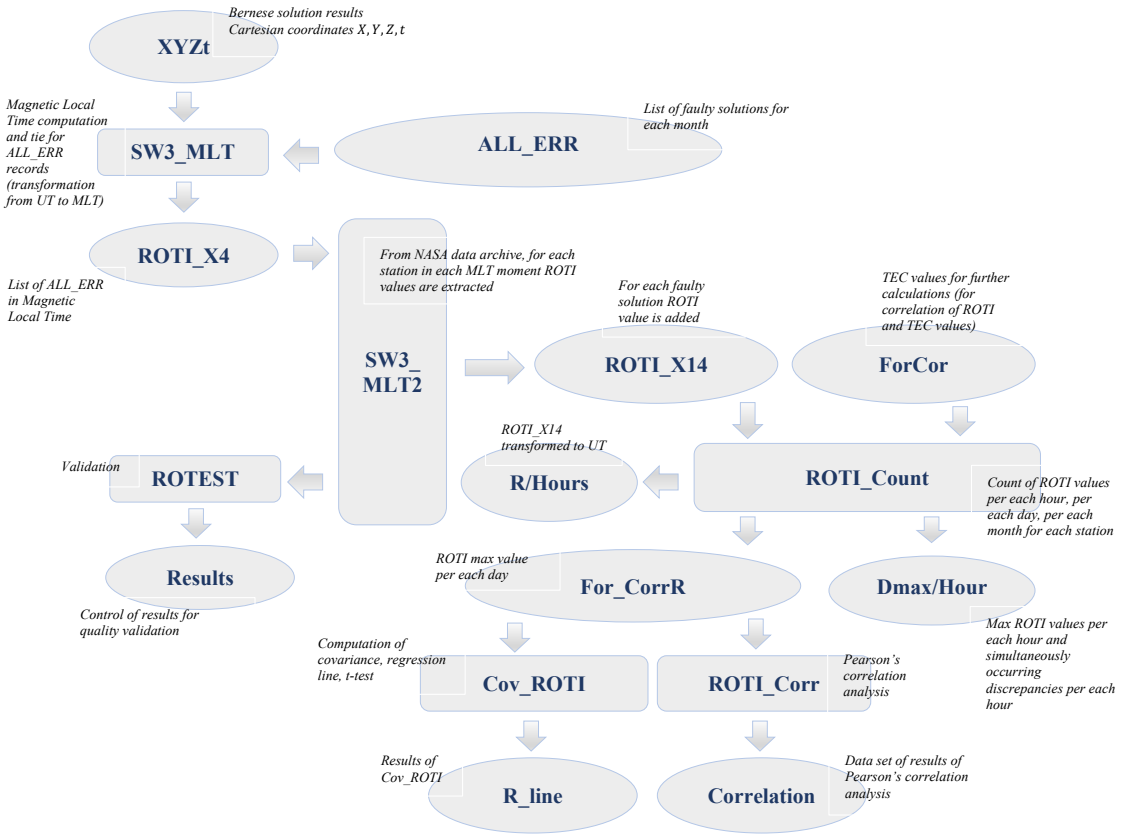


Fig. 3.16. Flowchart for the ROTI correlation analysis.

The main functions performed:

- magnetic local time (MLT) was computed for each faulty solution;
- ROTI value for each solution was found from National Aeronautics and Space Administration (NASA) data base;
- covariance and regression lines were computed on ROTI and faulty solutions for each month for each station;
- the Pearson's correlation coefficients were computed to find the relation between ROTI (monthly set  $x$ ) and count of cycle slips (monthly set  $y$ ), similarly, between ROTI and the count of faulty solutions, as well as ROTI and the count of cycle slips in faulty solutions, and between the ROTI and TEC.

Table 3.10 similarly to Table 3.9, summarizes the analysis of the Pearson’s coefficients’ results for each of four data types summarized in four columns. Correlation summary of the ROTI is given in Table 3.10.

Table 3.10

Count of Pearson’s Correlation Coefficients Between ROTI and Faulty Solutions

| ROTI and cycle slips |            |          |          | ROTI and faulty solutions |            |          |             | ROTI and cycle slips from faulty solutions |            |          |             | ROTI and TEC |            |          |             |
|----------------------|------------|----------|----------|---------------------------|------------|----------|-------------|--|------------|----------|-------------|--------------|------------|----------|-------------|
| [0 ; 0.4)            | [0.4; 0.7) | [0.7; 1] | [0 ; -1] | [0 ; 0.4)                 | [0.4; 0.7) | [0.7; 1] | [-1 ; -0.4) | [0 ; 0.4)                                  | [0.4; 0.7) | [0.7; 1] | [-1 ; -0.4) | [0 ; 0.4)    | [0.4; 0.7) | [0.7; 1] | [-1 ; -0.4) |
| 18                   | 5          | 3        | 8        | 13                        | 6          | 1        | 14          | 15   | 4          | 1        | 14          | 18           | 7          | 0        | 9           |

In Table S9 (see supplementary file), the count of faulty solutions, the count of cycle slips and the ROTI max values per day and per each hour (ROTI\*1.e04 for RIGA station) for the month of December 2014, is given and in Table S10 (see supplementary file) – for the month of March 2015. In Tables S11 and S12 (see supplementary file) similar information is given, but instead of the ROTI, the occurred positioning discrepancies are presented. For example, on March 16, the ROTI values (0.5830) are extremely high for 2 hours. Maximum positioning discrepancy is 31.32 meters. On March 17, the maximum ROTI is lower (0.1174) for 8 hours, but maximum discrepancy reaches 533.04 meters. The irregularities of ionosphere and a correlation between the count of disturbances or the count of cycle slips are difficult to define. In Tables S13–S16 (see supplementary file) similar situation for the KREI station is depicted. In Tables S2 and S5 (see supplementary file) the count of discrepancies in other Latvian CORS stations in December 2014 and March 2015, is shown.

### 3.7 Estimation of the relation between the count of faulty solutions and TEC-max

Geomagnetic storms and solar flares are extreme events. Figure 3.17 shows the monthly average of the daily maximum TECs and the average numbers of the Latvian CORS networks’ faulty 90-s solutions per station/per month. There is no close correlation between the indices of the mean TEC-max values and disturbance events. An average in a time span of 11 years is compared with sporadic events, and there is no close correlation expected.

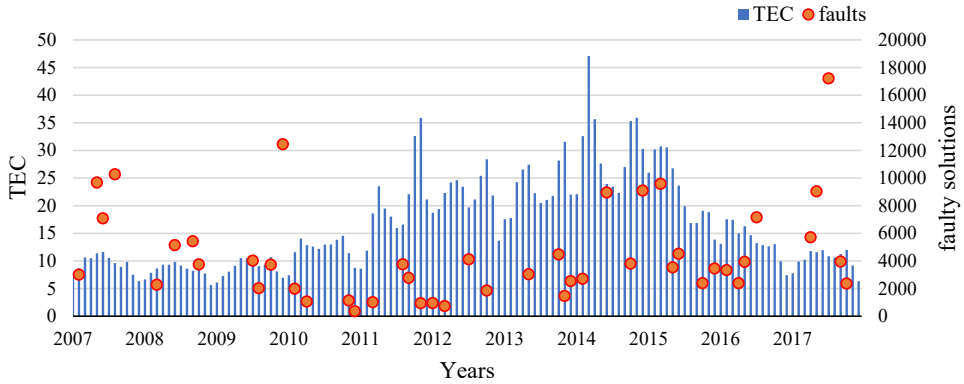


Fig. 3.17. Monthly average of daily maximum TECs and the average number of faulty solutions per month.

Figure 3.17 indicates the monthly average of the irregularities of daily maximum TECs and the average number of faulty solutions per month. Figure 3.18 shows the monthly mean values of:

- the TEC-max over the territory of Latvia;
- the mean value of the count of cycle slips counts found by the *Bernese GNSS Software v5.2* in all volume of reduced solutions, including faulty solutions (CSLP);
- the mean count of faulty solutions (F.sol.);
- the mean count of cycle slips found by *Bernese GNSS Software v5.2* in faulty solutions.

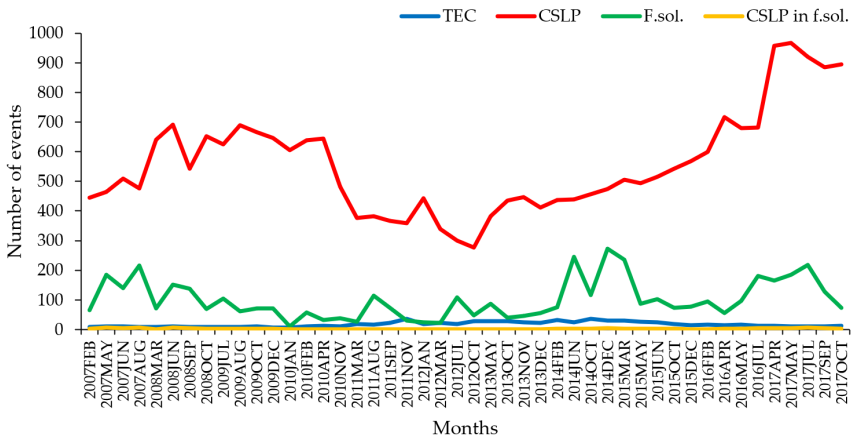


Fig. 3.18. Mean TEC-max values, mean count of cycle slips, faulty solutions, and cycle slips in faulty solutions.

The count of cycle slips is greater than faulty solutions; the *Bernese GNSS Software v5.2* identified most of the affected positions. However, still there are many faulty solutions that *Bernese GNSS Software v5.2* does not identify.

## 4. ADDITIONAL SPACE WEATHER TESTS FOR EGNOS RIMS GROUND STATIONS

The EGNOS ground segment comprise 34 RIMS spread over Europe and surrounding continents. Due to the safety related nature of EGNOS, the RIMS hosting sites are secured areas and essentially consist in airports and telecommunication space centers.

At architectural level, a given RIMS site comprise 2 to 3 independent RIMS channels (called “A/B” or “A/B/C”) depending whether or not channel C is installed.

RIMS channels A and B constitutes the measurement chains, one feeding EGNOS CPF with raw data for differential corrections computation, the other feeding EGNOS CPF check chain for comparison and integrity monitoring purposes. In order to avoid common failures, Channels A and B are diversified from a design point of view and are built by different manufacturers. Each of these channels A and B constitute a stand-alone measurement chain with its own antenna and its own receiver.

RIMS channel A and B antennas on a given site are separated by several tens of meters: not less than 60 meters, with an objective of 120 m (when feasible taking into account site constraints) (Brocard, Maier, and Busquet).

The additional space weather tests for three EGNOS RIMS ground stations (GVL, LAP, and WRS) have been performed. The GPS data from these stations GVL and GVLB, LAPA and LAPB, WRSA and WRSB from March 16–18, 2015 have been analysed.



Fig. 4.1. RIMS stations GVL, LAP, and WRS (ESA home page).

The analysis of the results of the kinematic solution results of 90-second GPS observation data was used to describe the GPS navigation situation. RIMS 16–18 March 2015 daily GPS observation data for *Bernese GNSS Software v5.2* double-difference (DD) post-processing was used to identify disturbed results caused by geomagnetic storm on March 17, 2015 (St. Patricks’ day geomagnetic storm). Daily RINEX observations (30-second sampling rate) for the full set of 3 selected RIMS stations were used and 90-second kinematic coordinates

were computed. For RIMS station coordinate computation, the reference station LAMA, METS, VIS0, and VLNS EPN reference data was used.

The mean coordinates for each RIMS station were computed in several iterations using GPS data on March 16 and 17, 2015. The data from the day of St. Patrick’s geomagnetic storm, March 17 were not included in station mean coordinate computation. The filtration of gross errors was performed. The iteration results and RMS ( $\bar{\sigma}_n$ ,  $\bar{\sigma}_e$ ,  $\bar{\sigma}_h$ ) of each solution are depicted in Table 4.1. In column “Records” the count of 90-s data used for the calculation of mean coordinate values in each filtration cycle is listed, correspondingly.

Table 4.1

Iterative Mean Coordinate Computation Results

| Station |      |     | North       | East       | Up      | Records | $\bar{\sigma}_n$ | $\bar{\sigma}_e$ | $\bar{\sigma}_h$ |
|---------|------|-----|-------------|------------|---------|---------|------------------|------------------|------------------|
| GVLA    | 2015 | MAR | 745242.395  | 125180.573 | 53.534  | 1920    | 2.367            | 0.976            | 8.321            |
| GVLA    | 2015 | MAR | 745242.329  | 125180.545 | 53.302  | 1919    | 0.031            | 0.016            | 0.110            |
| GVLA    | 2015 | MAR | 745242.330  | 125180.546 | 53.302  | 1702    | 0.014            | 0.009            | 0.043            |
| GVLA    | 2015 | MAR | 745242.330  | 125180.546 | 53.302  | 1701    | 0.014            | 0.009            | 0.043            |
| GVLA    | 2015 | MAR | 745242.330  | 125180.546 | 53.302  | 1701    | 0.014            | 0.009            | 0.043            |
| GVLA    | 2015 | MAR | 745242.328  | 125180.546 | 53.304  | 834     | 0.011            | 0.008            | 0.016            |
|         |      |     |             |            |         |         |                  |                  |                  |
| GVLB    | 2015 | MAR | 745306.340  | 125239.879 | 53.995  | 1920    | 0.133            | 0.043            | 0.314            |
| GVLB    | 2015 | MAR | 745306.340  | 125239.880 | 53.989  | 1506    | 0.024            | 0.014            | 0.051            |
| GVLB    | 2015 | MAR | 745306.340  | 125239.880 | 53.988  | 1489    | 0.024            | 0.014            | 0.050            |
| GVLB    | 2015 | MAR | 745306.340  | 125239.880 | 53.988  | 1484    | 0.024            | 0.014            | 0.049            |
|         |      |     |             |            |         |         |                  |                  |                  |
| LAPA    | 2015 | MAR | 716698.669  | 695010.428 | 35.794  | 1920    | 0.114            | 0.011            | 0.395            |
| LAPA    | 2015 | MAR | 716698.671  | 695010.427 | 35.799  | 1753    | 0.014            | 0.009            | 0.047            |
| LAPA    | 2015 | MAR | 716698.671  | 695010.427 | 35.800  | 1748    | 0.014            | 0.009            | 0.047            |
| LAPA    | 2015 | MAR | 716698.671  | 695010.427 | 35.800  | 1748    | 0.014            | 0.009            | 0.047            |
| LAPA    | 2015 | MAR | 716698.669  | 695010.428 | 35.797  | 689     | 0.012            | 0.009            | 0.017            |
|         |      |     |             |            |         |         |                  |                  |                  |
| LAPB    | 2015 | MAR | 716726.718  | 694935.605 | 34.396  | 1920    | 0.079            | 0.012            | 0.271            |
| LAPB    | 2015 | MAR | 716726.715  | 694935.605 | 34.387  | 1813    | 0.016            | 0.011            | 0.040            |
| LAPB    | 2015 | MAR | 716726.715  | 694935.605 | 34.386  | 1807    | 0.016            | 0.011            | 0.039            |
| LAPB    | 2015 | MAR | 716726.715  | 694935.605 | 34.386  | 1807    | 0.016            | 0.011            | 0.039            |
| LAPB    | 2015 | MAR | 716726.716  | 694935.605 | 34.384  | 923     | 0.013            | 0.010            | 0.017            |
|         |      |     |             |            |         |         |                  |                  |                  |
| WRSA    | 2015 | MAR | -211023.238 | 299678.081 | 125.517 | 1920    | 0.022            | 0.011            | 0.072            |
| WRSA    | 2015 | MAR | -211023.239 | 299678.081 | 125.524 | 1678    | 0.019            | 0.010            | 0.048            |
| WRSA    | 2015 | MAR | -211023.239 | 299678.081 | 125.526 | 1653    | 0.019            | 0.010            | 0.047            |
| WRSA    | 2015 | MAR | -211023.239 | 299678.081 | 125.526 | 1648    | 0.019            | 0.010            | 0.046            |
| WRSA    | 2015 | MAR | -211023.239 | 299678.082 | 125.526 | 614     | 0.013            | 0.009            | 0.017            |
|         |      |     |             |            |         |         |                  |                  |                  |
| WRSB    | 2015 | MAR | -211082.160 | 299665.763 | 128.508 | 960     | 0.023            | 0.015            | 0.077            |
| WRSB    | 2015 | MAR | -211082.157 | 299665.765 | 128.509 | 760     | 0.020            | 0.015            | 0.049            |
| WRSB    | 2015 | MAR | -211082.157 | 299665.765 | 128.509 | 759     | 0.020            | 0.015            | 0.049            |
| WRSB    | 2015 | MAR | -211082.157 | 299665.765 | 128.510 | 756     | 0.020            | 0.015            | 0.049            |
| WRSB    | 2015 | MAR | -211082.161 | 299665.767 | 128.511 | 272     | 0.014            | 0.011            | 0.016            |

The positioning discrepancies are computed with a bound of 10 cm from mean coordinate values. The count of discrepancies (faulty results) for each station is given in Table 4.2.

Table 4.2

Summary of Counts of Discrepancy Occurrences > 10 cm

|                                 |      |      |      |      |      |      |
|---------------------------------|------|------|------|------|------|------|
| 3269 TOTAL FAULTS IN MAR 2015 = | 646  | 930  | 567  | 408  | 453  | 265  |
| STATION #                       | GVLA | GVLB | LAPA | LAPB | WRSA | WRSB |

The repeating faulty results in the sequence each of the next 90 seconds are shown in Table 4.3 (see supplementary file Table R3).

Table 4.3

List of Cases of Repeatedly Occurred Discrepancies

|      |          |    |      |           |                          |                         |
|------|----------|----|------|-----------|--------------------------|-------------------------|
| 1    | 2015 MAR | 75 | GVLA | 3 after   | 75.702083 day repeatedly | 2 times **              |
| 2    | 2015 MAR | 75 | GVLA | 14 after  | 75.928125 day repeatedly | 10 times *****          |
| 3    | 2015 MAR | 76 | GVLA | 29 after  | 76.000000 day repeatedly | 12 times *****          |
| 4    | 2015 MAR | 76 | GVLA | 42 after  | 76.556250 day repeatedly | 11 times *****          |
| 5    | 2015 MAR | 76 | GVLA | 319 after | 76.568750 day repeatedly | 277 times *****277***** |
| 6    | 2015 MAR | 77 | GVLA | 460 after | 76.864583 day repeatedly | 141 times *****141***** |
| 7    | 2015 MAR | 77 | GVLA | 499 after | 77.035417 day repeatedly | 36 times ***** 36*****  |
| 8    | 2015 MAR | 77 | GVLA | 503 after | 77.114583 day repeatedly | 2 times **              |
| 9    | 2015 MAR | 77 | GVLA | 506 after | 77.117708 day repeatedly | 3 times ***             |
| 10   | 2015 MAR | 77 | GVLA | 508 after | 77.121875 day repeatedly | 2 times **              |
| 11   | 2015 MAR | 77 | GVLA | 511 after | 77.125000 day repeatedly | 3 times ***             |
| 12   | 2015 MAR | 77 | GVLA | 514 after | 77.130208 day repeatedly | 3 times ***             |
| 13   | 2015 MAR | 77 | GVLA | 517 after | 77.136458 day repeatedly | 2 times **              |
| 14   | 2015 MAR | 77 | GVLA | 519 after | 77.140625 day repeatedly | 2 times **              |
| 15   | 2015 MAR | 77 | GVLA | 524 after | 77.332292 day repeatedly | 3 times ***             |
| 16   | 2015 MAR | 77 | GVLA | 530 after | 77.372917 day repeatedly | 5 times *****           |
| 17   | 2015 MAR | 77 | GVLA | 533 after | 77.381250 day repeatedly | 3 times ***             |
| 18   | 2015 MAR | 77 | GVLA | 536 after | 77.391667 day repeatedly | 2 times **              |
| 19   | 2015 MAR | 77 | GVLA | 539 after | 77.401042 day repeatedly | 2 times **              |
| 20   | 2015 MAR | 77 | GVLA | 541 after | 77.605208 day repeatedly | 2 times **              |
| 21   | 2015 MAR | 77 | GVLA | 568 after | 77.610417 day repeatedly | 27 times ***** 27*****  |
| 22   | 2015 MAR | 77 | GVLA | 570 after | 77.653125 day repeatedly | 2 times **              |
| 23   | 2015 MAR | 77 | GVLA | 572 after | 77.656250 day repeatedly | 2 times **              |
| 24   | 2015 MAR | 77 | GVLA | 586 after | 77.659375 day repeatedly | 14 times *****          |
| 25   | 2015 MAR | 77 | GVLA | 588 after | 77.691667 day repeatedly | 2 times **              |
| 26   | 2015 MAR | 77 | GVLA | 591 after | 77.694792 day repeatedly | 3 times ***             |
| 27   | 2015 MAR | 77 | GVLA | 608 after | 77.922917 day repeatedly | 12 times *****          |
| 28   | 2015 MAR | 77 | GVLA | 612 after | 77.936458 day repeatedly | 4 times ****            |
| 29   | 2015 MAR | 77 | GVLA | 647 after | 77.963542 day repeatedly | 35 times ***** 35*****  |
| [..] |          |    |      |           |                          |                         |

The numerical values of each sequence of discrepancies are listed in Table 4.4 (extraction of the supplementary file Table R7).

Table 4.4

List of Positioning Discrepancies N, E, Up (h) Related to Table 4.3

|      |            |        |        |        |        |        |        |        |        |        |        |
|------|------------|--------|--------|--------|--------|--------|--------|--------|--------|--------|--------|
| [..] |            |        |        |        |        |        |        |        |        |        |        |
| 2    | GVLA N 10x | -0.064 | -0.033 | -0.011 | 0.036  | 0.023  | 0.016  | 0.022  | 0.013  | 0.010  | 0.015  |
| 2    | GVLA E 10x | -0.030 | -0.007 | 0.008  | 0.024  | 0.004  | 0.000  | 0.009  | 0.009  | 0.004  | 0.000  |
| 2    | GVLA h 10x | -0.229 | -0.103 | -0.104 | -0.118 | -0.212 | -0.203 | -0.204 | -0.194 | -0.192 | -0.173 |
| [..] |            |        |        |        |        |        |        |        |        |        |        |

For the most impressive occasions the plots of data set Figures (see supplementary file Figures R) are designed. These faulty sequences are qualified as a Loss-of-Lock of the corresponding RIMS station. Below an example of GVLA station N, E, Up discrepancies on March 16–18, 2015 is given.

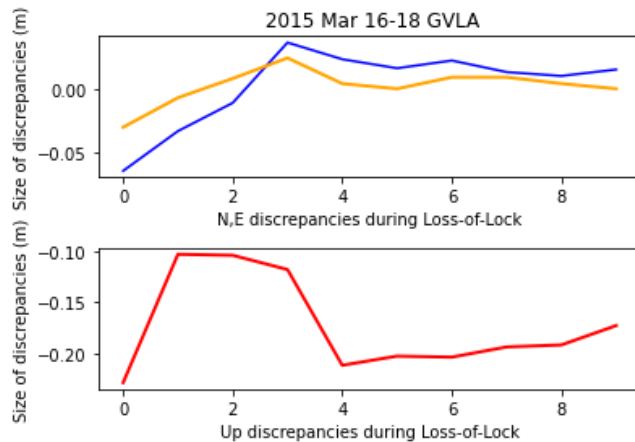


Fig. 4.2. N, E, Up discrepancies during Loss-of-Lock at the GVLA station on March 16–18, 2015.

The min and max discrepancies are listed at the end of Table 4.3 (see Table 4.3.1 and see supplementary file Table R3).

Table 4.3.1

## Min and Max Discrepancies for North, East and Up Components

| XMIN    | XMAX    | YMIN    | YMAX   | HMIN     | HMAX    |
|---------|---------|---------|--------|----------|---------|
| -54.226 | 127.017 | -26.668 | 52.395 | -203.047 | 446.572 |

In Table 4.5 the count of discrepancies per each station in days of performed analysis is depicted.

Table 4.5

## Count of Disturbances per Days on March 16-18, 2015

| 2015 Mar | 1 | 2 | 3 | 4 | 5 | 6 | 7 | 8 | 9 | 10 | 11 | 12 | 13 | 14 | 15 | 16  | 17  | 18  | 19 | 20 | 21 | 22 | 23 | 24 | 25 | 26 | 27 | 28 | 29 | 30 | 31 |
|----------|---|---|---|---|---|---|---|---|---|----|----|----|----|----|----|-----|-----|-----|----|----|----|----|----|----|----|----|----|----|----|----|----|
| 1 GVLA   | 0 | 0 | 0 | 0 | 0 | 0 | 0 | 0 | 0 | 0  | 0  | 0  | 0  | 0  | 0  | 16  | 432 | 198 | 0  | 0  | 0  | 0  | 0  | 0  | 0  | 0  | 0  | 0  | 0  | 0  | 0  |
| 2 GVLB   | 0 | 0 | 0 | 0 | 0 | 0 | 0 | 0 | 0 | 0  | 0  | 0  | 0  | 0  | 0  | 275 | 519 | 136 | 0  | 0  | 0  | 0  | 0  | 0  | 0  | 0  | 0  | 0  | 0  | 0  | 0  |
| 3 LAPA   | 0 | 0 | 0 | 0 | 0 | 0 | 0 | 0 | 0 | 0  | 0  | 0  | 0  | 0  | 0  | 40  | 407 | 120 | 0  | 0  | 0  | 0  | 0  | 0  | 0  | 0  | 0  | 0  | 0  | 0  | 0  |
| 4 LAPB   | 0 | 0 | 0 | 0 | 0 | 0 | 0 | 0 | 0 | 0  | 0  | 0  | 0  | 0  | 0  | 39  | 305 | 64  | 0  | 0  | 0  | 0  | 0  | 0  | 0  | 0  | 0  | 0  | 0  | 0  | 0  |
| 5 WRSA   | 0 | 0 | 0 | 0 | 0 | 0 | 0 | 0 | 0 | 0  | 0  | 0  | 0  | 0  | 0  | 156 | 208 | 89  | 0  | 0  | 0  | 0  | 0  | 0  | 0  | 0  | 0  | 0  | 0  | 0  | 0  |
| 6 WRSB   | 0 | 0 | 0 | 0 | 0 | 0 | 0 | 0 | 0 | 0  | 0  | 0  | 0  | 0  | 0  | 63  | 202 | 0   | 0  | 0  | 0  | 0  | 0  | 0  | 0  | 0  | 0  | 0  | 0  | 0  | 0  |

In Table 4.6 the “waves” of space weather impact (“evil waves”) where the faulty solutions did occur synchronously at least in three stations and which did continue for the several consecutive epochs of 90 seconds, are listed.

Table 4.6

## List of “Evil Waves”

| #      | N-Number of first record | S-Number of sequential records |
|--------|--------------------------|--------------------------------|
| 1 WAVE | 366                      | 9                              |
| 2 WAVE | 416                      | 12                             |
| 3 WAVE | 696                      | 181                            |
| 4 WAVE | 886                      | 117                            |
| 5 WAVE | 1007                     | 6                              |
| 6 WAVE | 1015                     | 96                             |
| 7 WAVE | 1112                     | 8                              |
| 8 WAVE | 1518                     | 10                             |

For example, the first “evil wave” fixed is at the record No. 366 of the supplementary file Table R6, and it continues for the next 9 epochs of 90-s (see Table 4.7). The beginning is at 22:15:00 UT on March 16, 2015, and the end is at 22:27:00 UT on March 16, 2015.

List of Stations where Faulty Solutions Occurred Synchronously in March 2015

|      |             |             |                          |
|------|-------------|-------------|--------------------------|
| [..] |             |             |                          |
| 366  | 2015 MAR 16 | 22:15: 0 UT | GVLB LAPB LAPA           |
| 367  | 2015 MAR 16 | 22:16:30 UT | WRSA LAPA LAPB GVLA GVLB |
| 368  | 2015 MAR 16 | 22:18: 0 UT | WRSA LAPA GVLB LAPB GVLA |
| 369  | 2015 MAR 16 | 22:19:30 UT | WRSA LAPA GVLA           |
| 370  | 2015 MAR 16 | 22:21: 0 UT | WRSA LAPA LAPB GVLA      |
| 371  | 2015 MAR 16 | 22:22:30 UT | WRSA LAPA GVLB GVLA LAPB |
| 372  | 2015 MAR 16 | 22:24: 0 UT | LAPB GVLB GVLA WRSA      |
| 373  | 2015 MAR 16 | 22:25:30 UT | WRSA GVLB GVLA LAPA LAPB |
| 374  | 2015 MAR 16 | 22:27: 0 UT | GVLB LAPA GVLA LAPB WRSA |
| [..] |             |             |                          |

The 3rd wave starts at the record No. 696 (see supplementary file Table R6) on March 17 at 14:01:30 UT and it continues till 17:18:30 UT consecutive 181 epochs of 90-s.

The frequency of the faulty solutions is depicted in Figure 4.3.

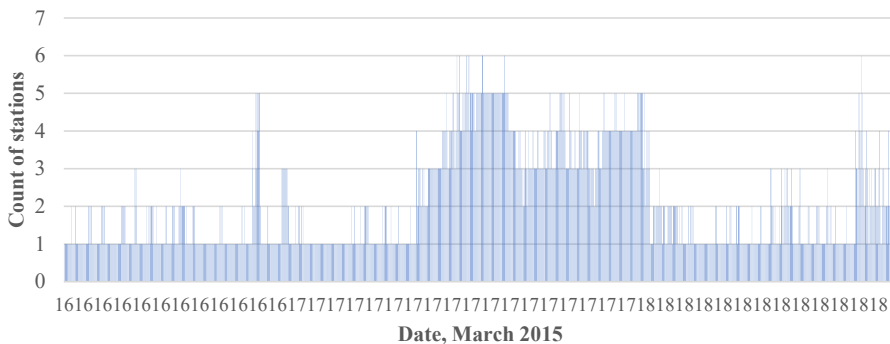


Fig. 4.3. Frequency of faulty solutions on March 16–18, 2015 in the set of RIMS stations GVLA and GVLB, LAPA and LAPB, and WRSA and WRSB.

In Table 4.8 (extracted from the supplementary file Table R8) positioning discrepancies which occurred synchronously in each of recorded epochs (hh:mm:ss) for corresponding stations listed in Table 4.7 (extracted from the supplementary file Table R6) are depicted. No. of records related to the synchronous occurrences, see Table 4.7 (extracted from the supplementary file Table R6), where No of groups = 1591; dx = discrepancy of North; dy = discrepancy of East; dh = discrepancy of Up component; Dist =  $\sqrt{dx^2 + dy^2}$ ; Az = azimuth ( $\arctan dy/dx$ ).

Table 4.8

Synchronously Occurred Positioning Discrepancies. No. of Records Related to  
Synchronous Occurrences in Table 4.7

| DISCREPANCIES |                         | #        | dx (m) | dy (m) | dh (m) | Dist (m) | Az (dg) |
|---------------|-------------------------|----------|--------|--------|--------|----------|---------|
| [.]           |                         |          |        |        |        |          |         |
| 366           | 2015 MAR 16 22:15:00 UT | GVLB 444 | 0.021  | 0.020  | 0.192  | 0.194    | 43.6    |
|               |                         | LAPB 446 | 0.070  | 0.008  | 0.368  | 0.375    | 6.5     |
|               |                         | LAPA 445 | 0.213  | -0.005 | 0.787  | 0.815    | -1.3    |
| 367           | 2015 MAR 16 22:16:30 UT | WRSA 451 | 0.010  | -0.005 | 0.126  | 0.126    | -26.6   |
|               |                         | LAPA 449 | -0.090 | -0.011 | -0.277 | 0.291    | -173.0  |
|               |                         | LAPB 450 | -0.120 | 0.015  | -0.334 | 0.355    | 172.9   |
|               |                         | GVLA 447 | 0.317  | 0.130  | 1.135  | 1.186    | 22.3    |
|               |                         | GVLB 448 | 1.034  | 0.435  | 3.871  | 4.030    | 22.8    |
| 368           | 2015 MAR 16 22:18:00 UT | WRSA 456 | 0.015  | -0.015 | 0.137  | 0.139    | -45.0   |
|               |                         | LAPA 454 | -0.237 | -0.020 | -0.773 | 0.809    | -175.2  |
|               |                         | GVLB 453 | -0.529 | -0.203 | -1.635 | 1.730    | -159.0  |
|               |                         | LAPB 455 | 0.503  | 0.029  | 1.829  | 1.897    | 3.3     |
|               |                         | GVLA 452 | -0.649 | -0.275 | -2.281 | 2.387    | -157.0  |
| 369           | 2015 MAR 16 22:19:30 UT | WRSA 459 | 0.009  | -0.013 | 0.125  | 0.126    | -55.3   |
|               |                         | LAPA 458 | -0.090 | -0.023 | 0.264  | 0.280    | -165.7  |
|               |                         | GVLA 457 | 0.104  | 0.065  | 0.472  | 0.488    | 32.0    |
| 370           | 2015 MAR 16 22:21:00 UT | WRSA 463 | 0.015  | -0.007 | 0.147  | 0.148    | -25.0   |
|               |                         | LAPA 461 | -0.169 | -0.026 | -0.501 | 0.529    | -171.3  |
|               |                         | LAPB 462 | -0.221 | -0.018 | -0.653 | 0.690    | -175.3  |
|               |                         | GVLA 460 | -0.232 | -0.098 | -0.751 | 0.792    | -157.1  |
| 371           | 2015 MAR 16 22:22:30 UT | WRSA 468 | 0.018  | -0.002 | 0.120  | 0.121    | -6.3    |
|               |                         | LAPA 466 | -0.060 | -0.016 | -0.147 | 0.160    | -165.1  |
|               |                         | GVLB 465 | -0.102 | -0.049 | -0.263 | 0.286    | -154.3  |
|               |                         | GVLA 464 | -0.095 | -0.036 | -0.286 | 0.304    | -159.2  |
|               |                         | LAPB 467 | -0.314 | -0.029 | -0.977 | 1.027    | -174.7  |
| 372           | 2015 MAR 16 22:24:00 UT | LAPB 471 | -0.063 | 0.006  | -0.136 | 0.150    | 174.6   |
|               |                         | GVLB 470 | -0.087 | -0.041 | -0.188 | 0.211    | -154.8  |
|               |                         | GVLA 469 | -0.082 | -0.037 | -0.267 | 0.282    | -155.7  |
|               |                         | WRSA 472 | 0.191  | 0.042  | 0.463  | 0.503    | 12.4    |
| 373           | 2015 MAR 16 22:25:30 UT | WRSA 477 | 0.020  | -0.010 | 0.129  | 0.131    | -26.6   |
|               |                         | GVLB 474 | -0.066 | -0.027 | -0.110 | 0.131    | -157.8  |
|               |                         | GVLA 473 | -0.069 | -0.038 | -0.248 | 0.260    | -151.2  |
|               |                         | LAPA 475 | -0.098 | -0.024 | -0.252 | 0.271    | -166.2  |
|               |                         | LAPB 476 | -0.105 | -0.001 | -0.293 | 0.31     | -179.5  |
| 374           | 2015 MAR 16 22:27:00 UT | GVLB 479 | -0.089 | -0.019 | -0.122 | 0.152    | -167.9  |
|               |                         | LAPA 480 | -0.058 | -0.016 | -0.142 | 0.154    | -164.6  |
|               |                         | GVLA 478 | -0.066 | -0.031 | -0.237 | 0.248    | -154.8  |
|               |                         | LAPB 481 | -0.129 | -0.014 | -0.328 | 0.353    | -173.8  |
|               |                         | WRSA 482 | 0.180  | 0.050  | 0.410  | 0.451    | 15.5    |
| [.]           |                         |          |        |        |        |          |         |

In the supplementary file Figures R9–R24, the daily time series of RIMS station data are depicted.

Table 4.9

Positioning Discrepancies in RIMS Stations WRSA, LAPA and LAPB, and GVLB and GVLB on March 17, 2015 at 15:28:30 UT and at Following 90 Seconds

| DISCREPANCIES |          |                | #           | dx (m) | dy (m)  | dh (m)  | Dist (m) | Az (dg)        |        |
|---------------|----------|----------------|-------------|--------|---------|---------|----------|----------------|--------|
| 754           | 2015 MAR | 17 15:28:30 UT | WRSA        | 1101   | 0.000   | 0.009   | 0.120    | 0.120          | 90.0   |
|               |          |                | <b>LAPB</b> | 1100   | -0.087  | 0.033   | 0.436    | <b>0.446</b>   | 159.2  |
|               |          |                | GVLB        | 1098   | 0.700   | -1.622  | -0.649   | 1.882          | -66.7  |
|               |          |                | GVLA        | 1097   | -53.826 | -19.559 | -12.408  | 58.598         | -160.0 |
|               |          |                | <b>LAPA</b> | 1099   | -16.684 | 46.905  | -199.657 | <b>205.770</b> | 109.6  |
| 755           | 2015 MAR | 17 15:30: 0 UT | WRSA        | 1106   | -0.012  | 0.012   | 0.106    | 0.107          | 135.0  |
|               |          |                | <b>LAPB</b> | 1105   | -0.083  | 0.025   | 0.539    | <b>0.546</b>   | 163.2  |
|               |          |                | GVLB        | 1103   | 0.715   | -1.655  | -0.653   | 1.917          | -66.6  |
|               |          |                | GVLA        | 1102   | -53.469 | -18.643 | -15.603  | 58.736         | -160.8 |
|               |          |                | <b>LAPA</b> | 1104   | -16.844 | 47.730  | -203.047 | <b>209.261</b> | 109.4  |

Below, in Figure 4.4 the size of the N (blue color), E (orange color), Up (red color) coordinate discrepancies during Loss-of-Lock at RIMS station LAPA from March 16–17, 2015, is shown.

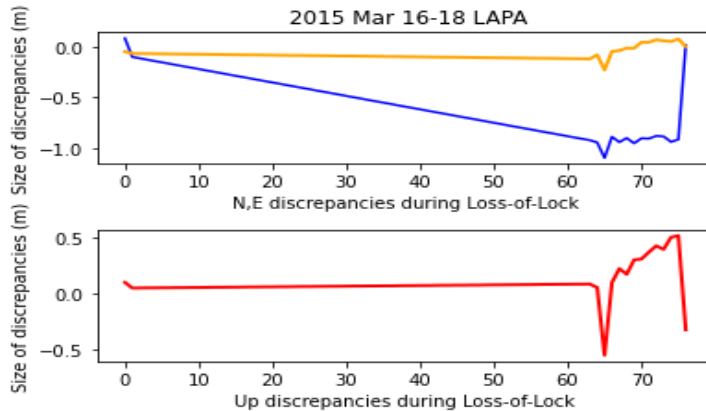


Fig. 4.4. Size of the N (blue color), E (orange color), Up (red color) coordinate discrepancies during Loss-of-Lock at RIMS station LAPA from March 16–18, 2015.

The analysis of selected RIMS station GPS data on 16–18 March, 2015 discovers that positioning results are impacted by a very strong St. Patrick’s geomagnetic storm ( $Kp$  index +8). GVLA and GVLB were most affected. Less influenced were stations WRSA and WRSB.

When comparing the max discrepancies in RIMS stations with Latvian CORS stations on March 17, 2015, it appeared, that in RIMS stations the max discrepancies were detected about 3 h before than they appeared in Latvian CORS stations (see supplementary files R9 and R10, respectively).

## CONCLUSIONS

The novelty of this study is the developed and applied methodology for analysis of space weather impact on CORS stations.

The following has been achieved in the development of the Doctoral Thesis:

- 1) The amount of disturbed results has been discovered and statistics of disturbance size have been characterized.
- a) The total count of *Bernese GNSS Software v5.2* solutions reached 36,728,129, of which 203,981 (i.e. 0.6 %) solutions appeared with discrepancies in position greater than 10 cm ( $3\sigma$ ). Including the 10 cm threshold, the count reached 204,022. There were 744,689 cycle slips (CSLP) identified by *Bernese GNSS Software v5.2*. This covers 2 % of all *Bernese GNSS Software v5.2* solutions. In the subset of disturbed solutions just 4849 cycle slips (i.e. 0.6 % of all cycle slips) of these were identified by *Bernese GNSS software v5.2*.
- b) The largest positioning disturbances and their frequency appeared in March 2015, during the highest Sun activity of the 24th solar cycle in years 2007–2017. It is the only detected case when solar event correlates with coordinate discrepancies. On March 17, 2015 the solar activity event created a significant geomagnetic storm causing serious positioning discrepancies in the Latvian CORS stations reaching more than 500 m in some cases. A very strong geomagnetic storm occurred in September 2017 over the territories of Canada and USA; however, this geomagnetic storm did not impact the territory of Latvia.
- 2) Taking into account space weather indices and ionospheric TEC and ROTI levels of the selected months of the time period 2007–2017, the correlation was sought and a conclusions was obtained that the performed Pearsons' correlation analysis reveals that the global TEC and ROTI approximation models are not suitable for the study of the local TEC and ROTI anomalies.
- 3) Most influenced CORS stations were found and conclusions on the reason of network affected instability were drawn.
- a) The most affected appear to be the *EUPOS*<sup>®</sup>-Riga network stations. An average 3.9 % of all faulty solutions relate to *EUPOS*<sup>®</sup>-Riga stations while just 1.8 % relate to LatPos stations.
- b) One might think that the eventual dependency exists between the Loss-of-Lock frequency of GNSS receivers and the type of receivers. However, it seems that the

number of CORS stations and the size of the covered territory are more important (LatPos network gives better results).

- c) Statistical analysis discovered that LatPos network functionality is of high quality, but space weather impact to *EUPOS*<sup>®</sup>-Riga network is critical.
- 4) The results of the research, obtained within the framework of the Doctoral Thesis, by performing additional test analysis at EGNOS RIMS ground stations WRSA and WRSB, GVL A and GVL B, LAPA and LAPB, confirms, that using the presented methodology, the severe space weather (geomagnetic storms') impact can be detected also in regional SBAS (in this particular case – EGNOS).

This research, confirms that the myth of weak effects of space weather in the mid-latitudes, is mistaken; this has been concluded according to an analysis of data from CORS GPS observations collected over 11 years.

This methodology can be used to analyse space weather impact on any other CORS stations as well as regional SBAS (for example EGNOS). The obtained information is critical in order to understand better the impact of space weather processes on GPS observation results in a specific area (region or country) and to predict the possible station behaviour and the data reliability.

Speaking about Latvia, the Thesis author thinks that, firstly, it is necessary to work seriously in order to create an understanding of the existence of this problem in GNSS positioning, navigation and accurate time synchronization not only in Latvia, but in all midlatitude countries, including Latvia, Estonia, and Lithuania. Only when the effects of space weather caused errors are explained to the wide audience of GNSS users, it will be possible to draw government attention to this topic. The Thesis author considers informing the public of Latvia as her first task in the coming months and years. The effects of space weather are being studied very seriously in Poland, Spain, and other member states of the European Space Agency.

# APPENDICES

## Supplementary files S

Table S1: List of geomagnetic storms and Sun flares, count of TEC-max, identified cycle slips, position discrepancies > 10 cm (faulty solutions) and faulty solutions with cycle slips in the Latvian CORS 90 second solutions;

Table S2: List of faulty solutions per station in December 2014;

Table S3: List of “evil waves” in December 2014;

Table S4: List of stations where faulty solutions occurred synchronously in December 2014;

Table S5: List of faulty solutions per station in March 2015;

Table S6: List of “evil waves” in March 2015;

Table S7: List of stations where faulty solutions occurred synchronously in March 2015;

Table S8: Sample data of discrepancies;

Table S9: RIGA station’s ROTI max values per day and per each hour, December 2014;

Table S10: RIGA station’s ROTI max values per day and per each hour, March 2015;

Table S11: Max values (m) of discrepancies per day and per each hour, December 2014;

Table S12: Max values (m) of discrepancies per day and per each hour, March 2015;

Table S13: KREI station’s ROTI max values per day and per each hour, December 2014;

Table S14: KREI station’s ROTI max values per day and per each hour, March 2015;

Table S15: Max values (m) of discrepancies per day and per each hour, December 2014;

Table S16: Max values (m) of discrepancies per day and per each hour, March 2015;

Table S18: Number of total faults per each station of the selected months (2007–2017);

Table S19: Cycle slips per each station of the selected months (2007–2017);

Table S20: Summary table on the GPS signal registration faults.

## **Supplementary files R**

Table R1: Iterative mean coordinate computation results;

Table R2: Summary of count of discrepancy occurrences > 10 cm;

Table R3: List of cases of repeatedly occurred discrepancies;

Table R4: Count of disturbances per days on March 16–18, 2015;

Table R5: List of “evil waves”;

Table R6: List of stations where faulty solutions occurred synchronously in March 2015;

Table R7: List of positioning discrepancies (N, E, Up (h) related to Table R2;

Table R8: Synchronously occurred positioning discrepancies. No. of records related to synchronous occurrences in Table R6;

Table R9: Max discrepancies in the RIMS stations on March 17, 2015;

Table R10: Max discrepancies in the Latvian CORS stations on March 17, 2015;

Figures R9–R24: Daily time series of RIMS station data.

## LIST OF REFERENCES

1. Abele, M., J. Balodis, K. Balodis, M. Normand, I. Janpaule, I. Mitrofanovs, A. Rubans, G. Silabriedis, and A. Zarins. 2008. "Implementation of New Positioning System in Riga." *International Symposium EUREF*, 6 pages.
2. Ahmed, El-Rabanny. 2006. *Introduction to GPS: The Global Positioning System* (2nd edition). Artech House, INC.
3. Leick, Alfred. 2004. *GPS satellite surveying* (3rd edition). John Wiley.
4. Amory-Mazaudier, C., R. Fleury, S. Gadimova, and A. Touzani. 2017. "Space Weather, from the Sun to the Earth, the key role of GNSS." <https://hal.sorbonne-universite.fr/hal-01489731>.
5. Astafyeva, Elvira, Irina Zakharenkova, and Mathias Förster. 2015. "Ionospheric response to the 2015 St. Patrick's Day storm: A global multi-instrumental overview." *Journal of Geophysical Research: Space Physics*, 120(10), 9023–9037. <https://doi.org/10.1002/2015JA021629>.
6. Astafyeva, Elvira, I. Zakharenkova, K. Hozumi, P. Alken, P. Coisson, M. R. Hairston, and W. R. Coley. 2018. "Study of the Equatorial and Low-Latitude Electrodynamic and Ionospheric Disturbances During the 22–23 June 2015 Geomagnetic Storm Using Ground-Based and Spaceborne Techniques." *Journal of Geophysical Research: Space Physics*, 123(3), 2424–2440. <https://doi.org/10.1002/2017JA024981>.
7. Balasis, G., C. Papadimitriou, and A. Z. Boutsis. 2019. "Ionospheric response to solar and interplanetary disturbances: A Swarm perspective." *Philosophical Transactions of the Royal Society A: Mathematical, Physical and Engineering Sciences*, 377(2148). <https://doi.org/10.1098/rsta.2018.0098>.
8. Balodis, Janis, Madara Normand, and Inese Varna. 2021. "Extreme solar events' impact on GPS positioning results." *Remote Sensing* (Vol. 13, Issue 18). MDPI. <https://doi.org/10.3390/rs13183624>.
9. Balodis, Janis, Madara Normand, and Ansis Zarins. 2023. "The Movement of GPS Positioning Discrepancy Clouds at a Mid-Latitude Region in March 2015". *Remote Sensing* 15, no. 8: 2032. <https://doi.org/10.3390/rs15082032>.
10. Balodis, Janis, Gunars Silabriedis, Diana Haritonova, Maris Kalinka, Inese Janpaule, Katerina Morozova, Izolde Jumare, Ingus Mitrofanovs, Janis Zvirgzds, Janis Kaminskis, and Ivars Liepins. 2015. "Development of the one centimeter accuracy geoid model of

- Latvia for GNSS measurements.” *IOP Conference Series: Materials Science and Engineering*, 96(1). <https://doi.org/10.1088/1757-899X/96/1/012037>.
11. Balodis, Janis, Inese Varna, Diana Haritonova, Madara Normand, and Gunars Silabriedis. 2017. “Ground Based Kinematic GNSS Observation Results Affected by Space Weather Fluctuations in 2015.” *Baltic Journal of Modern Computing*, 5(3). <https://doi.org/10.22364/bjmc.2017.5.3.01>.
  12. Balodis, Janis, Inese Varna, and Madara Normand. 2018. “Removing Space Weather Influence.” *Baltic Journal of Modern Computing*, 6(4). <https://doi.org/10.22364/bjmc.2018.6.4.05>.
  13. Bernese GNSS Software home page. <http://www.bernese.unibe.ch>.
  14. Parkinson, Bradford W. and James J. Spilker Jr. 1995. *Global Positioning System: Theory and Applications Volume I* (Paul Zarchan, Penina Axelrad, and Per Enge, Eds.; ISBN 1-56347-107-8, Vol. 163).
  15. British Geological Survey home page. [http://www.geomag.bgs.ac.uk/data\\_service/models\\_compass/coord\\_calc.html](http://www.geomag.bgs.ac.uk/data_service/models_compass/coord_calc.html).
  16. Brocard, D., T. Maier, and C. Busquet. “EGNOS Ranging and Integrity Monitoring Stations (RIMS).” [http://www.egnospro.esa.int/Publications/GNSS%202000/GNSS2000\\_rims.pdf](http://www.egnospro.esa.int/Publications/GNSS%202000/GNSS2000_rims.pdf).
  17. CDDIS Data Archive. <https://cdsis.nasa.gov/archive/gnss/products/ionex/>.
  18. Cherniak, I., I. Zakharenkova, and R. J. Redmon. 2015. “Dynamics of the high-latitude ionospheric irregularities during the 17 March 2015 St. Patrick’s Day storm: Ground-based GPS measurements.” *Space Weather*, 13(9), 585–597. <https://doi.org/10.1002/2015SW001237>.
  19. Circiu, Mihaela-Simona, Michael Felux, Patrick Remi, Lai Yi, Boubeker Belabbas, and Sam Pullen. 2014. “Evaluation of Dual Frequency GBAS Performance using Flight Data.” *Proceedings of the ION ITM*. ION ITM, 27-29 Jan. 2014, San Diego, CA, USA.
  20. CODE Data archive. “<ftp://ftp.unibe.ch/aiub/BSWUSER50/ATM/>.”
  21. Colvin, and Thomas. 2019. “Next Step Space Weather Benchmarks.”
  22. Coster, A., and A. Komjathy. 2008. “Space Weather and the Global Positioning System.” *Space Weather*, 6(6). <https://doi.org/10.1029/2008sw000400>.
  23. Dach, Rolf, Simon Lutz, Peter Walser, and Pierre Fridez. 2015. *Bernese GNSS Software Version 5.2*. <https://doi.org/10.7892/boris.72297>.
  24. de La Beaujardière, O., J. M. Retterer, R. F. Pfaff, P. A. Roddy, C. Roth, W. J. Burke, Y. J. Su, M. C. Kelley, R. R. Ilma, G. R. Wilson, L. C. Gentile, D. E. Hunton, and D. L.

- Cooke. 2009. "C/NOFS observations of deep plasma depletions at dawn." *Geophysical Research Letters*, 36(18). <https://doi.org/10.1029/2009GL038884>.
25. DLR home page. [https://www.dlr.de/content/en/articles/news/2018/4/20181008\\_3d-elevation-model-tandem-x-mission.html](https://www.dlr.de/content/en/articles/news/2018/4/20181008_3d-elevation-model-tandem-x-mission.html).
26. Dobelis, Didzis, Jānis Zvirgzds, and Māris Kaļinka. 2017. "High ionospheric activity effects on LatPos RTK network performance in Latvia." *IOP Conference Series: Materials Science and Engineering*, 251(1). <https://doi.org/10.1088/1757-899X/251/1/012064>.
27. ECAC home page. <https://www.ecac-ceac.org/latvia>.
28. ESA home page. <https://gssc.esa.int/navipedia/index.php/File:RIMS.png>.
29. ESA home page.  
[https://www.esa.int/About\\_Us/Corporate\\_news/Member\\_States\\_Cooperating\\_States](https://www.esa.int/About_Us/Corporate_news/Member_States_Cooperating_States).
30. ESA home page.  
[https://www.esa.int/Science\\_Exploration/Space\\_Science/What\\_are\\_solar\\_flares](https://www.esa.int/Science_Exploration/Space_Science/What_are_solar_flares).
31. EUPOS® ISC. 2013.
32. EUREF home page. [http://epncb.oma.be/\\_networkdata/datacalendar.php](http://epncb.oma.be/_networkdata/datacalendar.php).
33. EUREF home page.  
[http://www.epncb.oma.be/\\_networkdata/siteinfo4onestation.php?station=RIGA00LVA](http://www.epncb.oma.be/_networkdata/siteinfo4onestation.php?station=RIGA00LVA).
34. Fagundes, P. R., M. Pezzopane, J. B. Habarulema, K. Venkatesh, M. A. L. Dias, A. Tardelli, A. J. de Abreu, V. G. Pillat, A. Pignalberi, M. J. A. Bolzan, B. A. G. Ribeiro, F. Vieira, J. P. Raulin, C. M. Denardini, M. O. Arcanjo, and G. K. Seemala. 2020. "Ionospheric disturbances in a large area of the terrestrial globe by two strong solar flares of September 6, 2017, the strongest space weather events in the last decade." *Advances in Space Research*, 66(7), 1775–1791. <https://doi.org/10.1016/j.asr.2020.06.032>.
35. Feltens, J., and S. Schaer. 1998. "IGS Products for the Ionosphere."
36. Free ocean tide loading provider home page.  
<http://holt.oso.chalmers.se/loading/index.html>.
37. Guo, J., W. Li, X. Liu, Q. Kong, C. Zhao, and B. Guo. 2015. "Temporal-spatial variation of global GPS-Derived total electron content, 1999-2013." *PLoS ONE*, 10(7). <https://doi.org/10.1371/journal.pone.0133378>.
38. H2020 HSNV home page. <https://h2020nav.esa.int/page/about-h2020>.
39. H2020 HSNV home page. <https://h2020nav.esa.int/project/h2020-037>.
40. Hairston, M., W. R. Coley, and R. Stoneback. 2016. "Responses in the polar and equatorial ionosphere to the March 2015 St. Patrick Day storm." *Journal of Geophysical Research: Space Physics*, 121(11), 11,213-11,234. <https://doi.org/10.1002/2016JA023165>.

41. Haritonova, Diana. 2016. "Evaluation of high-precision technique application for observations of Earth's crust movements in Latvia." Riga: Riga Technical University, Faculty of Civil Engineering, Department of Geomatics. Doctoral Thesis.
42. Hlubek, Nikolai, Jens Berdermann, Volker Wilken, Stefan Gewies, Norbert Jakowski, Mogese Wassae, and Baylie Damtie. 2014. "Scintillations of the GPS, GLONASS, and Galileo signals at equatorial latitude." *Journal of Space Weather and Space Climate*, 4. <https://doi.org/10.1051/swsc/2014020>.
43. Huang, C., G. R. Wilson, M. R. Hairston, Y. Zhang, W. Wang, and J. Liu. 2016. "Equatorial ionospheric plasma drifts and O<sup>+</sup> concentration enhancements associated with disturbance dynamo during the 2015 St. Patrick's Day magnetic storm." *Journal of Geophysical Research: Space Physics*, 121(8), 7961–7973. <https://doi.org/10.1002/2016JA023072>.
44. IAGA home page. <https://iaga-aiga.org>.
45. IAGA Working Group V-DAT home page. <https://www.ngdc.noaa.gov/IAGA/vdat/>.
46. IGS home page. <http://www.igs.org/about>.
47. Imel, D. A. 1994. "Evaluation of the TOPEX/POSEIDON dual-frequency ionosphere correction." *Journal of Geophysical Research*, 99(C12), 24895. <https://doi.org/10.1029/94JC01869>.
48. ISGI home page. [http://isgi.unistra.fr/about\\_indices.php](http://isgi.unistra.fr/about_indices.php).
49. ISGI home page. [http://isgi.unistra.fr/geomagnetic\\_indices.php](http://isgi.unistra.fr/geomagnetic_indices.php).
50. Jacobsen, Knut Stanley. 2014. "The impact of different sampling rates and calculation time intervals on ROTI values." *Journal of Space Weather and Space Climate*, 4, A33. <https://doi.org/10.1051/swsc/2014031>.
51. Jacobsen, Knut Stanley, and Yngvild Linnea Andalsvik. 2016. "Overview of the 2015 St. Patrick's day storm and its consequences for RTK and PPP positioning in Norway." *Journal of Space Weather and Space Climate*, 6, A9. <https://doi.org/10.1051/swsc/2016004>.
52. Janpaule, Inese. 2014. "Methods for the determination of high precision Latvian geoid model [in Latvian]." Riga: Riga Technical University, Faculty of Civil Engineering Institute of Transport Structures. Doctoral Thesis.
53. Jauns home page. <http://jauns.lv/raksts/zinas/56804-latvija-novero-pedejo-gadu-spilgtako-ziemelblazmu-foto-video>.
54. Jauns home page. <https://jauns.lv/foto/zinas/9685-ziemelblazma-jurmala#&gid=9685&pid=4>.

55. Jauns home page. <https://jauns.lv/foto/zinas/9686-ziemelblazma-livanos#&gid=9686&pid=4>.
56. Jin, Yaqi, Andres Spicher, Chao Xiong, Lasse B. N. Clausen, Guram Kervalishvili, Claudia Stolle, and Wojciech J. Miloch. 2019. "Ionospheric Plasma Irregularities Characterized by the Swarm Satellites: Statistics at High Latitudes." *Journal of Geophysical Research: Space Physics*, 124(2), 1262–1282. <https://doi.org/10.1029/2018JA026063>.
57. Julien, Olivier, Ikhlas Selmi, Pagot Jean-Baptiste, Jaron Samson, and Francisco Amarillo Fernandez. 2017. "Extension of EWF threat model and associated SQM." *Proceedings of the 2017 International Technical Meeting of The Institute of Navigation, ITM 2017*. <https://doi.org/10.33012/2017.14873>.
58. Kaminskis, Janis. 2010. "Latvian geoid model and its development [in Latvian]." Riga: Riga Technical University, Faculty of Civil Engineering Institute of Transport Structures. Doctoral Thesis.
59. Kintner, P. M., B. M. Ledvina, and E. R. de Paula. 2007. "GPS and ionospheric scintillations." *Space Weather*, 5(9). <https://doi.org/10.1029/2006SW000260>.
60. Kotulak, K., A. Krankowski, A. Froń, P. Flisek, N. Wang, Z. Li, and L. Błaszkiwicz. 2021. "Sub-auroral and mid-latitude gnss roti performance during solar cycle 24 geomagnetic disturbed periods: Towards storm's early sensing." *Sensors*, 21(13). <https://doi.org/10.3390/s21134325>.
61. Kuai, J., L. Liu, J. Liu, S. Sripathi, B. Zhao, Y. Chen, H. Le, and L. Hu. 2016. "Effects of disturbed electric fields in the low-latitude and equatorial ionosphere during the 2015 St. Patrick's Day storm." *Journal of Geophysical Research: Space Physics*, 121(9), 9111–9126. <https://doi.org/10.1002/2016JA022832>.
62. Laundal, K. M., and A. D. Richmond. 2017. "Magnetic Coordinate Systems." *Space Science Reviews*, 206(1–4), 27–59. <https://doi.org/10.1007/s11214-016-0275-y>.
63. Lee, Jinsil, and Jiyun Lee. 2019. "Correlation between Ionospheric Spatial Decorrelation and Space Weather Intensity for Safety-Critical Differential GNSS Systems." *Sensors*, 19(9), 2127. <https://doi.org/10.3390/s19092127>.
64. Leick, A., L. Rapoport, and D. Tatarnikov. 2015. *GPS Satellite Surveying: Fourth Edition*. <https://doi.org/10.1002/9781119018612>.
65. Li, G., B. Ning, M. A. Abdu, X. Yue, L. Liu, W. Wan, and L. Hu. 2011. "On the occurrence of postmidnight equatorial F region irregularities during the June solstice." *Journal of Geophysical Research: Space Physics*, 116(4). <https://doi.org/10.1029/2010JA016056>.

66. Liu, Jing, Wenbin Wang, Alan Burns, Xinan Yue, Shunrong Zhang, Yongliang Zhang, and Chaosong Huang. 2016. "Profiles of ionospheric storm-enhanced density during the 17 March 2015 great storm." *Journal of Geophysical Research: Space Physics*, 121(1), 727–744. <https://doi.org/10.1002/2015JA021832>.
67. Liu, J. Y., C. H. Lin, Y. I. Chen, Y. C. Lin, T. W. Fang, C. H. Chen, Y. C. Chen, and J. J. Hwang. 2006. "Solar flare signatures of the ionospheric GPS total electron content." *Journal of Geophysical Research*, 111(A5), A05308. <https://doi.org/10.1029/2005JA011306>.
68. Liu, Xifeng, Yunbin Yuan, Bingfeng Tan, and Min Li. 2016. "Observational Analysis of Variation Characteristics of GPS-Based TEC Fluctuation over China." *ISPRS International Journal of Geo-Information*, 5(12), 237. <https://doi.org/10.3390/ijgi5120237>.
69. Liu, Yang, Lianjie Fu, Jinling Wang, and Chunxi Zhang. 2017. "Study of GNSS Loss of Lock Characteristics under Ionosphere Scintillation with GNSS Data at Weipa (Australia) During Solar Maximum Phase." *Sensors*, 17(10), 2205. <https://doi.org/10.3390/s17102205>.
70. Liu, Y., C. Zhou, T. Xu, Q. Tang, Z. X. Deng, G. Y. Chen, and Z. K. Wang. 2021. "Review of ionospheric irregularities and ionospheric electrodynamic coupling in the middle latitude region." In *Earth and Planetary Physics* (Vol. 5, Issue 5, pp. 462–482). John Wiley and Sons Inc. <https://doi.org/10.26464/epp2021025>.
71. LSM home page. <http://www.lsm.lv/raksts/laika-zinas/laika-zinas/foto-un-video-nakti-daudzviet-latvija-un-citur-pasaule-noverota-spilgta-ziemelblazma.a121924/>.
72. Madsen, F., and B. Madsen. 1993. "A new GPS-network in the Baltic countries." *Symposium of the IAG Subcommission for Europe (EUREF), 17–19 May 1993, Budapest*, 83–91.
73. Mayer, Christoph, Boubeker Belabbas, Norbert Jakowski, Michael Meurer and Winfried Dunkel. 2009. "Ionosphere Threat Space Model Assessment for GBAS." *ION GNSS 2009*, 22-25 Sep. 2009, Savannah, GA, USA.
74. Morozova, A. L., T. V. Barlyaeva, and T. Barata. 2020. "Variations of TEC Over Iberian Peninsula in 2015 Due to Geomagnetic Storms and Solar Flares." *Space Weather*, 18(11). <https://doi.org/10.1029/2020SW002516>.
75. Morozova, Katerīna. 2022. "Parameter estimation on hybrid zenith camera and gravimeter data for integrated gravity field and geoid determination based on spherical-cap-harmonics modelling." Riga. <https://doi.org/10.7250/9789934228162>.
76. NASA home page. <https://wind.nasa.gov/>.

77. NASA home page. <https://www.nasa.gov/goddard>.
78. "National Risk Register of Civil Emergencies 2017 edition." 2017. [www.official-documents.gov.uk](http://www.official-documents.gov.uk).
79. NOAA home page. [https://www.ngdc.noaa.gov/stp/geomag/kp\\_ap.html](https://www.ngdc.noaa.gov/stp/geomag/kp_ap.html).
80. NOAA home page. [https://www.ngdc.noaa.gov/stp/GEOMAG/kp\\_ap.html](https://www.ngdc.noaa.gov/stp/GEOMAG/kp_ap.html).
81. NOAA home page. <https://www.ngdc.noaa.gov/stp/iono/Dynasonde/>.
82. NOAA home page. <https://www.swpc.noaa.gov/impacts/space-weather-and-gps-systems>.
83. NOAA home page. <https://www.swpc.noaa.gov/phenomena>.
84. NOAA home page. <http://www.swpc.noaa.gov/phenomena/ionospheric-scintillation>.
85. NOAA home page, solar-cycle-progression. <https://www.swpc.noaa.gov/products/solar-cycle-progression>.
86. Park, Jaeheung, Hermann Lühr, Guram Kervalishvili, Jan Rauberg, Claudia Stolle, Young-Sil Kwak, and Woo Kyoung Lee. 2017. "Morphology of high-latitude plasma density perturbations as deduced from the total electron content measurements onboard the Swarm constellation." *Journal of Geophysical Research: Space Physics*, 122(1), 1338–1359. <https://doi.org/10.1002/2016JA023086>.
87. Pi, X., A. J. Mannucci, U. J. Lindqwister, and C. M. Ho. 1997. "Monitoring of global ionospheric irregularities using the worldwide GPS network." *Geophysical Research Letters*. <https://doi.org/10.1029/97GL02273>.
88. Salimov B. G., O. I. Berngardt, A. E. Khmel'nov, K. G. Ratovsky, O. A. Kusonsky. 2023. "Application of convolution neural networks for critical frequency foF2 prediction." *Solar-Terrestrial Physics*. 2023. Vol. 9, Iss. 1. P. 56–67. DOI: 10.12737/stp-91202307.
89. Salmins, K., V. Sproģis, I. Biļinskis, and J. del Pino. 2022. "Local Ties at SLR Station Riga." [https://doi.org/10.1007/1345\\_2022\\_157](https://doi.org/10.1007/1345_2022_157).
90. Schaer, S. 1999. "Mapping and predicting the Earth's ionosphere using the Global Positioning System." *Geodätisch-Geophysikalische Arbeiten in Der Schweiz, Schweizerische Geodätische Kommission, Institut Für Geodäsie Und Photogrammetrie, Eidg. Technische Hochschule Zürich, Zürich, Switzerland*, 59.
91. Silabriedis, Gunars. 2012. "EUPOS®-RĪGA ģeodēziskais atbalsta tīkls un tā daudzfunkcionālā lietošana." *Promocijas darba kopsavilkums*.
92. Skone, S. H. 2001. "The impact of magnetic storms on GPS receiver performance".
93. SONEL home page. <https://www.sonel.org/spip.php?page=gps&idStation=829>.
94. SpaceWeatherLive home page. <https://www.spaceweatherlive.com>.
95. SpaceWeatherLive home page. <https://www.spaceweatherlive.com/en/archive/2015/03.html>].

96. SpaceWeatherLive home page. <https://www.spaceweatherlive.com/en/auroral-activity/kp-index.html>.
97. SpaceWeatherLive home page. [https://www.spaceweatherlive.com/en/auroral-activity/magnetometers.html#Stackplot\\_EU](https://www.spaceweatherlive.com/en/auroral-activity/magnetometers.html#Stackplot_EU).
98. SpaceWeatherLive home page. <https://www.spaceweatherlive.com/en/auroral-activity/top-50-geomagnetic-storms>.
99. SpaceWeatherlive home page. <https://www.spaceweatherlive.com/en/help/the-interplanetary-magnetic-field-imf>.
100. SpaceWeatherLive home page. <https://www.spaceweatherlive.com/en/help/what-is-a-coronal-mass-ejection-cme.html>.
101. SpaceWeatherLive home page. <https://www.spaceweatherlive.com/en/solar-activity/solar-cycle.html>.
102. Spogli, L., L. Alfonsi, G. De Franceschi, V. Romano, M. H. O. Aquino, and A. Dodson. 2009. "Climatology of GPS ionospheric scintillations over high and mid-latitude European regions." *Annales Geophysicae*, 27(9), 3429–3437. <https://doi.org/10.5194/angeo-27-3429-2009>.
103. Sreeja, V. 2016. "Impact and mitigation of space weather effects on GNSS receiver performance." In *Geoscience Letters* (Vol. 3, Issue 1). SpringerOpen. <https://doi.org/10.1186/s40562-016-0057-0>.
104. Sripathi, S., S. Bose, A. K. Patra, T. K. Pant, B. Kakad, and A. Bhattacharyya. 2008. "Simultaneous observations of ESF irregularities over Indian region using radar and GPS." *Annales Geophysicae*, 26(11), 3197–3213. <https://doi.org/10.5194/angeo-26-3197-2008>.
105. Stankov, S. M., R. Warnant, and K. Stegen. 2009. "Trans-ionospheric GPS signal delay gradients observed over mid-latitude Europe during the geomagnetic storms of October–November 2003." *Advances in Space Research*, 43(9), 1314–1324. <https://doi.org/10.1016/j.asr.2008.12.012>.
106. Sverige. Myndigheten för samhällsskydd och beredskap. 2012. *Conference proceedings: international round-table on extreme space weather: geomagnetic storms, GNSS disruptions and the impact on vital functions in society: Stockholm, 5-6 september 2012*. Swedish Civil Contingencies Agency (MSB).
107. Verkhoglyadova, O. P., B. T. Tsurutani, A. J. Mannucci, M. G. Mlynczak, L. A. Hunt, L. J. Paxton and A. Komjathy. 2016. "Solar wind driving of ionosphere-thermosphere responses in three storms near St. Patrick's Day in 2012, 2013, and 2015." *Journal of Geophysical Research: Space Physics*, 121(9), 8900–8923. <https://doi.org/10.1002/2016JA022883>.

108. Wautelet, G. 2012. "Characterization of ionospheric irregularities and their influence on high-accuracy positioning with GPS over mid-latitudes."
109. Space Weather Operations, and Mitigation Working Group. 2019. "National Space Weather Strategy and Action Plan." <http://www.whitehouse.gov/ostp>.
110. Space Weather Operations, Research, and Mitigation Subcommittee, Committee on Homeland and National Security of the National Science and Technology Council. 2018. "*Space weather phase 1 benchmarks*." <http://www.whitehouse.gov/ostp>.
111. Yang, Zhe, Y. T. Jade Morton, Irina Zakharenkova, Iurii Cherniak, Shuli Song, and Wei Li. 2020. "Global View of Ionospheric Disturbance Impacts on Kinematic GPS Positioning Solutions During the 2015 St. Patrick's Day Storm." *Journal of Geophysical Research: Space Physics*, 125(7). <https://doi.org/10.1029/2019JA027681>.
112. Zakharenkova, I., E. Astafyeva, and I. Cherniak. 2016. "GPS and GLONASS observations of large-scale traveling ionospheric disturbances during the 2015 St. Patrick's Day storm." *Journal of Geophysical Research: Space Physics*, 121(12), 12,138-12,156. <https://doi.org/10.1002/2016JA023332>.
113. Zvirgzds, Janis. 2007. "Geodetic measurements using GPS base station system LatPos." *Geomatics*, 11(RTU), 81–89.
114. Zvirgzds, Janis. 2012. "Rational system LatPos [in Latvian]." Riga: Riga Technical University, Department of Geomatics. Doctoral Thesis.



**Madara Normand** (nee Caunite) was born in 1979 in Riga. In 1999, she received a Bachelor's degree in Civil Engineering and an engineer's qualification in Geodesy and Cartography in 2001. In 2005, she received a degree of Master of Engineering in Civil Engineering from Riga Technical University. In 2009, she obtained a Master's degree in Geomatics from École Nationale des Sciences Géographiques (France). From 1999 to 2005, she was an engineer-programmer at the Institute of Geodesy and Geoinformatics of the University of Latvia (LU GGI). From February to June 2000, she studied at the Technical University of Denmark within the Socrates/Erasmus programme. From February to June 2002, she was an assistant at Riga Technical University. From April 2003 to September 2005, she was the managing director at "Mūsu mērnies" Ltd. From June to January 2003, she worked at Riga Technical University on project COSTG9. From June to September 2004, she was a professional educational consultant/salesperson at The Southwestern Company, Nashville, TN, USA. From May to December 2006, she had an internship at the société EXAGONE (France) within the frame of the master's study programme. Since 2007, she has been a researcher at the LU GGI.